# *Evaluation of Engineered Barrier Systems FY19 Report*

## Spent Fuel and Waste Disposition

*Prepared for US Department of Energy*
*Spent Fuel and Waste Science and Technology*

*E.N. Matteo and T. Hadgu, Sandia National Laboratories*

*L. Zheng, H. Xu, H. Wainwright, N. Subramanian,*
*M. Voltolini, L. Lammers, B. Gilbert, A. MacDowell,*
*J. Nichol, H. Lisabeth, Lawrence Berkeley National*
*Laboratory*

*N. van Hartesveldt, A. Migdissov, A.C. Strzelecki,*
*H. Xu, F. Caporuscio, R. Roback, J. White*
*Los Alamos National Laboratory*

*E.C. Buck, X-Y Yu, J. Yao, D.D. Reilly, J. Son,*
*S.D. Chatterjee, B.K. McNamara, E.S. Ilton,*
*Pacific Northwest National Laboratory*

*F. Claret, S. Gaboreau, The Bureau de Recherches*
*Géologiques et Minières (BRGM), France*

*D. Ermakova, University of California, Berkeley*

*R. Gabitov, Mississippi State University*

This is a technical paper that does not take into account the contractual limitations under the Standard Contract for Disposal of Spent Nuclear Fuel and/or High-Level Radioactive Waste (Standard Contract) (10 CFR Part 961). For example, under the provisions of the Standard Contract, DOE does not consider spent nuclear fuel in multi-assembly canisters to be an acceptable waste form, absent a mutually agreed to contract amendment. To the extent discussions or recommendations in this pape conflict with the provisions of the Standard Contract, the Standard Contract governs the obligations of the parties, and this paper in no manner supersedes, overrides, or amends the Standard Contract. This paper reflects technical work which could support future decision making by DOE. No inferences should be drawn from this paper regarding future actions by DOE, which are limited both by the terms of the Standard Contract and a lack of Congressional appropriations for the Department to fulfill its obligations under the Nuclear Waste Policy Act including licensing and construction of a spent nuclear fuel repository.

Revision 5
01/15/2018

## APPENDIX E
## NTRD DOCUMENT COVER SHEET[1]

Name/Title of
Deliverable/Milestone/Revision No.    Evaluation of Engineered Barrier Systems FY19 Report

Work Package Title and Number    Engineered Barrier Systems R&D – SNL, SF-20SN01030804

Work Package WBS Number    1.08.01.03.08

Responsible Work Package Manager    Edward N. Matteo /
(Name/Signature)

Date Submitted

| Quality Rigor Level for Deliverable/Milestone[2] | ☐ QRL-1 ☐ Nuclear Data | ☐ QRL-2 | ☒ QRL-3 | ☐ QRL-4 Lab QA Program[3] |
|---|---|---|---|---|

This deliverable was prepared in accordance with    Sandia National Laboratories
(Participant/National Laboratory Name)

QA program which meets the requirements of

☒ DOE Order 414.1    ☐ NQA-1    ☐ Other
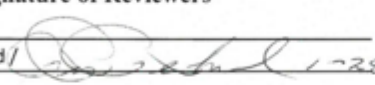
**This Deliverable was subjected to:**

☒ Technical Review                      ☐ Peer Review

**Technical Review (TR)**                **Peer Review (PR)**

**Review Documentation Provided**        **Review Documentation Provided**

☐ Signed TR Report or,                  ☐ Signed PR Report or,

☐ Signed TR Concurrence Sheet or,        ☐ Signed PR Concurrence Sheet or,

☒ Signature of TR Reviewer(s) below      ☐ Signature of PR Reviewer(s) below

**Name and Signature of Reviewers**

Robert P. Rechard /                     1-28-2020

NOTE 1:  *Appendix E should be filled out and submitted with the deliverable. Or, if the PICS:NE system permits, completely enter all applicable information in the PICS:NE Deliverable Form. The requirement is to ensure that all applicable information is entered either in the PICS:NE system or by using the NTRD Document Cover Sheet.*

   • *In some cases there may be a milestone where an item is being fabricated, maintenance is being performed on a facility, or a document is being issued through a formal document control process where it specifically calls out a formal review of the document. In these cases, documentation (e.g., inspection report, maintenance request, work planning package documentation or the documented review of the issued document through the document control process) of the completion of the activity, along with the Document Cover Sheet, is sufficient to demonstrate achieving the milestone.*

NOTE 2:  *If QRL 1, 2, or 3 is not assigned, then the QRL 4 box must be checked, and the work is understood to be performed using laboratory QA requirements. This includes any deliverable developed in conformance with the respective National Laboratory / Participant, DOE or NNSA-approved QA Program.*

NOTE 3: *If the lab has an NQA-1 program and the work to be conducted requires an NQA-1 program, then the QRL-1 box must be checked in the work Package and on the Appendix E cover sheet and the work must be performed in accordance with the Lab's NQA-1 program. The QRL-4 box should not be checked.*

This page is intentionally left blank.

# SUMMARY

This report describes research and development (R&D) activities conducted during fiscal year 2019 (FY19) specifically related to the Engineered Barrier System (EBS) R&D Work Package in the Spent Fuel and Waste Science and Technology (SFWST) Campaign supported by the United States (U.S.) Department of Eneregy (DOE). The R&D activities focus on understanding EBS component evolution and interactions within the EBS, as well as interactions between the host media and the EBS. A primary goal is to advance the development of process models that can be implemented directly within the Genreric Disposal System Analysis (GDSA) platform or that can contribute to the safety case in some manner such as building confidence, providing further insight into the processes being modeled, establishing better constraints on barrier performance, etc.The FY19 EBS activities involved not only modeling and analysis work, but experimental work as well.

The report documents the FY19 progress made in seven different research areas as follows: (1) thermal analysis for the disposal of dual purpose canisters (DPCs) in sedimentary host rock using the semi-analytical method, (2) tetravalent uranium solubility and speciation, (3) modeling of high temperature, thermal-hydrologic-mechanical-chemical (THMC) coupled processes, (4) integration of coupled thermal-hydrologic-chemical (THC) model with GDSA using a Reduced-Order Model, (5) studying chemical controls on montmorillonite structure and swelling pressure, (6) transmission x-ray microscope for in-situ nanotomography of bentonite and shale, and (7) in-situ electrochemical testing of uranium dioxide under anoxic conditions.

The R&D team consisted of subject matter experts from Sandia National Laboratories, Lawrence Berkeley National Laboratory (LBNL), Los Alamos National Laboratory (LANL), Pacific Northwest National Laboratory (PNNL), the Bureau de Recherches Géologiques et Minières (BRGM), the University of California Berkeley, and Mississippi State University. In addition, the EBS R&D work leverages international collaborations to ensure that the DOE program is active and abreast of the latest advances in nuclear waste disposal. For example, the FY19 work on modeling coupled THMC processes at high temperatures relied on the bentonite properties from the Full-scale Engineered Barrier EXperiment (FEBEX) Field Test conducted at the Grimsel Test Site in Switzerland.

Overall, significant progress has been made in FY19 towards developing the modeling tools and experimental capabilities needed to investigate the performance of EBS materials and the associated interactions in the drift and the surrounding near-field environment under a variety of conditions including high temperature regimes.

# ACKNOWLEDGEMENTS

# CONTENTS

# LIST OF FIGURES

# LIST OF TABLES

# ACRONYMS

| | |
|---|---|
| µXCT | microscale x-ray computed tomography |
| 2D | two dimensional |
| 3D | three dimensional |
| ALS | Advanced Light Source |
| APS | Advanced Photon Source |
| BBM | Barcelona Basic Model |
| BExM | Barcelona Expansive Model |
| BRGM | The Bureau de Recherches Géologiques et Minières, France |
| CCD | charge coupled device |
| CE | counter electrode |
| CPU | central processing unit |
| DLVO | Derjaguin-Landau-Verwey-Overbeek |
| DOE | Department of Energy |
| DOE NE | DOE Nuclear Energy |
| DPC | dual purpose canister |
| DRIE | deep reactive ion etching |
| DS | drift spacing |
| DW | drift wall |
| EBS | engineering barrier system |
| EDS | x-ray energy dispersive spectroscopy |
| EELS | electron energy-loss spectroscopy |
| ELSM | Extended Linear Swelling Model |
| FEBEX | Full-scale Engineered Barrier EXperiment |
| FEG | field emission gun |
| FIB | focused ion beam |
| FIB-SEM | focused (gallium) ion beam-scanning electron microscope |
| FMDM | Fuel Matrix Dissolution Model |
| FY | fiscal year |
| GCMC | Grand Canonical Monte Carlo |
| GDSA | Generic Disposal System Analyses |
| GSA | global sensitivity analysis |
| GWd/MT | gigawatt (thermal) - days per metric ton |

| HAADF | high angle annular dark field |
| HPLC | high performance liquid chromatography |
| ICP-MS | inductively coupled plasma–mass spectrometry |
| KPA | kinetic phosphorimetry |
| LANL | Los Alamos National Laboratory |
| LBNL | Lawrence Berkeley National Laboratory |
| MC | mechanical-chemical |
| MD | molecular dynamics |
| MGC | Modified Gouy-Chapman |
| MMT | montmorillonite |
| MPM | Mixed Potential Model |
| MRB | Ryzhenko–Bryzgalin |
| OAT | one-at-a-time |
| OoR | out-of-reactor |
| PA | performance assessment |
| PCE | polynomial chaos expansion |
| PDMS | polydimethylsiloxane |
| PI | Physique Instrument |
| PNNL | Pacific Northwest National Laboratory |
| ppb | parts per billion |
| ppm | parts per million |
| PWR | pressurized water reactor |
| R&D | research and development |
| RE | reference electrode |
| RM | Radiolysis Model |
| ROM | Reduced Order Model |
| RPL | Radiochemical Processing Laboratory |
| SALVI | System for Analysis at the Liquid Vacuum Interface |
| SAXS | small-angle x-ray scattering |
| SEM | scanning electron microscopy/microscope |
| SEM-EDS | scanning electron microscopy/microscope–x-ray energy dispersive spectroscopy |
| SFWST | Spent Fuel and Waste Science and Technology |
| SIMS | secondary ion mass spectrometry |
| SNF | spent nuclear fuel |

| | |
|---|---|
| SPC/E | extended simple point charge |
| STEM | scanning transmission electron microscopy |
| STEM-EDS | scanning transmission electron microscopy–x-ray energy dispersive spectroscopy |
| swp | saturated water vapor pressure |
| TEM | transmission electron microscopy |
| TEM-EELS | transmission electron microscopy-electron energy-loss spectroscopy |
| THC | thermal-hydrologic-chemical |
| THM | thermal-hydrologic-mechanical |
| THMC | thermal-hydrologic-mechanical-chemical |
| THMCB | thermal-hydrologic-mechanical-chemical-biogeo |
| TM | thermal-mechanical |
| ToF-SIMS | time-of-flight secondary ion mass spectrometry |
| TSR | thermochemical sulfate reduction |
| TXM | transmission x-ray microscopy/microscope |
| U.S. | United States |
| WE | working electrode |
| WP | waste package |
| Wy-MMT | Wyoming montmorillonite |
| XCT | x-ray computed tomography |
| XPS | x-ray photoelectron spectroscopy |
| XRD | x-ray diffraction |
| ZP | zone plate |

# SPENT FUEL AND WASTE SCIENCE AND TECHNOLOGY/ENGINEERED BARRIER SYSTEM R&D

## 1.   INTRODUCTION

This report describes research and development (R&D) activities conducted during fiscal year 2019 (FY19) specifically related to the Engineered Barrier System (EBS) R&D Work Package in the Spent Fuel and Waste Science and Technology (SFWST) Campaign supported by the United States (U.S.) Department of Energy (DOE). The R&D team consists of individuals from Sandia National Laboratories, Lawrence Berkeley National Laboratory (LBNL), Los Alamos National Laboratory (LANL), Pacific Northwest National Laboratory (PNNL), the Bureau de Recherches Géologiques et Minières (BRGM), the University of California Berkeley, and Mississippi State University.

The R&D activities described in this report focus on understanding EBS component evolution and interactions within the EBS, as well as interactions between the host media and the EBS. A primary goal is to advance the development of process models that can be implemented directly within the Generic Disposal System Analysis (GDSA) platform or that can contribute to the safety case in some manner such as building confidence, providing further insight into the processes being modeled, establishing better contraints on barrier performance, etc.

The FY19 EBS activities involved not only modeling and analysis work, but experimental work as well. The report documents the FY19 progress made in seven different research areas as follows:

- **Thermal Analysis for the Disposal of Dual Purpose Canisters in Sedimentary Host Rock using the Semi-analytical Method (Section 2)**

  This section presents the results of a thermal, semi-analytical analysis for the disposal of dual purpose canisters (DPCs) for the sedimentary closed repository concept. The simulations were conducted in support of the GDSA. The simulations provide estimates of temperature at the surface of the waste package and the drift wall to help decide repository layout for performance assessment (PA) analysis. The semi-analytical method is based on the approach developed for enclosed emplacement modes (no ventilation) by Hardin et al. (2011; 2012). Thermal responses for pressurized water reactor (PWR) waste forms were investigated for a disposal concept in generic sedimentary host rock. These simulations are a continuation of previous work with increased focus on disposal of 37-PWR DPCs in closed-mode, sedimentary repository setting. The thermal calculations were based on a set of selected properties and parameters. A parametric study was also conducted for different repository configurations and disposal scenarios. The analysis examined the effects of drift spacing, waste package spacing, backfill thermal conductivity, number of PWR assemblies per waste package, and surface storage period.

- **Tetravalent Uranium Solubility and Speciation (Section 3)**

  This section presents the results of experiments on the solubility of $UO_2$ and speciation of U in $SO_4$-bearing, 1 m NaCl solutions at 250°C, 300°C, and 350°C and saturated water vapor pressure. The data obtained suggest unexpectedly high stability of U(IV)-sulfate aqueous complexes. The predominant sulfate complex of U(IV) was identified as the neutral aqueous species, $U(OH)_2SO_4^o$. In the sulfate-bearing solutions ranging from 0.01 to 0.35 mol/kg of total dissolved sulfate, $U(OH)_2SO_4^o$ controls the solubility of uranium at reducing conditions. However, even within more modest sulfate concentration ranges, uranium concentrations can range from hundreds of parts per billion (ppb) to tens of parts per million (ppm) when in

equilibrium with uraninite. Logarithms of the formation constant ($U_4^+ + SO_4^{2-} + 2OH^- = U(OH)_2SO_4$) for this species are 30.18, 32.16, and 36.31, respectively, at 250°C, 300°C, and 350°C.

- **Modeling of High Temperature THMC Processes (Section 4)**

  This section presents the results of the application of thermal-hydrological-mechanical-chemical (THMC) modeling to evaluate the EBS bentonite characteristics in the argillite repository under different temperatures of 100°C and 200°C. The Barcelona Expansive Model (BExM) was integrated into the simulator TOUGHREACT-FLAC and its application was verified against laboratory tests. Coupled THMC models were used for simulations of the generic cases of heating for both 100°C and 200°C scenarios. While Zheng et al. (2019) reported the results of simulations of temperature, water saturation, stress and chemical changes, in this report, the focus is on simulations of the stress paths. Because modeling of THMC processes for the PA would likely require a large number of THMC simulations, we have begun transitioning simulations from TOUGHREACT-FLAC to a newly developed numerical simulator TReactMech, which is better suited for simulations of large computational problems and runs on the Linux platform.

- **Integration of Coupled THC Model with GDSA using Reduced-Order Model (Section 5)**

  This section presents an endeavor of integrating coupled thermal-hydrologic-chemical (THC) models into the GDSA using a Reduced Order Model (ROM). The ultimate goal is to develop a ROM-based methodology and toolsets for integrating complex, coupled models (such as THMC or THC) into the overall PA model. The particular focus in this section is to compute the spatial/process-integrated $K_d$ values to be used in the PA models. Up to now, the spatial temporal evolutions of $K_d$ in EBS for a generic bentonite-argillite system were evaluated and a global sensitivity analysis (GSA) was conducted to evaluate the impact of each parameter on the performance measure ($K_d$ in this case) over the full range of multidimensional parameters.

- **Studying Chemical Controls on Montmorillonite Structure and Swelling Pressure (Section 6)**

  This section presents the progress on computational and thermodynamic modeling of clay swelling and an experimental study of chemical controls on montmorillonite swelling pressure and structure. Molecular mechanics simulations were combined with thermodynamic modeling to predict the coexistence of multiple swelling states for montmorillonite clay. In addition, a miniaturized oedometer cell for synchrotron x-ray studies of dynamic changes in compacted swelling clay structure were developed.

- **Transmission X-ray Microscope for In-situ Nanotomography of Bentonite and Shale (Section 7)**

  This section presents the results of another experimental research activity aimed at the design and commission of a new transmission x-ray microscope (TXM) at beamline 11.3.1, and provides proof-of-principle data on (1) the structural evolution of hydrated compacted bentonite under changing chemical conditions, and (2) the deformation and fracture sealing of candidate repository rocks, such as shale or halite, under stress over multiple time scales, which will improve the fundamental understanding of interaction of chemical and mechanical processes taking place in bentonite. A novel uniaxial stress-strain cell has been designed and all components purchase or fabricated.

- **In-situ Electrochemical Testing of Uranium Dioxide under Anoxic Conditions (Section 8)**

  This section presents the work done to build the capabilities needed to perform in-situ electrochemical corrosion testing of uranium dioxide ($UO_2$) in the electron microscopy as well as

the experimental work completed thus far. A vacuum-compatible, microfluidic interface System for Analysis at the Liquid Vacuum Interface (SALVI) has been developed to enable surface analysis of liquids and liquid-solid interactions using scanning electron microscopy (SEM) and time-of-flight secondary ion mass spectrometry (ToF-SIMS). This section describes the initial results from the analysis of liquid samples of importance in the geologic disposal of $UO_2$ spent nuclear fuel (SNF) in a repository environment using in-situ liquid SEM and SIMS. The results demonstrate that multimodal analysis of $UO_2$ materials is possible using SALVI and in-situ chemical imaging. Both in-situ liquid SEM and SIMS can be used as new approaches to analyze radioactive materials in liquid and slurry forms of high-level nuclear wastes. In addition, stainless steel materials, like those that would be used in the repository setting, were analyzed using multiple surface tools including SEM, transmission electron microscopy (TEM), x-ray photoelectron spectroscopy (XPS), and ToF-SIMS. The results show that material interfaces change as a result of redox chemistry like those expected in the repository environment.

This report fulfills the SFWST Campaign deliverable M2SF-20SN010308043.

## 2. THERMAL ANALYSIS FOR THE DISPOSAL OF DUAL PURPOSE CANISTERS IN SEDIMENTARY HOST ROCK USING THE SEMI-ANALYTICAL METHOD

A thermal, semi-analytical analysis was conducted for the disposal of DPCs for the closed-mode, sedimentary repository concept. The simulations were conducted in support of the GDSA. The simulations provide estimates of temperature at the surface of the waste package and the drift wall to help decide repository layout for PA analysis. The semi-analytical approach for enclosed emplacement modes (no ventilation) was developed by Hardin et al. (2011, 2012). Thermal responses for PWR waste forms were investigated for a disposal concept in generic sedimentary host rock. Thermal analysis for the disposal of DPCs in several host rocks have been studied for various disposal options. Hardin and Voegele (2013) and Hardin et al. (2013) conducted preliminary analyses for the disposal of 32-PWR DPCs. These simulations included variations of buffer thermal conductivity. Hadgu et al. (2015) and Hardin et al. (2015) expanded the thermal calculations to 37-PWR DPCs and various disposal options. These calculations also included parametric studies. The current simulations are a continuation of previous work with increased focus on disposal of 37-PWR DPCs in closed-mode, sedimentary repository setting. The thermal calculations were based on a set of selected properties and parameters. A parametric study was also conducted for different repository configurations and disposal scenarios. The analysis looked at effect of drift spacing, waste package spacing, backfill thermal conductivity, number of PWR assemblies per container, and surface storage period.

## 2.1 Simulation Input Data

The repository was assumed to be at 500-m depth. Ambient average ground surface temperature of 15°C, and a natural geothermal gradient of 25°C/km were used. The disposal concept is based on DPCs placed in overpacks (Figure 2-1) emplaced individually horizontally. The selected geometry for the analysis includes a drift diameter of 4.5 m and a waste package diameter of 2.0 m with 5.6-m length. Thermal conductivity of the sedimentary host rock was assumed to be 1.2 W/(m·K) (Hardin et al. 2012). For the base case the buffer material is assumed to be engineered to provide higher thermal conductivity than bentonite or crushed alluvium backfill. A summary of the base case input data is given below.

Parameters selected for the base case include

- Waste package includes 37-PWR assemblies at 60 GWd/MT burnup

- Surface storage of 150 years out of reactor

- Sedimentary closed repository concept (no ventilation) with host rock thermal conductivity of 1.2 W/(m·K) and thermal diffusivity of $8.22 \times 10^{-7}$ m$^2$/s (i.e. volumetric heat capacity of $1.46 \times 10^{6}$ J/(m$^3$·K))

- Buffer thermal conductivity of 1.0 W/(m·K)

- Drift diameter of 4.5 m

- DPC dimensions: waste package diameter of 2 m and length of 5.6 m

- Drift spacing of 60 m

- Waste package spacing of 20 m (center-to-center)

For parametric study, the following variations were made:

- Waste package with 4-PWR and 12-PWR assemblies at 60 GWd/MT burnup. Decay heat for different assemblies is given in Figure 2-2.

- Sedimentary closed repository concept with host rock thermal conductivity of 1.2 W/(m·K) and thermal diffusivity of $4.8 \times 10^{-7}$ m$^2$/s (i.e. volumetric heat capacity of $2.5 \times 10^6$ J/(m$^3$·K))

- Buffer thermal conductivity values of 0.6 (dry bentonite), 1.5, and 2.0 W/(m·K)

- Drift spacing of 30, 40, 50, 70, 75, 80 m

- Waste package spacing of 30 m



**Dual Purpose Storage Cask***

Cask Lid

Diameter: 98 ir

Steel Canister (0.5 in)

Bundles of used fuel assemblies

Concrete Wall (26.75 in.)

(Holtec International HI-STORM 100)

Overall Length:  197 to 225 in.
Loaded Weight:  360,000 lbs.
Typical Payload:  24 PWR Bundles

*Storage and Transportation*
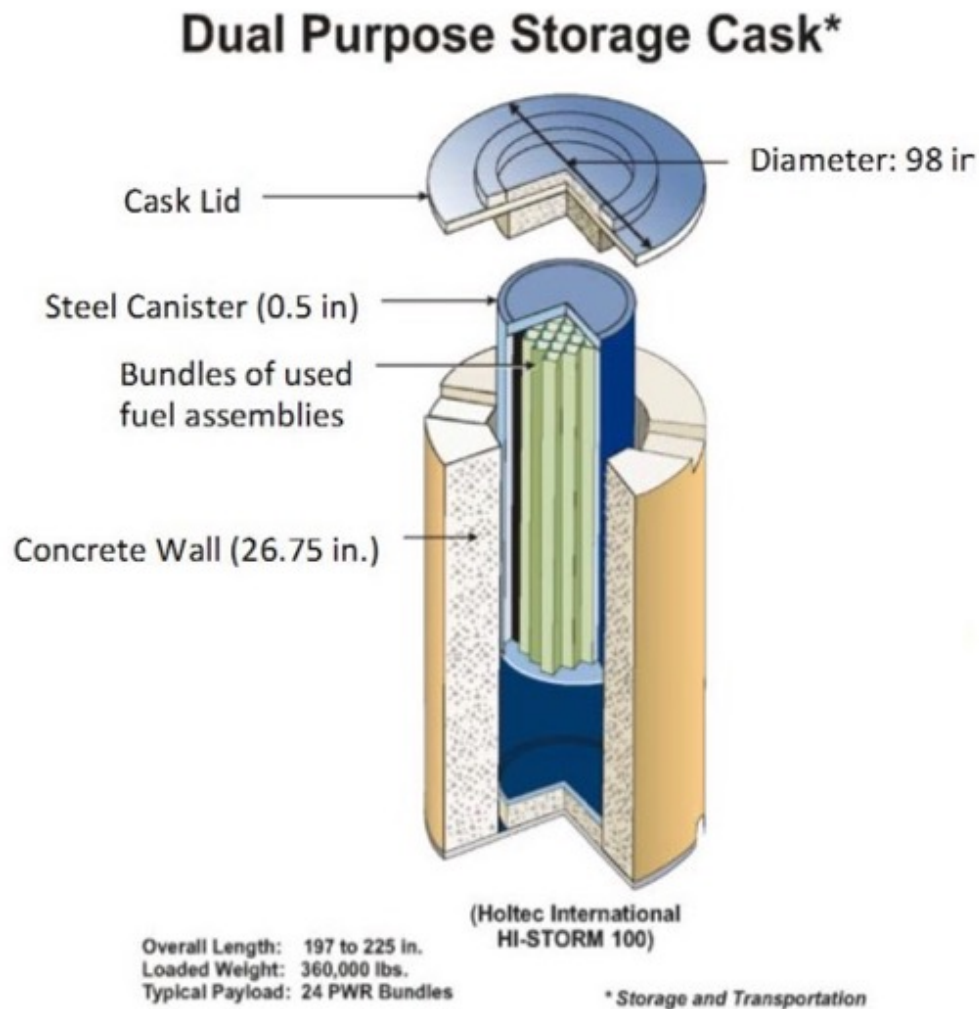
Source: Hardin et al. 2015, modified from Easton 2011.

**Figure 2-1.  Example of a DPC inside a storage overpack (cask)**
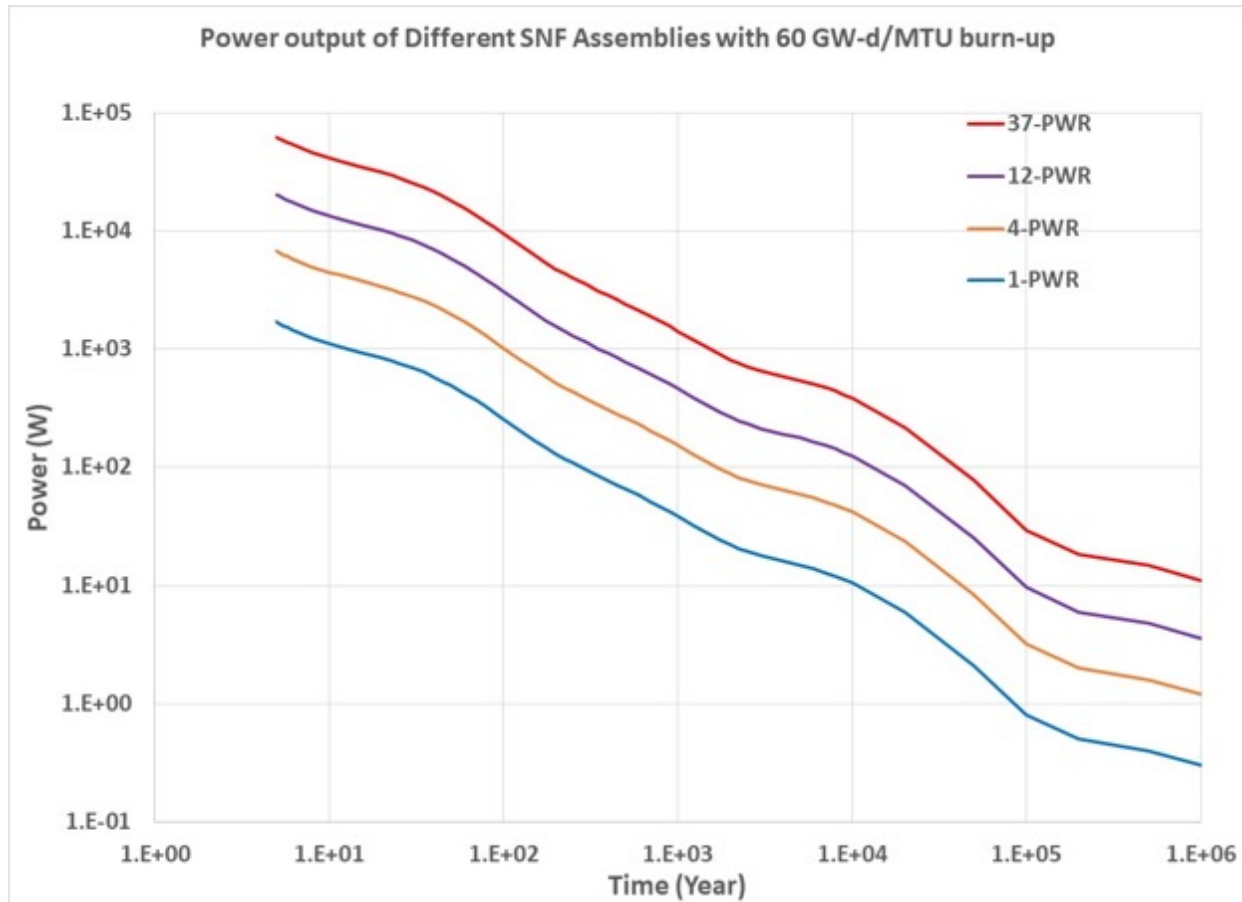
NOTE:    Time given by the *x*-axis refers to time out of the reactor.

**Figure 2-2.  Waste package decay heat power after discharge from PWR reactor
for various numbers of SNF assemblies at 60-GWd/MT burnup**

## 2.2    Results of Semi-analytical, Thermal Analysis

Semi-analytical Mathcad runs were conducted using the host rock and repository layout data, for the base case and variations listed above. Results of the simulations are given below. Maximum waste package and drift wall temperature predictions are given in Table 2-1, Table 2-2, Table 2-3, and Table 2-4. Temperature history plots for the waste package surface and the drift wall for the various combinations of input are given in Figure 2-3 to Figure 2-10.

Figure 2-2 shows a log-log power output plot for different assemblies, for 60 GWd/MT burnup. For 37-PWR DPC waste packages the thermal output is considerably higher than 4-PWR and 12-PWR waste packages. For the base case storage time of 150 years the thermal outputs of 37-PWR, 12-PWR and 4-PWR are 6.29 kW, 2.04 kW and 0.68 kW, respectively. Figure 2-3 shows predicted temperatures as a function of time for the base case. The plots show temperatures at the waste package surface and the drift wall. Note that drift wall temperature predictions are conservative.

The peak waste package surface and drift wall temperatures are 315°C and 194°C, respectively. The peak waste package surface temperature is within the 350°C temperature limit for cladding (DOE 2008 and Hardin et al. 2015) and corresponds to the base case data of 150 years surface storage, drift spacing of 60 m, waste package spacing of 20 m and buffer thermal conductivity of 1 W/(m·K). This would represent a relatively large repository foot print and a long surface storage time.
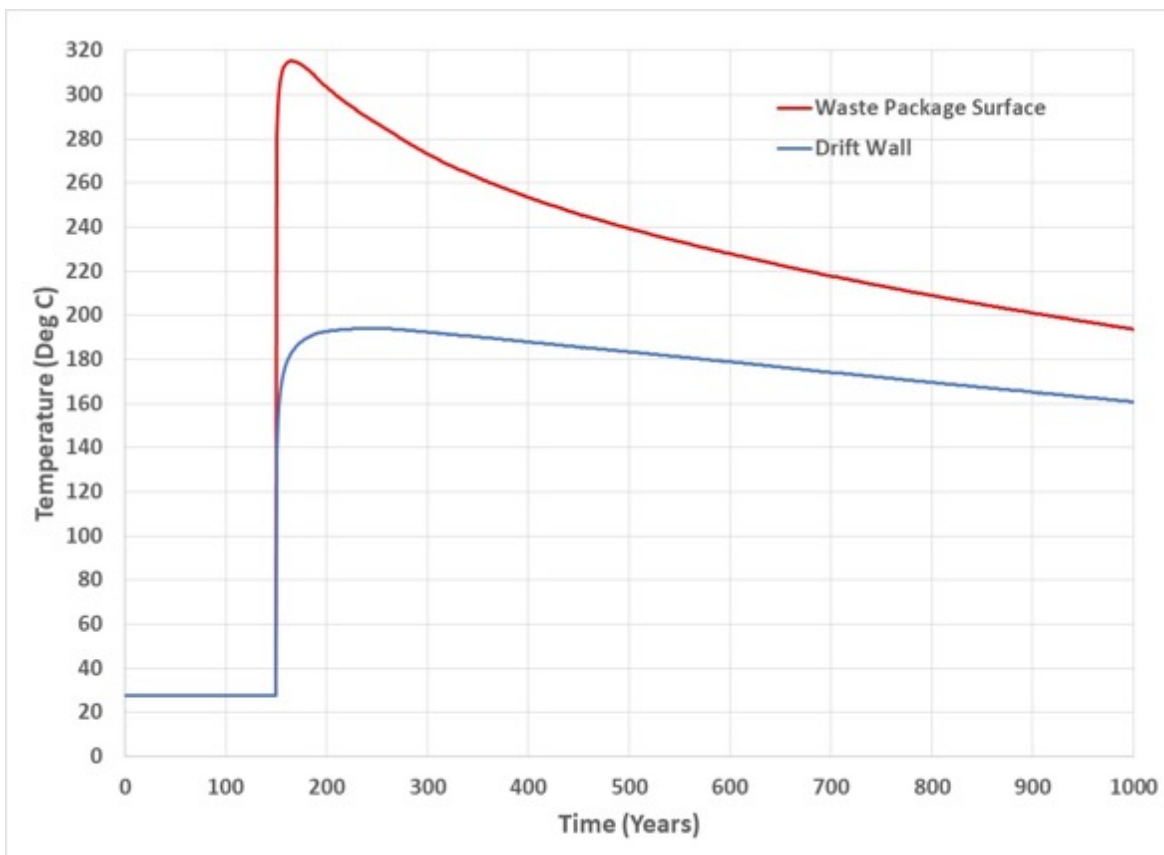
NOTE:    Time given by the *x*-axis refers to time out of the reactor.

**Figure 2-3.  Waste package surface and drift wall temperature prediction
for the base case with emplacement after 150 years of storage**

**Table 2-1.  Predicted maximum temperature at waste package surface and drift wall for
37 PWR (60-Wd/MT burnup) and backfill thermal conductivity of 1.0 W/(m·K)**

| WP Spacing (m) | Drift Spacing (m) | 150-year Storage | |
|---|---|---|---|
| | | Twp max (°C) | Tdw max (°C) |
| 20 | 30 | 358.2 | 272.6 |
| 20 | 40 | 328.3 | 233.3 |
| 20 | 50 | 318.3 | 208.4 |
| 20 | 60 | 315.3 | 194.1 |
| 20 | 70 | 314.6 | 187.3 |
| 20 | 80 | 314.3 | 184.8 |
| 30 | 75 | 302.4 | 168.0 |

NOTE:    WP = waste package.
          Tdw = drift wall temperature.
          Twp = waste package temperature.

**Table 2-2.  Predicted maximum temperature at waste package surface and drift wall for 37 PWR (60-GWd/MT burnup) and backfill thermal conductivity of 0.6 W/(m·K)**

| WP Spacing (m) | Drift Spacing (m) | 150-year Storage | |
|---|---|---|---|
| | | Twp max (°C) | Tdw max (°C) |
| 20 | 30 | 430.1 | 272.6 |
| 20 | 40 | 411.3 | 233.3 |
| 20 | 50 | 406.1 | 208.4 |
| 20 | 60 | 405.0 | 194.1 |
| 20 | 70 | 404.8 | 187.3 |

NOTE:   WP = waste package.
        Tdw = drift wall temperature.
        Twp = waste package temperature.

**Table 2-3.  Predicted maximum temperature at waste package surface and drift wall for 37 PWR (60-GWd/MT burnup) and backfill thermal conductivity of 1.5 W/(m·K)**

| WP Spacing (m) | Drift Spacing (m) | 150-year Storage | |
|---|---|---|---|
| | | Twp max (°C) | Tdw max (°C) |
| 20 | 30 | 327.4 | 272.6 |
| 20 | 40 | 291.2 | 233.3 |
| 20 | 50 | 276.9 | 208.4 |
| 20 | 60 | 271.9 | 194.1 |
| 20 | 70 | 270.3 | 187.3 |

NOTE:   WP = waste package.
        Tdw = drift wall temperature.
        Twp = waste package temperature.

**Table 2-4.  Predicted maximum temperature at waste package surface and drift wall for 37 PWR (60-GWd/MT burnup) and backfill thermal conductivity of 2.0 W/(m·K)**

| WP Spacing (m) | Drift Spacing (m) | 150-year Storage | |
|---|---|---|---|
| | | Twp max (°C) | Tdw max (°C) |
| 20 | 30 | 312.8 | 272.6 |
| 20 | 40 | 275.3 | 233.3 |
| 20 | 50 | 257.3 | 208.4 |
| 20 | 60 | 251.0 | 194.1 |
| 20 | 70 | 248.7 | 187.3 |

NOTE:   WP = waste package.
        Tdw = drift wall temperature.
        Twp = waste package temperature.

A parametric study was conducted to study thermal performance by varying various parameters, with the rest of the parameters kept at the base case values. Figure 2-4 shows waste package surface and drift wall temperature plots for different drift spacing and waste package spacing values. Table 2-1 shows the corresponding peak waste package surface and drift wall temperatures. Temperatures are highest for drift spacing value of 30 m (waste package surface temperature of 358.2°C and drift wall temperature of 272.6°C). For this case temperatures remain high for a long period of time. Peak temperatures can be lowered using larger drift spacing values which would reduce the contributions of waste packages in adjacent drifts. The peak temperature is sensitive to drift spacing values 50 m and lower. Reducing waste package spacing would also reduce the contributions of neighboring waste packages.
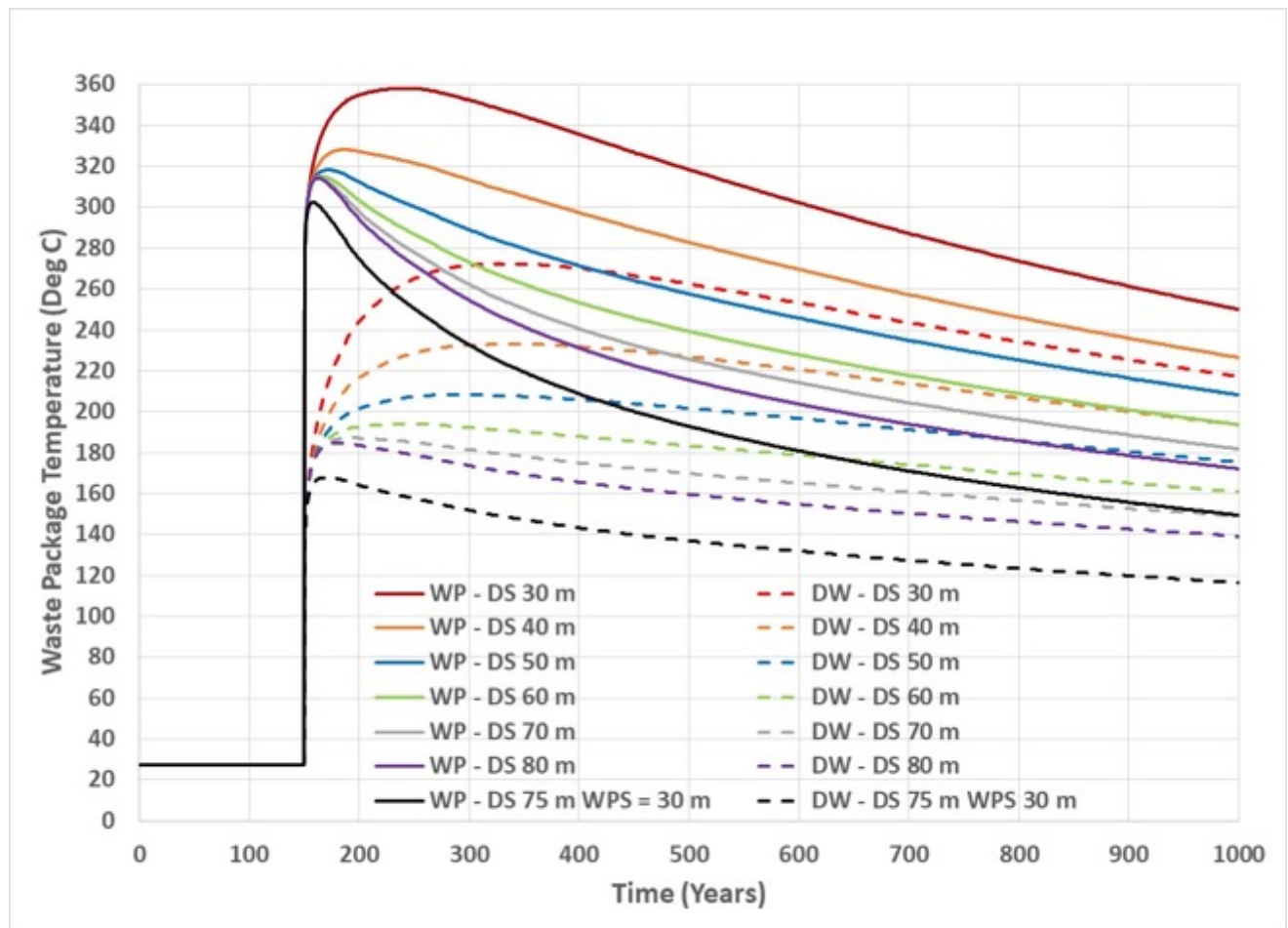


NOTE:    Time given by the *x*-axis refers to time out of the reactor.

WP = waste package surface
DW = drift wall
DS = drift spacing
WPS = waste package spacing

**Figure 2-4.  Waste package surface and drift wall temperature prediction for different drift spacing**
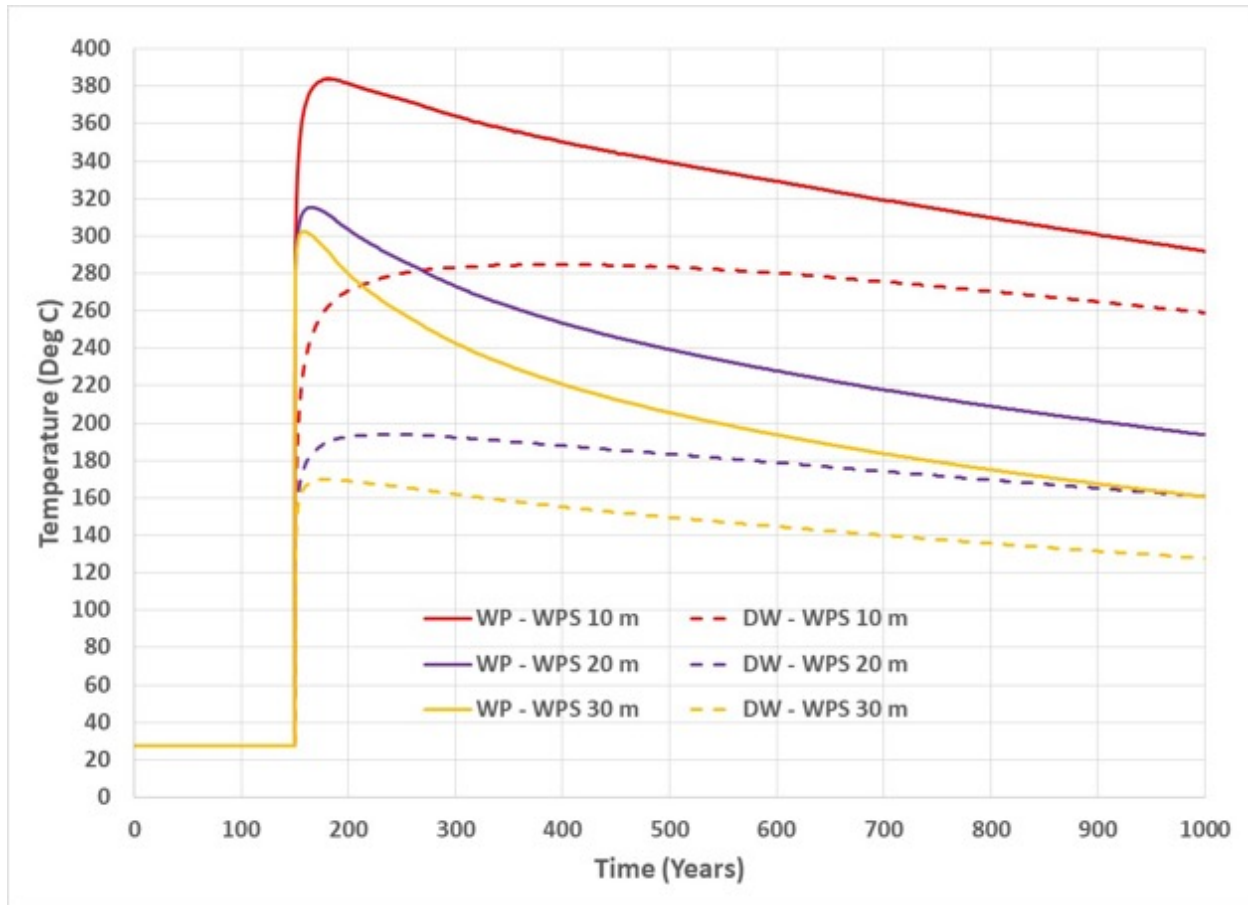
NOTE:   Time given by the *x*-axis refers to time out of the reactor.
WP = waste package surface
DW = drift wall
DS = drift spacing
WPS = waste package spacing

**Figure 2-5.  Waste package surface and drift wall temperature prediction for different waste package spacing (center-to-center), all at 60-m drift spacing**

Sensitivity of waste package surface and drift-wall temperature to waste package spacing is shown in Figure 2-5. Peak temperatures are highest for waste package spacing of 10 m (384.0°C for waste package surface and 284.9°C for drift wall). Use of 30 m waste package spacing significantly reduces the peak temperatures (302.5°C for waste package surface and 170.1°C for drift wall).
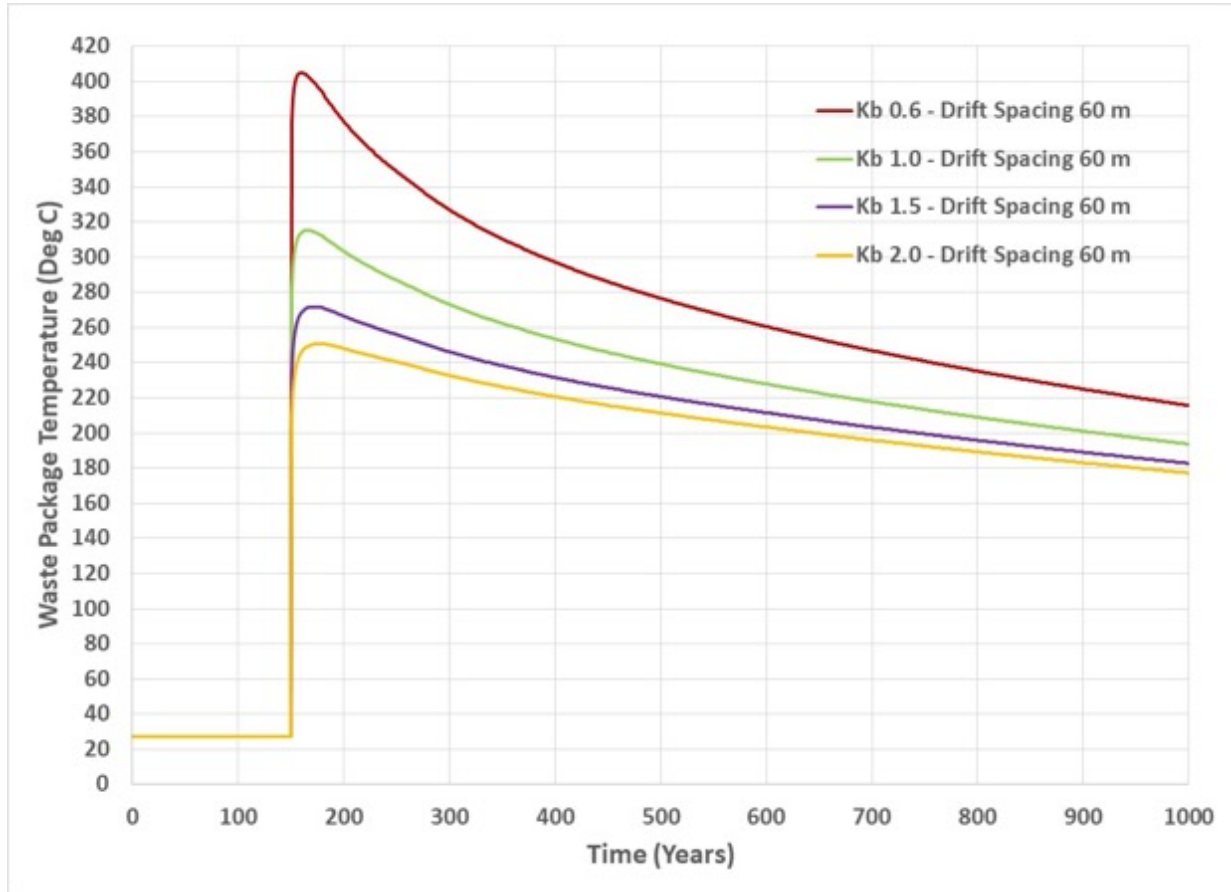
NOTE:   Time given by the *x*-axis refers to time out of the reactor.

Kb = thermal conductivity of buffer

**Figure 2-6.  Waste package surface temperature prediction for
different buffer thermal conductivity values**

Figure 2-6 shows predicted waste package temperature versus time for different buffer thermal
conductivity values. The plots show significant reduction in peak temperature for larger thermal
conductivity values. For buffer thermal conductivity 0.6 W/(m·K), representing dry bentonite, the
predicted peak waste package temperature is 405.0°C. Such high temperatures may affect the integrity of
the EBS and the host rock.
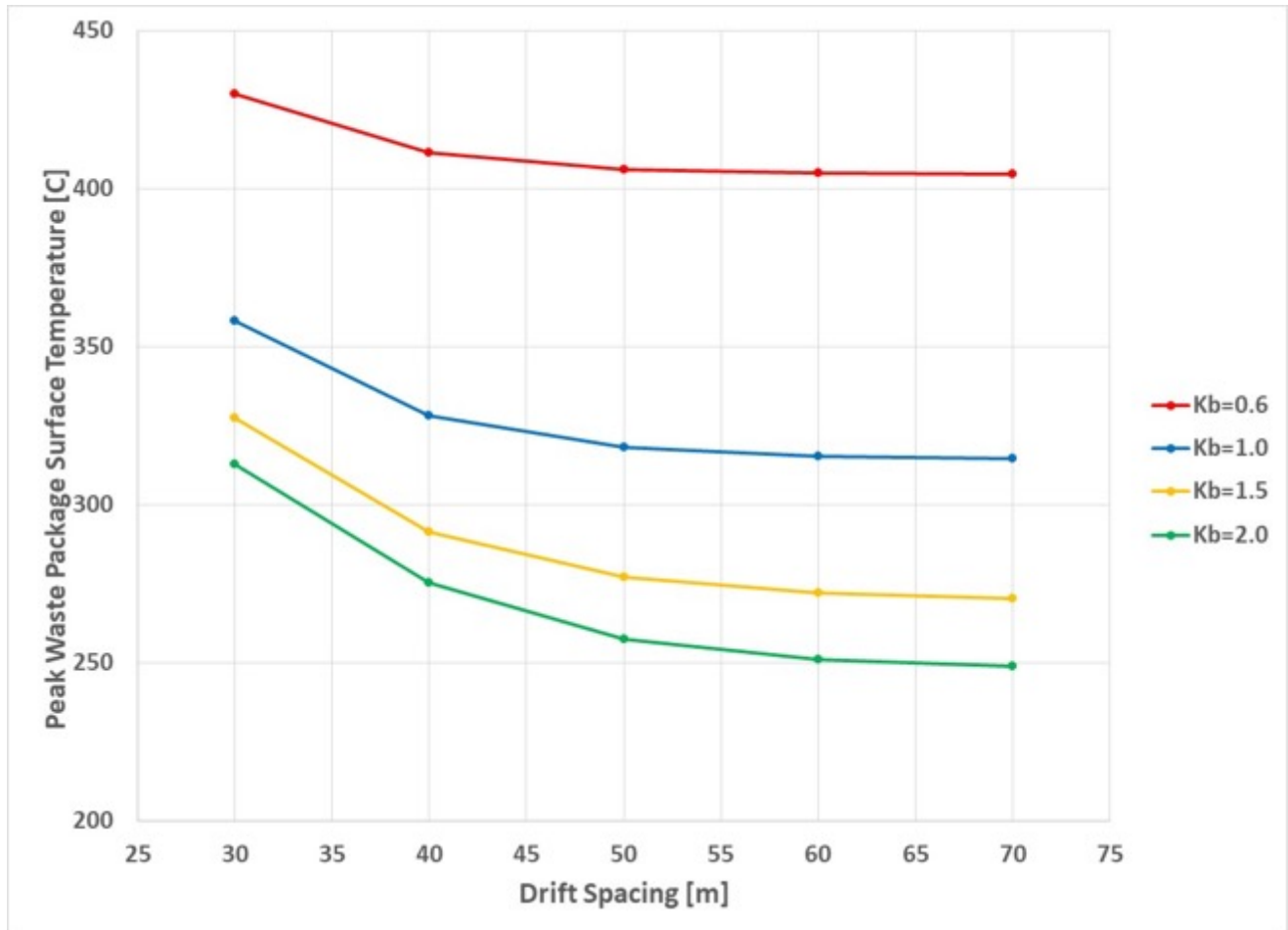
NOTE:    Kb = thermal conductivity of buffer

**Figure 2-7.  Peak waste package surface temperatures as a function
of drift spacing for different buffer thermal conductivity**

Figure 2-7 shows peak waste package surface temperature versus drift spacing for different buffer thermal conductivity values. Table 2-1, Table 2-2, Table 2-3, and Table 2-4 show corresponding peak temperatures. Figure 2-7 and the tables show sensitivity of peak temperature to drift spacing decreases for spacings larger than 50 m. That is also the case for higher buffer thermal conductivity values. As also shown in Figure 2-6, significant reductions in peak temperature occur for buffer thermal conductivity values of 1.0 W/(m·K) and higher. Thus, for the disposal of DPCs use of buffer material engineered to increase thermal conductivity would be beneficial. Figure 2-7 shows use of buffer thermal conductivities of 1.5 or 2.0 W/(m·K) would reduce peak temperatures below 300°C. This is further studied by varying one more parameter (i.e. surface storage time) as shown in Figure 2-8.

Table 2-1, Table 2-2, Table 2-3, and Table 2-4 provide peak waste package surface and drift wall temperatures for different drift spacing and buffer thermal conductivity values. For buffer thermal conductivity value of 0.6 W/(m·K) and drift spacing values of 30 to 70 m, waste package surface temperatures vary between 430.1°C and 404.8°C. If an engineered buffer is used with thermal conductivity of 2.0 W/(m·K), use of the range of drift spacing values result in waste package surface temperatures of 312.8°C to 248.7°C. The results indicate that peak temperatures could be optimized if a buffer thermal conductivity could be engineered appropriately. In addition, drift spacing could be optimized to reduce repository foot print.
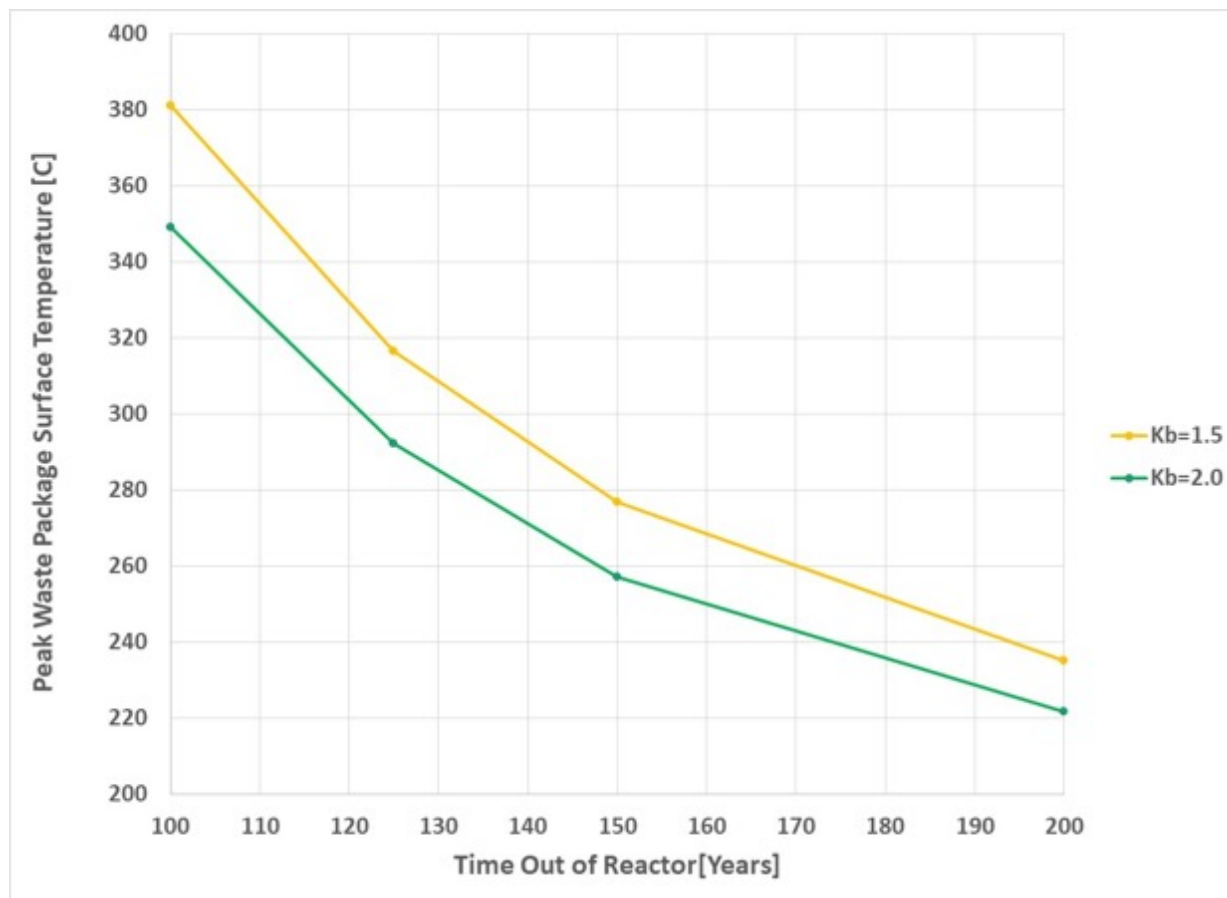
NOTE:    Kb = thermal conductivity of buffer

**Figure 2-8.  Peak waste package surface temperature as a function
of surface storage time for two buffer thermal conductivity values**

Figure 2-8 shows peak waste package surface temperature versus surface storage time (i.e., time out of reactor) for two different buffer thermal conductivity values. It is obvious that the decay heat dissipates at longer times and thus longer surface storage would reduce the heat. For buffer thermal conductivity of 1.5 W/(m·K), storage of 135 years is sufficient to reduce peak waste package temperature below the 300°C goal; storage to 200 years would reduce peak waste package surface temperature to 235.2°C. If the buffer thermal conductivity was 2 W/(m·K), then 122 years of storage would be sufficient.

Alternatively, peak temperatures can be lowered by placing a small number of assemblies in a waste package. Table 2-1, Table 2-2, Table 2-3, and Table 2-4 show peak waste package surface and drift wall temperatures for different buffer thermal conductivity, drift spacing and waste package spacing values.
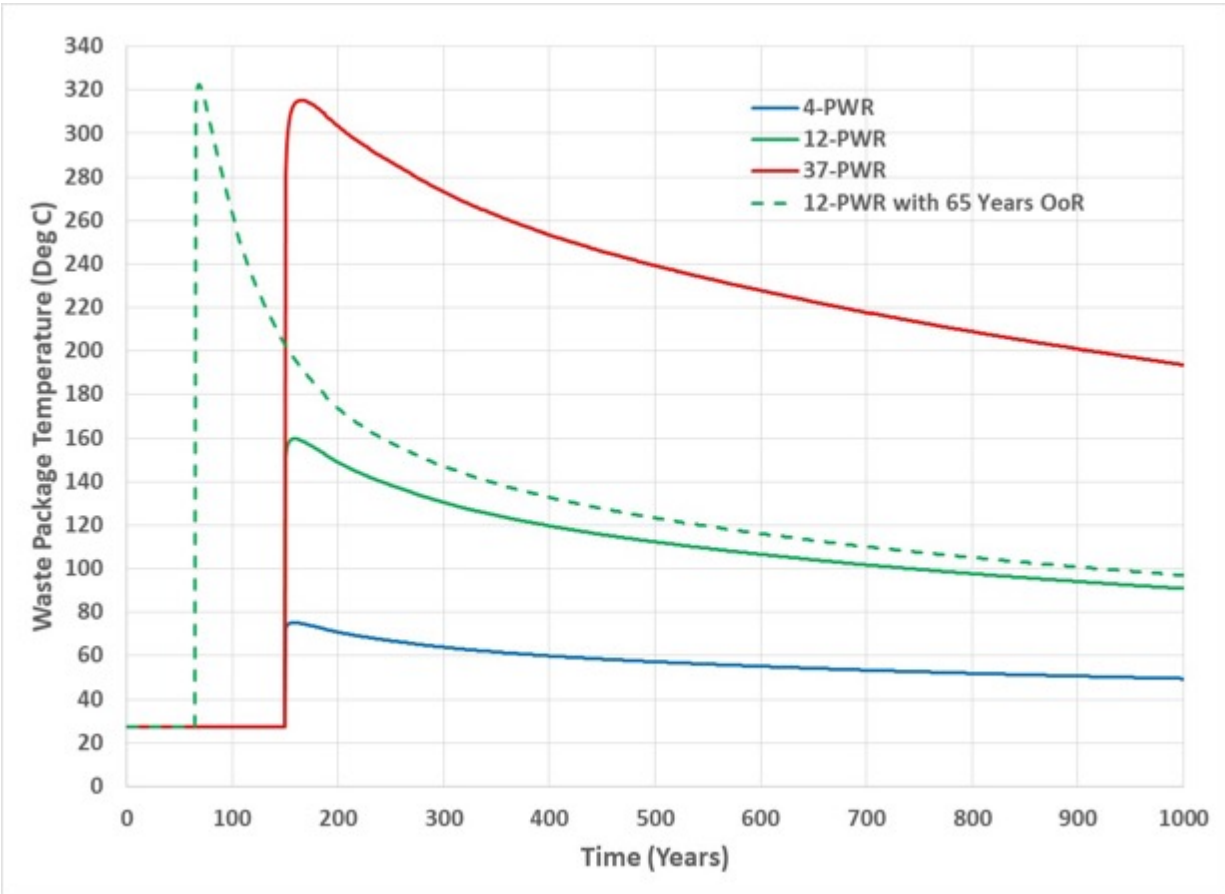
NOTE:    12-PWR shown by green dashed line is emplaced after 65 years of storage (out-of-reactor (OoR) time); assemblies with solid lines are emplaced after 150 years of storage.

PWR = pressurized water reactor

**Figure 2-9.  Effect of number of assemblies per waste package
on waste package surface temperature**

Figure 2-9 shows waste package surface temperature as a function of time for different numbers of assemblies in the waste package. Reducing the waste package power to 12-PWR would significantly reduce the peak temperature to 160°C (from 315.3°C for 37-PWR). Figure 2-9 also shows a plot for 12-PWR with 65 years surface storage time. The figure indicates that for similar peak waste package surface temperature as 37-PWR, the storage time could be significantly reduced. These are significant reductions in peak temperature but would require re-packaging DPCs.
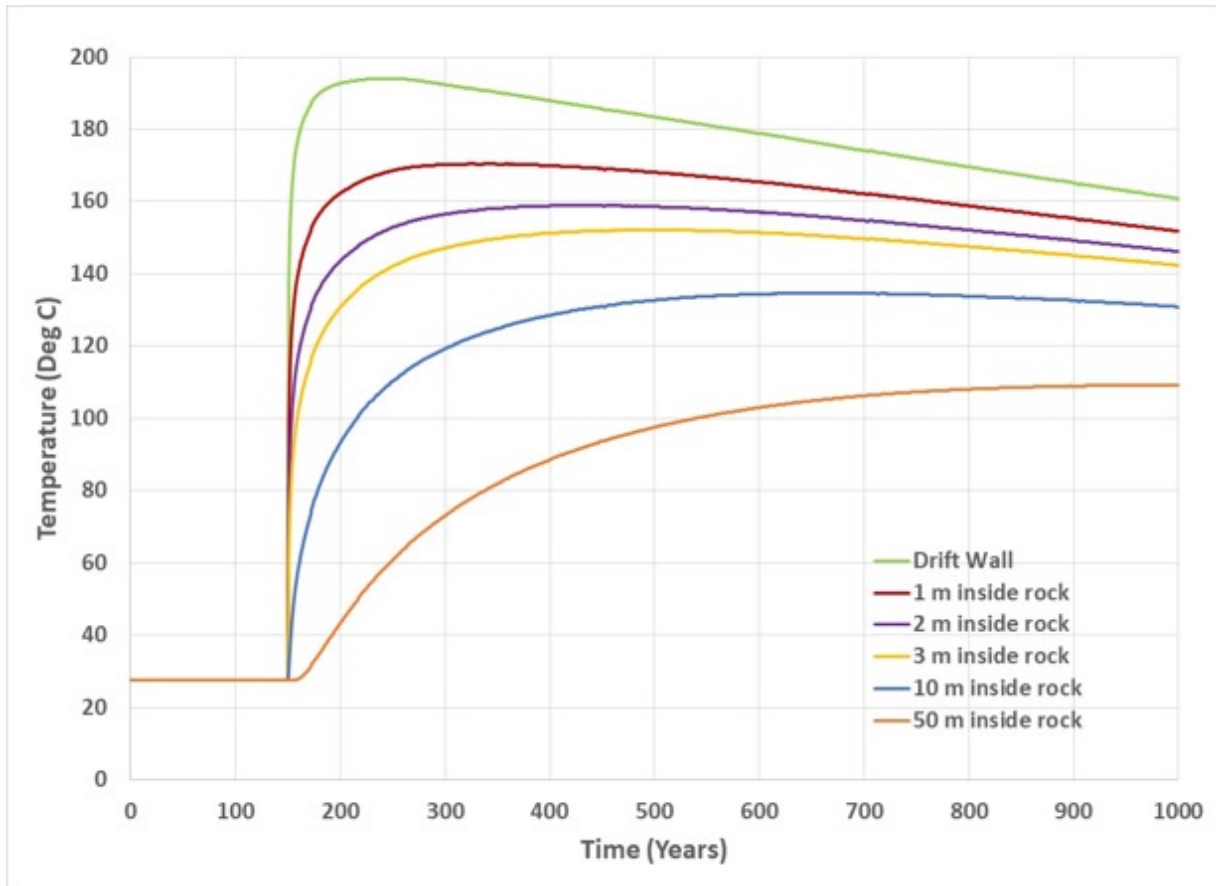
NOTE:    Time given by the *x*-axis refers to time out of the reactor.

**Figure 2-10.  Prediction of host rock temperature at different radial distances from drift wall**

Besides the peak waste package surface temperature and buffer temperature, temperature increases in the rest of the EBS and the host rock are also important to system integrity. Figure 2-10 shows predicted rock temperature at different distances from the drift wall. The calculations were done for the base case. The figure shows elevated temperatures for a long period of time. At 50-m radius from the central waste package temperatures rise to above 100°C. Reducing the peak waste package surface temperature will also reduce host rock temperatures.

The simulations also looked at the sensitivity of host rock thermal diffusivity to waste package surface temperature. A rock thermal diffusivity value of $8.22 \times 10^{-7}$ m²/s was selected for the base case. Based on Equation 2-1 below, the thermal diffusivity represents a volumetric heat capacity of $1.46 \times 10^{6}$ J/(m³·K) for the base case thermal conductivity of 1.2 W/(m·K). Sensitivity of rock thermal diffusivity was studied by using a reduced thermal diffusivity of $4.80 \times 10^{-7}$ m²/s (i.e. increasing volumetric heat capacity to $2.5 \times 10^{6}$ J/(m³·K) for the same rock thermal conductivity). Figure 2-11 shows waste package surface temperature for the two thermal diffusivity values. Using the lower thermal diffusivity value reduces the peak temperature by about 11°C.

$$\alpha = \frac{k}{\rho c_p}$$                                                                                       *Equation 2-1*

where   $\alpha$ = thermal diffusivity [m²/s]

       k = thermal conductivity [W/(m·K)]

      $\rho c_p$= volumetric heat capacity [J/(m³·K)]
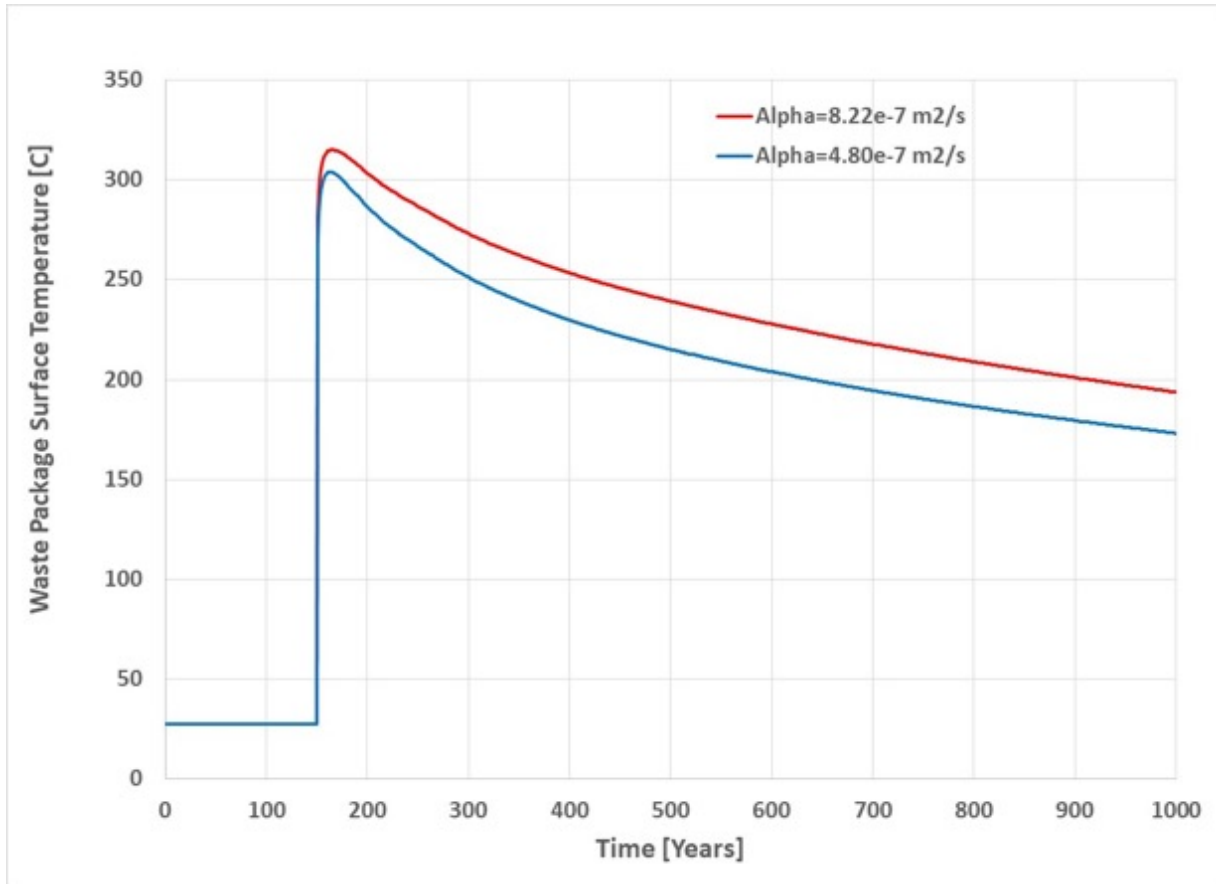


NOTE:   Time given by the *x*-axis refers to time out of the reactor.

        Alpha = thermal diffusivity

**Figure 2-11.  Effect of thermal diffusivity on waste package temperature**

## 2.3    Summary of Semi-analytical, Thermal Analysis

Semi-analytical, thermal calculations were conducted for the disposal of DPCs for the closed-mode, sedimentary repository concept. The calculations support GDSA PFLOTRAN-based PA simulations. Direct disposal of DPCs would result in high thermal loads due to the large number of PWR assemblies in the waste package. They would need large surface area to effectively dissipate heat. Thus, repository foot print is one important parameter. The calculations looked at combinations of parameters that would affect thermal conditions in the EBS and the host rock. The predicted results showed that a combination of a larger repository foot print, a longer surface storage time, and an engineered buffer with higher thermal conductivity would be required to control peak temperatures. Alternative disposal concepts were also shown as part of sensitivity analysis. The results are in line with previous analyses.

# 3.   TETRAVALENT URANIUM SOLUBILITY AND SPECIATION

## 3.1   Introduction

Understanding the controls on the behavior of U at hydrothermal conditions is essential in risk assessment associated with geological disposal of nuclear waste, especially for evaluating the effects of breaching engineered barriers and flooding waste with ground waters or deep saline fluids (e.g., Grambow and Bretesché 2014; Ewing 2015). Nuclear waste is heated by radioactive decay to temperatures typical of hydrothermal systems, and potential contact with aqueous solutions can mobilize uranium, transport it, and cause undesired contamination of the environment (e.g., Burns et al. 2012). Considering these risks and determing if mitigation measures will be necessary requires quantitative models of the processes occurring at elevated temperatures, and, thus, quantitative understanding of the behavior of U-bearing solid phases and aqueous complexes at these conditions.

In nature, uranium occurs predominantly in either the U(IV) or U(VI) oxidation state (e.g., Bastrakov et al. 2010). While the latter, oxidized state is highly mobile and known to form soluble solids and high stability aqueous species, reduced U(IV) is traditionally assumed to be highly insoluble and generally unable to develop significant concentrations in aqueous solutions (Guillaumont et al. 2003). Many existing mobilization/deposition models take into account this effect, and suggest that the change of oxidation regimes, when the system switches between predominance of U(IV) and U(VI), is the main factor controlling uranium mobilization and deposition (e.g., Komninou and Sverjensky 1995; Cuney 2009; Richard et al. 2011; Haynes et al. 1995). Low temperature experimental data (Guillaumont et al. 2003) support these conceptual models, and are able to sufficiently explain natural, low- and medium-temperature hydrothermal behavior (e.g., Ahonen et al. 1994; Sunder et al. 1996; Rich et al. 1977).

However, our recent experimental data on the stability of U(IV) complexes at temperatures above 200°C call into question the applicability of these conventional models at elevated temperatures (Timofeev et al. 2018). These data demonstrate that, at high temperatures, uranium (IV) chloride complexes become highly stable, and, at low pH, the solubility of uranium oxides becomes comparable to that in oxidizing systems. In addition to challenging the established reducing-ensures-immobilizing paradigm, these findings emphasize the paucity of experimental work on high temperature U(IV) complexation. Existing experimental studies devoted to the complexation of U(IV) at elevated temperature are restricted to those of Parks and Pohl (1988) and Tremaine et al. (1981), which evaluate stability of U(IV)-hydroxyl complexes. Stabilities of other complexes of U(IV) (chloride, sulfate, carbonate, etc.) have largely been considered insignificant (Grenthe et al. 1992; Guillaumont et al. 2003) until the study of Timofeev et al. (2018), and have received little attention. Thus, one important conclusion from Timofeev et al. (2018) is the necessity for additional experimental studies of high-T interaction of U(IV) with other ligands in aqueous solutions.

Sulfate is abundant in seawater (Millero et al. 2008), it played an active role in the Fukushima disaster, it is likely to be present in water that interacts with nuclear waste at disposal sites (Cheshire et al. 2014; Caporuscio et al. 2017; Cheshire et al. 2018), and it is also a component of many uranium-ore forming fluids (e.g., Gammons et al. 2003; Kister et al. 2005). Previous experimental studies performed at ambient and near-ambient temperatures demonstrate high affinity of U(IV) to the sulfate ligand and high stability of $USO_4^{2+}$ and $U(SO_4)_2$ aqueous species, relative to other U(IV) complexes (Perez et al. 1980; Hennig et al. 2007). Therefore, the main goal of this study is to experimentally investigate speciation of U(IV) in sulfate-bearing solutions at elevated temperatures, and to derive quantitative thermodynamic data characterizing the stability of observed uranium sulfate species.

## 3.2   Experimental Technique

The experiments involved determination of the solubilities of uraninite ($UO_2^{cryst}$) in aqueous solutions of various chemistries (pH, sulfate), and were conducted at controlled redox conditions (employing solid state redox buffers), saturated water vapor pressure (swp), and temperatures of 250°C, 300°C, and 350°C (200°C experiments are still in progress and will not be reported here). The experiments were performed in light-weight test tube-size autoclaves (35 to 40 cm³ internal volume), manufactured from Titanium Grade 2, which were passivated with a layer of $TiO_2$ to ensure its chemical inertness. Experiments performed at T < 300°C were conducted in autoclaves with Teflon liners. Since Teflon melts and decomposes at 270°C, in experiments at 300°C and 350°C, the Teflon liners were not used. The experimental technique employed in this study is similar to that reported in Timofeev et al. (2018), except that the solutions with a range of concentrations of sulfate, rather than chloride, were used here. For details not covered in the following sections, readers are referred to Timofeev et al. (2018).

Experimental solutions were prepared from de-ionized, $CO_2$-free water and $Na_2SO_4$ (Fisher Scientific, A.C.S.) with concentrations ranging from 0.05 to 0.55 mol/L (Table 3-1). Solutions' $pH_{25°C}$ were adjusted to approximately 2 using HCl (Fisher Scientific, Optima grade). All experimental solutions were prepared to have NaCl (Fisher Scientific, A.C.S.) as a background electrolyte at concentrations of 1 m because the most reliable and experimentally best-tuned activity model applicable to high temperatures is that developed by Helgeson et al. (1981), Oelkers and Helgeson (1990), and Oelkers and Helgeson (1991) for NaCl-dominated solutions (recommended for up to I = 6 and T up to 600°C).

**Table 3-1.   Composition of experimental solutions, solid state buffer used, $pH_{25°C}$ measured after quenching, and $pH_T$ extrapolated to experimental temperature**

| T (°C) | Buffer | $Na_2SO_4$ initial (mol/kg) | $Na_2SO_4$ HPLC (mol/kg) | NaCl (mol/kg) | $pH_{25°C}$ | $pH_T$ | U (ppm) | U log m |
|--------|--------|------|------|------|------|------|------|------|
| 250 | Ni/NiO | 0.001 | 0.001 | 1.0 | 3.300 | 3.803 | 0.065 | −6.483 |
| 250 | Ni/NiO | 0.005 | 0.005 | 1.0 | 2.880 | 3.821 | 0.287 | −5.840 |
| 250 | Ni/NiO | 0.008 | 0.008 | 1.0 | 2.740 | 3.855 | 0.409 | −5.685 |
| 250 | Ni/NiO | 0.01 | 0.010 | 1.0 | 2.650 | 3.841 | 0.655 | −5.481 |
| 250 | Co/CoO | 0.025 | 0.027 | 1.0 | 2.350 | 3.932 | 0.958 | −5.316 |
| 250 | Co/CoO | 0.05 | 0.054 | 1.0 | 2.150 | 4.026 | 1.160 | −5.233 |
| 250 | Ni/NiO | 0.08 | 0.083 | 1.0 | 2.090 | 4.187 | 1.164 | −5.231 |
| 250 | Ni/NiO | 0.1 | 0.103 | 1.0 | 1.990 | 4.168 | 1.376 | −5.159 |
| 250 | Ni/NiO | 0.025 | 0.025 | 1.0 | 2.960 | 4.623 | 0.061 | −6.512 |
| 250 | Ni/NiO | 0.025 | 0.026 | 1.0 | 2.900 | 4.555 | 0.069 | −6.459 |
| 250 | Ni/NiO | 0.025 | 0.026 | 1.0 | 2.630 | 4.264 | 0.312 | −5.803 |
| 250 | Co/CoO | 0.025 | 0.026 | 1.0 | 2.570 | 4.199 | 0.379 | −5.718 |

**Table 3-1. Composition of experimental solutions, solid state buffer used, $pH_{25°C}$ measured after quenching, and $pH_T$ extrapolated to experimental temperature (continued)**

| T (°C) | Buffer | Na$_2$SO$_4$ initial (mol/kg) | Na$_2$SO$_4$ HPLC (mol/kg) | NaCl (mol/kg) | $pH_{25°C}$ | $pH_T$ | U (ppm) | U log m |
|--------|--------|--------|--------|--------|--------|--------|--------|--------|
| 250 | Co/CoO | 0.025 | 0.025 | 1.0 | 2.560 | 4.186 | 0.368 | −5.732 |
| 250 | Ni/NiO | 0.025 | 0.026 | 1.0 | 2.510 | 4.130 | 0.348 | −5.756 |
| 250 | Ni/NiO | 0.025 | 0.027 | 1.0 | 2.310 | 3.876 | 1.013 | −5.292 |
| 250 | Ni/NiO | 0.025 | 0.026 | 1.0 | 2.130 | 3.625 | 3.764 | −4.722 |
| 300 | Ni/NiO | 0.05 | 0.046 | 1.0 | 2.353 | 4.555 | 1.171 | −5.309 |
| 300 | Ni/NiO | 0.05 | 0.042 | 1.0 | 2.165 | 4.754 | 0.283 | −5.925 |
| 300 | Ni/NiO | 0.25 | 0.239 | 1.0 | 2.091 | 4.689 | 2.336 | −5.009 |
| 300 | Ni/NiO | 0.25 | 0.260 | 1.0 | 1.997 | 4.751 | 0.923 | −5.412 |
| 300 | Co/CoO | 0.25 | 0.248 | 1.0 | 2.314 | 4.929 | 0.633 | −5.576 |
| 300 | Ni/NiO | 0.35 | 0.354 | 1.0 | 2.091 | 4.851 | 1.717 | −5.142 |
| 300 | Ni/NiO | 0.35 | 0.313 | 1.0 | 2.227 | 5.100 | 0.719 | −5.520 |
| 300 | Ni/NiO | 0.45 | 0.451 | 1.0 | 2.095 | 4.894 | 1.306 | −5.261 |
| 300 | Ni/NiO | 0.55 | 0.546 | 1.0 | 2.050 | 4.880 | 1.451 | −5.215 |
| 350 | Ni/NiO | 0.05 | 0.053 | 1.0 | 2.436 | 5.261 | 0.067 | −6.550 |
| 350 | Co/CoO | 0.05 | 0.034 | 1.0 | 2.036 | 4.723 | 0.293 | −5.910 |
| 350 | Ni/NiO | 0.05 | 0.034 | 1.0 | 1.897 | 4.480 | 1.595 | −5.174 |
| 350 | Ni/NiO | 0.15 | 0.144 | 1.0 | 2.110 | 5.189 | 0.602 | −5.597 |
| 350 | Co/CoO | 0.15 | 0.135 | 1.0 | 2.133 | 5.216 | 0.665 | −5.555 |
| 350 | Ni/NiO | 0.15 | n.a. | 1.0 | 1.709 | 4.674 | 1.420 | −5.225 |
| 350 | Ni/NiO | 0.25 | 0.222 | 1.0 | 1.836 | 4.968 | 2.905 | −4.914 |
| 350 | Ni/NiO | 0.25 | 0.232 | 1.0 | 2.050 | 5.211 | 0.381 | −5.797 |
| 350 | Co/CoO | 0.25 | 0.264 | 1.0 | 2.193 | 5.371 | 0.253 | −5.975 |
| 350 | Ni/NiO | 0.35 | 0.351 | 1.0 | 2.051 | 5.254 | 0.615 | −5.588 |
| 350 | Co/CoO | 0.35 | 0.336 | 1.0 | 2.288 | 5.504 | 0.294 | −5.908 |

NOTE:     HPLC = high performance liquid chromatography

Before each experiment the autoclaves were loaded with $UO_2$ (99.8% International Bio-Analytical Industries, Inc.) and solid-state redox buffers (Ni/NiO or Co/CoO; Fisher Scientific, 99.95%), which were contained in separate 1- to 3-mm diameter quartz holders (fused quartz tubes with their upper ends open; Technical Glass Products). Then an aliquot of experimental solution was added. The technique employs the separated phases approach and uses the effect of thermal expansion of solutions; the volume of added aliquot is calculated to ensure the solution is not in contact with $UO_2$ at ambient conditions, but will expand and flush the holder at the experimental temperature (Figure 3-1). After completion of the experiments and quenching the autoclaves, the solutions contract and lose contact with $UO_2$. This approach ensures that the solubility determined in the experiments corresponds to the experimental temperature only and is not affected by the processes that may occur during heating/quenching of the autoclaves. The holders containing solid-state redox buffers were sufficiently long (~10 cm) to ensure that experimental solutions never contact the redox buffers, and $fO_2$ re-equilibration occurred through the gas phase (Figure 3-1). In order to accelerate $fO_2$ re-equilibration and to avoid unnecessary consumption of the buffers by atmospheric oxygen, autoclaves were purged with high purity Argon gas (Matheson Tri Gas, Ultrapure) immediately before being capped and sealed using a Grafoil® O-ring.
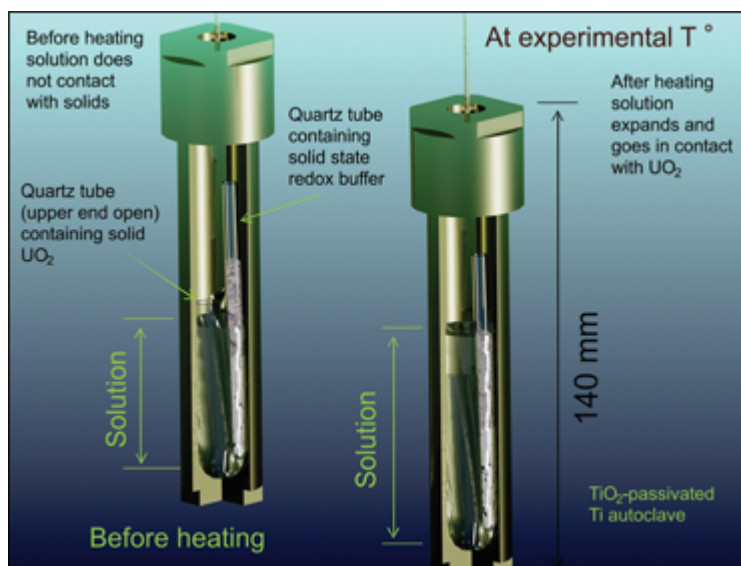


**Figure 3-1. Sketch of the experimental setup used in this study**

Autoclaves were thermostated in a ThermoFisher Scientific Thermolyne Largest Tabletop Muffle Furnace (±0.5°C). After the experiments, autoclaves were air quenched until solution reached room temperature, holders containing $UO_2$ and $fO_2$ buffers were removed and aliquots of post-experimental solutions were taken for pH and sulfate measurements. The sulfate concentration was analyzed using high performance liquid chromatography (HPLC), and the pH was measured potentiometrically using an Orion glass double junction electrode and a set of calibration standards matching $NaCl/Na_2SO_4$ concentrations in experimental solutions. Thereafter 3 to 5 ml of concentrated $HNO_3$ (Fisher Scientific, TM grade) was added to the autoclave to dissolve any uranium which may have precipitated on the inside walls of the autoclave during cooling. To ensure complete dissolution, autoclaves were soaked with acid overnight before an aliquot of the acidified experimental solution was taken to measure the total dissolved uranium.

Concentrations of U in the resulting solution were measured using inductively coupled plasma–mass spectrometry (ICP-MS) technique and confirmed by kinetic phosphorimetry analysis (KPA). Two sets of blank experiments (no $UO_2$ holders added) were also performed to ensure that any uranium deposited on the autoclave walls was dissolved during the overnight acid soak. ICP-MS analysis showed that any residual uranium concentrations were negligible, and any uranium solids possibly precipitated during cooling were removed during the overnight soaking. Finally, to ensure that the measured solubility corresponded only to the dissolution of $UO_2$, post experiment holders were selected randomly, and the collected solids were analyzed by x-ray diffraction (XRD). An example of the XRD patterns taken from post-experimental solids is shown in Figure 3-2, which reveals no alteration of the reference $UO_2$ phase during the solubility experiments.
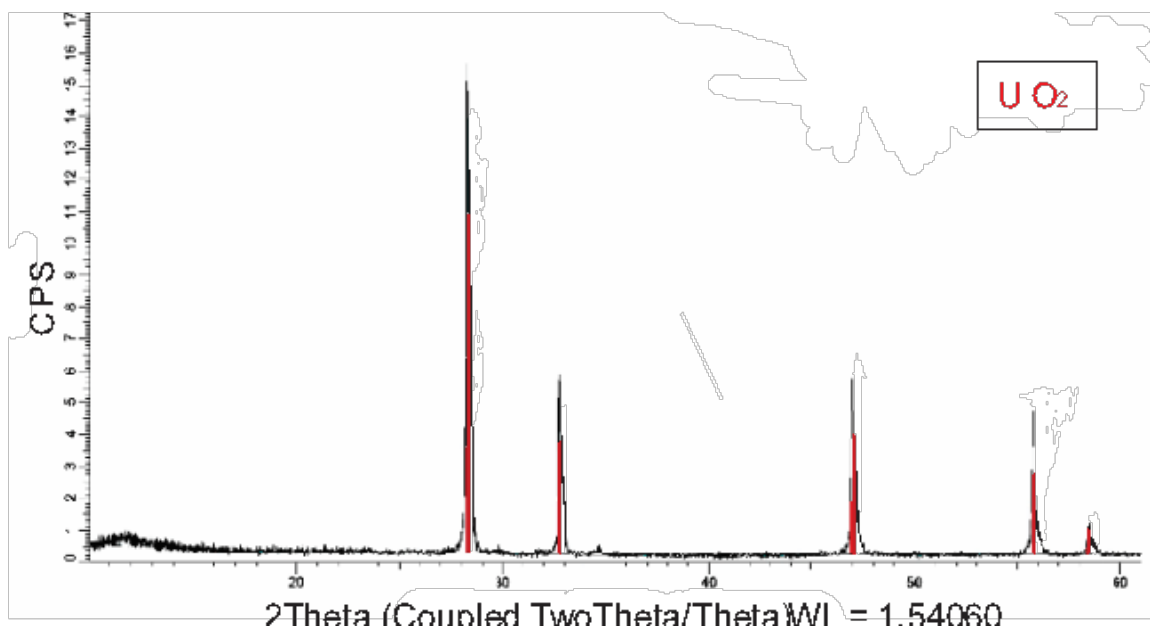


**Figure 3-2. XRD pattern showing the close match between predicted diffraction peaks for $UO_2$ (red) and those observed in the experiment (black)**

Most experiments were performed using Ni/NiO solid state redox buffers ($Ni^{metal}+0.5O_2^{gas} = NiO^{solid}$). However, a few controlled determinations were also performed at each isotherm with a Co/CoO solid state redox buffer. These experiments allowed verification of our assumption that the data collected at Ni/NiO conditions correspond to the predominance of U(IV) species in aqueous solutions, while uranyl complexes (U(VI)) do not contribute significantly to the mass balance of dissolved U. If dissolution of $UO_2$ is mostly controlled by U(IV) aqueous species, this process is redox-independent, and the data collected for the same solution, but different redox conditions (Ni/NiO and Co/CoO set ~3 orders of magnitude different $fO_2$) should be identical, e.g.
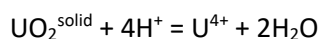
$$UO_2{}^{solid} + 4H^+ = U^{4+} + 2H_2O \qquad\qquad \textit{Equation 3-1}$$

However, if uranyl species predominate in the aqueous solution, solubility of $UO_2$ turns into a redox-dependent process, and the data should differ significantly, e.g.

$$UO_2^{solid} + 2H^+ + 0.5O_2^{gas} = UO_2^{2+} + H_2O \qquad \text{Equation 3-2}$$
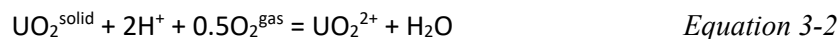
Agreement between the data collected at Ni/NiO and Co/CoO conditions was therefore considered as a criterion of the predominance of U(IV) species in aqueous solution.

In addition to the redox control series, a set of 7 experiments with identical sulfate concentration and pH (pH = 2.1–2.3, $Na_2SO_4$ = 0.4 mol/kg) were performed at 250°C for durations of 1 to 7 days to determine the time needed to reach the equilibrium (Figure 3-3). After four days at 250°C, uranium concentrations reached a plateau where they remained for the duration of the experiments. Since equilibrium will be reached faster at elevated temperatures, the reproducible, consistent uranium concentrations after four days suggest that the concentrations measured for the experiments exceeding four days correspond to those of isothermal solubility. Hence, all experiments reported in this study were performed for a minimum of six days.
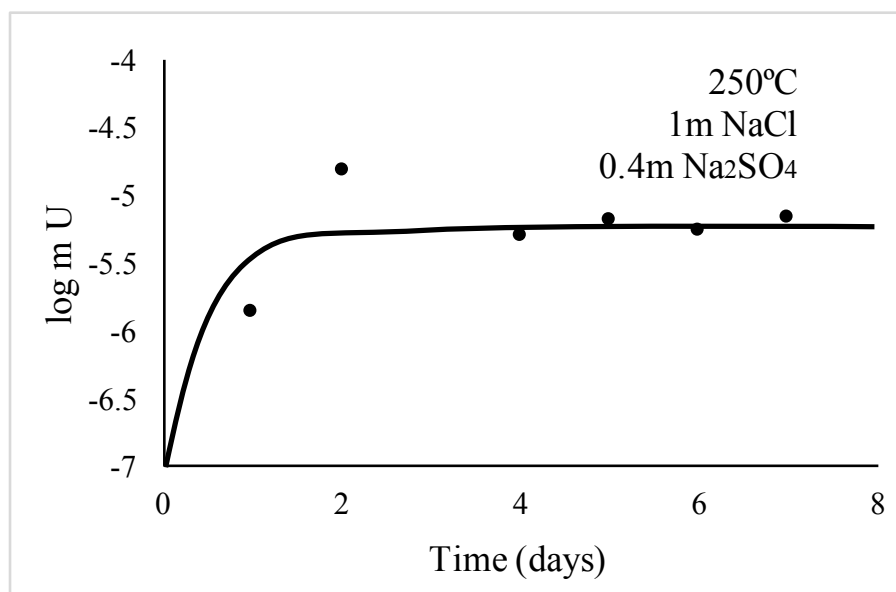


NOTE:   Equilibrium was reached after approximately three days.

**Figure 3-3.  Series of kinetic experiments performed at 250°C**

## 3.3   Results and Preliminary Data Treatment

The results of the solubility experiments are summarized in Table 3-1. The table also lists the concentrations of total sulfate set in experimental solutions prior to heating ($Na_2SO_4$ initial) and those determined in the solutions after the experiments ($Na_2SO_4$ HPLC). As it can be seen from the table, the concentrations of total sulfate determined in post-experimental solutions are effectively indistinguishable

from initial concentrations (within the experimental error). The latter effect does not reflect equilibrium state, and rather corresponds to the steady state conditions. Indeed, redox conditions employed in the experiments correspond to the predominance fields of $H_2S$ and $HS^-$ species (Figure 3-4(a)), and, if equilibrium is established, sulfate must represent a very minor proportion of dissolved sulfur at these conditions. It is known however that thermochemical sulfate reduction (TSR) is the process characterized by extremely slow kinetics, and in many cases requiring variable intermediates, such as polysulfanes or polythionates, to be initiated (Goldstein and Aizenshtat 1994; Thom and Anderson 2008; Ellis et al. 2016; Li et al. 2017). It is evident from the table that this process has not been initiated (or has been initiated at undetectable extent) in our experiments. In the following derivations we assumed the "frozen" redox equilibria of sulfur in experimental solutions and that the determined concentrations of sulfate (not sulfide or hydrosulfide) fully control speciation of uranium.

Notably, uranium concentrations experimentally determined at elevated temperatures (250°C, 300°C, and 350°C) are unexpectedly high. In some experiments, they reach values of up to 3.5 ppm, which is seven to eight orders of magnitude greater than concentrations predicted in a system without sulfate or chloride complexes, based on the data reported in Shock et al. (1997a). The table also lists the values of $pH_{25°C}$ and $pH_T$, which were calculated for experimental temperatures using the measured $pH_{25°C}$ and post-experiment solution composition.

All calculations reported here employed the extended Debye-Huckel model modified by Helgeson et al. (1981), Oelkers and Helgeson (1990), and Oelkers and Helgeson (1991) for NaCl-dominated solutions:

$$\log \gamma_i = -\frac{A \cdot [Z_i]^2 \cdot \sqrt{I}}{1 + B \cdot \mathring{a} \cdot \sqrt{I}} + \Gamma + b_\gamma I \qquad \text{\textit{Equation 3-3}}$$

where $A$ and $B$ are the Debye–Huckel parameters, $Z_i$, $\Gamma$ and $\mathring{a}$ are the individual molal activity coefficient, the charge, a molarity to molality conversion factor and the distance of closest approach of an ion $i$, respectively. The effective ionic strength calculated using the molal scale is $I$ and $b_\gamma$ is the extended-term parameter for NaCl dominated solutions. The initial model used for preliminary calculation of pH and activity of sulfate species included: $H_2O$, $H^+$, $OH^-$, $O_2$, $H_2$, $Na^+$, $NaOH$, $NaSO_4^-$, $NaCl°$, $SO_4^{2-}$, $HSO_4^-$, $Cl^-$, and $HCl°$. Thermodynamic data for these calculations were taken from Johnson et al. (1992), Sverjensky et al. (1997), and Tagirov et al. (1997). Although the pH values initially set in experimental solutions and measured after the experiments ($pH_{25°C}$) are all appreciably acidic, those calculated for experimental temperatures ($pH_T$), especially at 300°C and 350°C, are shifted to near-neutral range. This effect is due to two inter-related factors: 1) sulfuric acid strength significantly decreases with temperature (pK of the dissociation reaction $HSO_4^- = H^+ + SO_4^{2-}$ changes from 1.97 at 25°C, swp, to 7.40 at 350°C, swp; Figure 3-4(b)), and 2) $pH_T$ of experimental solutions is largely controlled by weak acid and strong base due to sulfate concentration in experimental solutions set using $Na_2SO_4$.

In the experiments performed at higher temperatures without Teflon lining (300°C and 350°C), $pH_{25°C}$ shifts more strongly toward alkalinity from the initial values. This effect can be explained by partial (minor) interaction of intrinsic acid with the walls of the autoclaves and neutralization of the acidity of the experimental solutions. Although this shift never exceeds 0.1–0.5 $pH_{25°C}$ units, it leads to significant variability of $pH_T$ and adds additional variability to the controls of $UO_2$ solubility: experimental series initially expected to be performed at constant $pH_T$ do not reflect this condition. Thus, reduction of $UO_2$ solubility data must assume dependence on both $pH_T$ and sulfate concentration.
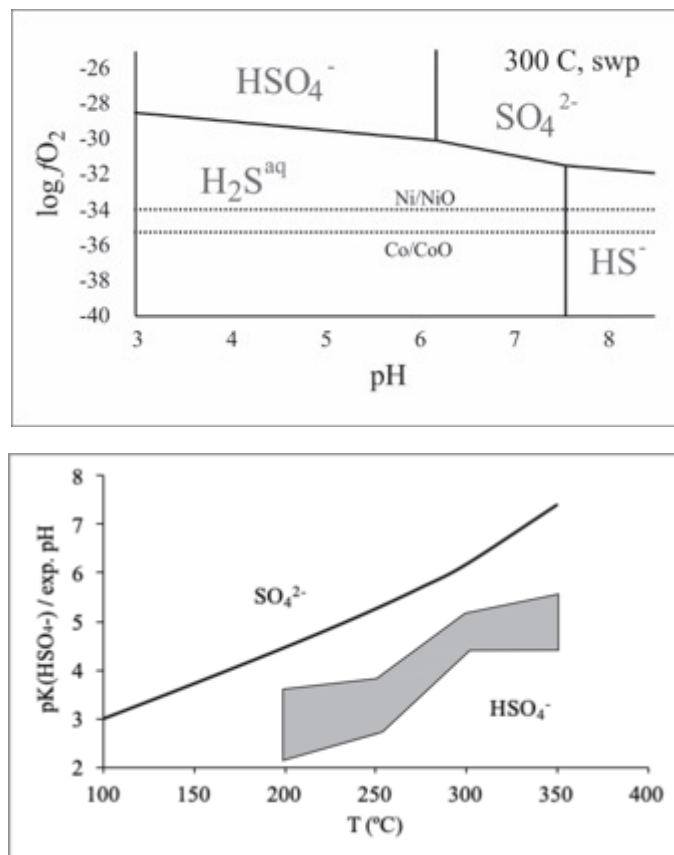
NOTE:    Dashed line in (a) corresponds to the conditions of Ni/Ni and Co/CoO solid state redox buffers.

**Figure 3-4.  (a) Example of Predominance field diagram for sulfur aqueous species at 300°C and Saturated pressure of water, and (b) dissociation constant of sulfuric acid (pK HSO$_4^-$ = H$^+$ + SO$_4^-$) and range of pH$_T$ Investigated as a function of temperature**

**Stoichiometry of the Predominant Species**—Figure 3-5(a),(b), and (c) illustrates the dependencies of the logarithms of measured uranium concentration in the experimental solutions as a function of the logarithms of activity of HSO$_4^-$ (the predominant sulfate species at experimental conditions; see Figure 3-4) calculated for each data point using the above-mentioned model.
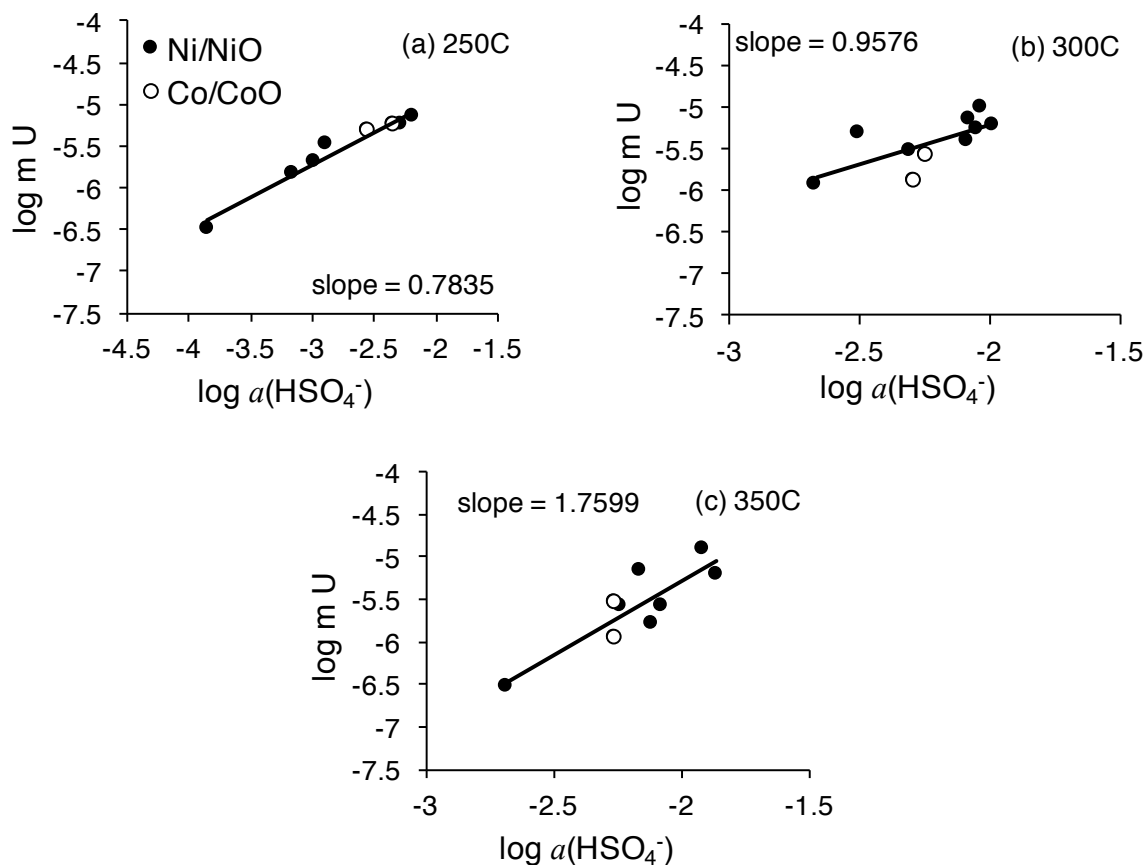
**Figure 3-5.  Logarithms of uranium molality plotted as a function of increasing HSO$_4^-$ activity at three isotherms: (a) 250°C, (b) 300°C, (c) 350°C**

As seen in Figure 3-5, the log m U – log a(HSO$_4^-$) trends obtained have slopes ranging from 0.78 to 1.76. However, it should be noted that these slopes likely do not reflect the stoichiometric ratio of the predominant aqueous species, as these dependencies are the function of two variables: activity of hydrosulfate ion and pH. Changes of pH in experimental series are greatest at 350°C and smaller at 250°C and 300°C, and therefore we assumed to the first approximation that the latter two isotherms closely approximate the stoichiometric ratio of the predominant species (U:HSO$_4^-$ = 1:1). Employing this assumption as a working hypothesis, the data were normalized assuming U:HSO$_4^-$ stoichiometric ratio of 1:1, and then plotted as a function of pH$_T$ to evaluate the contribution of pH to the changes in the UO$_2$ solubility in experimental solutions (Figure 3-6). As can be seen, all isotherms in Figure 3-6 show negative correlation of saturation concentrations of U with pH, which is close to the U:H$^+$ stoichiometric ratio of 1:1.
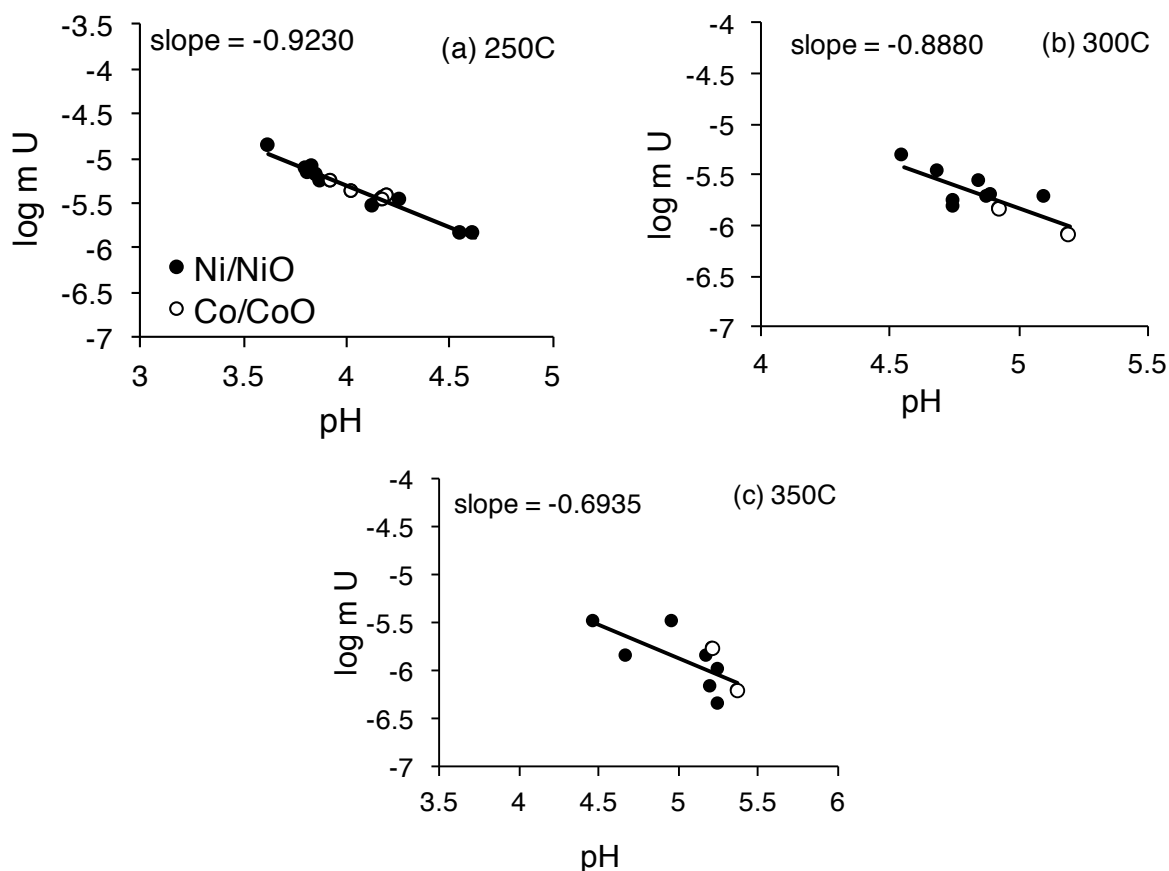
NOTE:   Normalization is used to standardize experimental values to a fixed $HSO_4^-$ activity so that proper stoichiometric slopes can be observed when plotted against pH.

**Figure 3-6.  Logarithms of uranium molality normalized to log $HSO_4^-$ activity of −2.5**

This finding permitted to account for the changing pH in experimental solutions and to validate our initial hypothesis that the species controlling solubility of $UO_2$ in our experiments are characterized by the stoichiometric ratio $U:HSO_4^- = 1:1$. As can be seen from Figure 3-7, the data plotted accounting for the pH dependence, demonstrate a close approximation to the slope of 1.

Along with experiments performed with Ni/NiO solid state buffers, Figure 3-5, Figure 3-6, and Figure 3-7 also plot the data from the experiments performed with Co/CoO buffers. The data collected for Co/CoO-buffered systems are in excellent agreement with those collected using Ni/NiO-buffered systems. This finding validates the assumption that our experimental dissolution of $UO_2$ occurred via redox-independent process and the aqueous species controlling this process are those of U(IV). Based on this finding and the pH and $HSO_4^-$ dependencies discussed above, we conclude that, at all temperatures investigated, the solubility of $UO_2$ determined in experimental solutions is controlled by the following reaction:
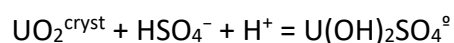
$$UO_2^{cryst} + HSO_4^- + H^+ = U(OH)_2SO_4^{\circ} \qquad\qquad \textit{Equation 3-4}$$
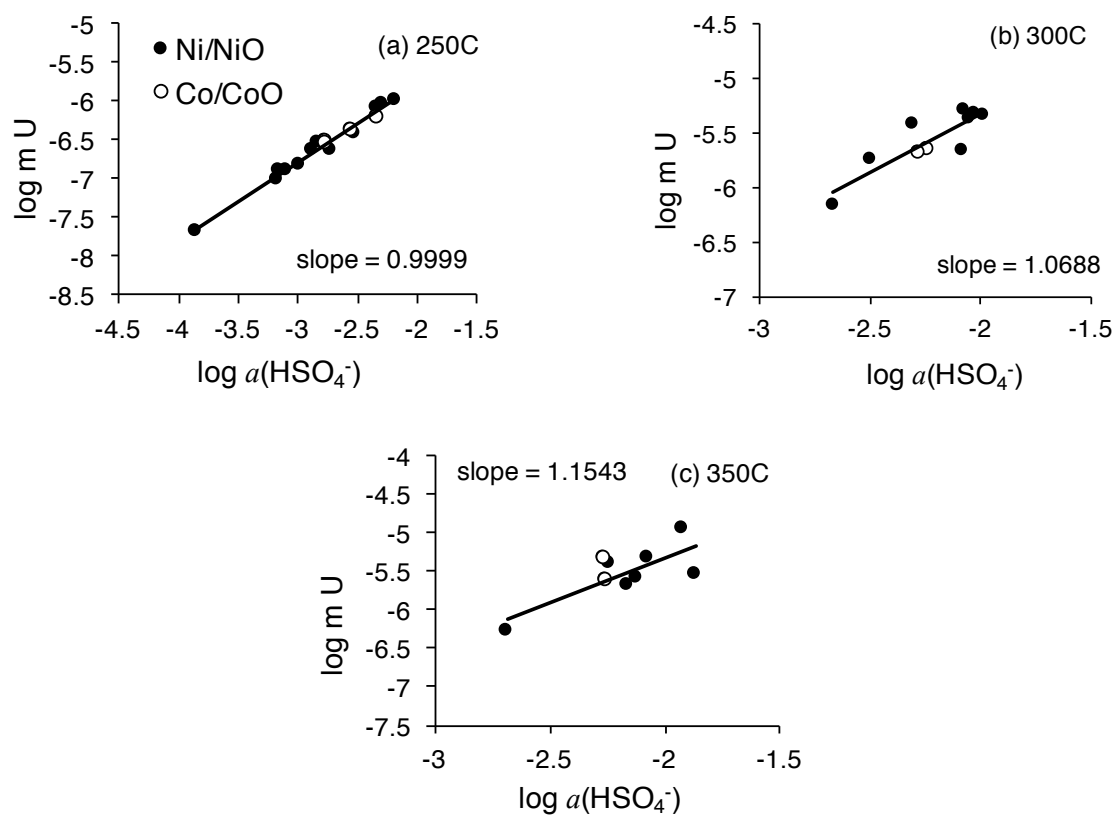
NOTE:   Normalization is used to standardize experimental values to a fixed pH so that proper stoichiometric slopes can be observed when plotted against activity of $HSO_4^-$.

**Figure 3-7.  Logarithms of uranium molality normalized to pH of 5**

## 3.3.1    Data Reduction

In order to take into account all possible complexities in our system, we used the code OptimA (part of the HCh software package) to determine formation constants for each isotherm (Shvarov 2010). The code minimizes the sum of the squared deviations of measured, experimental concentrations of U from those theoretically calculated at equilibrium (Shvarov 2015) by adjusting Gibbs free energy of the species of interest ($U(OH)_2SO_4$). The calculation of the equilibrium state of the chemical system was performed using the HCh package by minimizing its free energy. In addition to the species used for $pH_T$ calculations noted above, chemical description of the system also involved: uraninite, nickel, bunsenite, $U^{4+}$, $UOH^{2+}$, $UO^+$, $HUO_2$, $UO_2^-$, $UOH^{3+}$, $UO^{2+}$, $UO_2$, $HUO_2^+$, $HUO_3^-$, $UO_2^+$, $UO_2OH$, $UO_2^{2+}$, $UO_3^-$, $UO_2OH^+$, $UO_3$, $UO_4^{2-}$, $HUO_4^-$, $UO_2SO_4$, $UO_2(SO_4)_2^{2-}$, $UO_2Cl^+$, $UO_2Cl_2$, and $UCl_4$. Thermodynamic properties of these components were taken from Shock et al. (1997b); Shock et al. (1997a); Guillaumont et al. (2003); Timofeev et al. (2018), and Migdisov et al. (2018). Thermodynamic properties of water and its dissociation constant used in these calculations are from the Haar-Gallagher-Kell model (Kestin et al. 1984) and the Marshall and Franck (1981) model, respectively. Activity coefficients of charged species were calculated using the extended Debye-Huckel equation (Equation 3-3), while activity coefficients of neutral aqueous species were calculated from the simplified version of the extended Debye-Huckel equation:

$$\log \gamma_i = \Gamma + b_\gamma I \qquad\qquad \text{\textit{Equation 3-5}}$$

Using the data available for uraninite (Guillaumont et al. 2003), $U^{4+}$ (Shock et al. 1997c), $HSO_4^-$ and $SO_4^{2-}$ (Johnson et al. 1992; Shock et al. 1997c), the optimized values of the Gibbs free energies were recalculated to the logarithms of the constants (log K = $-\Delta rG/(2.303 \cdot RT)$) for the reaction (Equation 3-4):

$$\Delta rG°_T = \Delta G°_T\ (U(OH)_2SO_4^{\underline{o}})\ - \Delta rG°_T\ (UO_2^{cryst})\ - \Delta rG°_T\ (HSO_4^-) \qquad \text{\textit{Equation 3-6}}$$

$$\Delta G°_T\ (H^+) = 0 \qquad\qquad \text{\textit{Equation 3-7}}$$

and for the formation reaction:

$$U^{4+} + SO_4^{2-} + 2OH^- = U(OH)_2SO_4 \qquad\qquad \text{\textit{Equation 3-8}}$$

$$\Delta rG°_T = \Delta G°_T\ (U(OH)_2SO_4^{\underline{o}}) - \Delta rG°_T\ (U^{4+}) - \Delta rG°_T\ (SO_4^{2-}) - 2\ \Delta rG°_T\ (OH^-) \qquad \text{\textit{Equation 3-9}}$$

The derived formation constants are reported in Table 3-2, along with uncertainties calculated based on the confidence intervals returned by the OptimA code for $\Delta G°_T\ (U(OH)_2SO_4^°)$. The trend of the obtained log K (log $B$) values as a function of temperature ($-1000/TK$) is also illustrated in Figure 3-8.

**Table 3-2.  Logarithms of formation constants for species $U(OH)_2SO_4°$ determined in this study**

|  |  | 250°C | 300°C | 350°C |
|---|---|---|---|---|
| $UO_2^{cryst} + HSO_4^- + H^+ =$ $U(OH)_2SO_4°$ | log K | 1.18±0.09 | 1.65±0.27 | 1.65±0.32 |
| $U^{4+} + SO_4^{2-} + 2OH^- =$ $U(OH)_2SO_4$ | log $B$ | 30.18 | 32.16 | 36.31 |
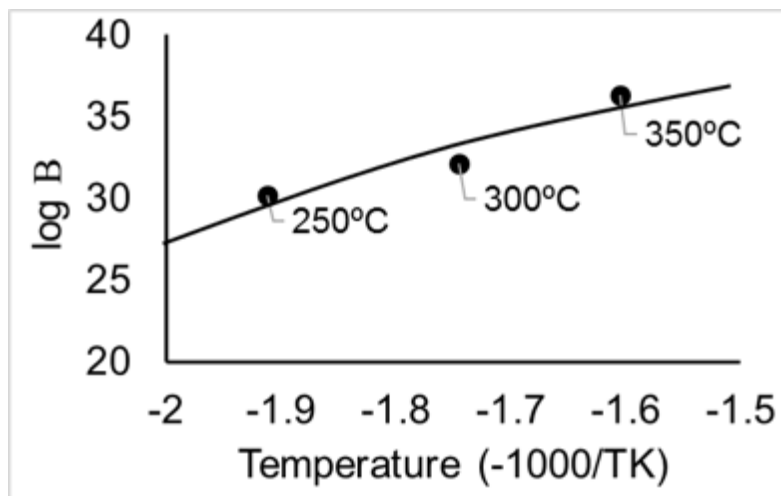
**Figure 3-8. Logarithms of formation constant for U(OH)₂SO₄**
**as function of temperature (−1000/TK).**

In order to extrapolate/interpolate these values to the temperatures beyond those investigated experimentally, the values of formation constants (log $B$) have been fitted to the Ryzhenko–Bryzgalin (MRB) model (Ryzhenko et al. 1985) modified by Shvarov and Bastrakov (1999). The latter is a model that was developed to fit the temperature and pressure dependence of dissociation constants for ion pairs:

$$logK_{(T,P)} = \frac{T_r}{T} logK_{(T_r,P_r)} + B_{(T,P)} * ( Azz_{/a} + \frac{Bzz_{/a}}{T} ) \qquad \text{Equation 3-10}$$

where K is the dissociation constant of the ion pair, $T_r$ and $P_r$ are the reference temperature and pressure, respectively, and *Azz/a* and *Bzz/a* are fitting parameters. The term $B_{(T,P)}$ accounts for the properties of water at a given $T$ and $P$, and is computed from the data of Marshall and Franck (1981). Parameters of the MRB model for U(OH)₂SO₄° are reported in Table 3-3.

**Table 3-3. MRB model parameters for U(OH)₂SO₄ aqueous complex**
**derived based on experimental results in this study**

|  | pK(298) | *Azz/a* | *Bzz/a* |
|---|---|---|---|
| **U(OH)₂SO₄** | 9.774 | −4.876 | 6595.72 |

## 3.4 Discussion

The data listed in Table 3 and illustrated in Figure 3-7 suggest that the stability of U(OH)₂SO₄° decreases drastically with decreasing temperature. Thus, it is not surprising that this aqueous species has not been identified at ambient and near-ambient conditions and is not included in the summarizing dataset reported by Guillamont et al. (2003), which is mostly based on experimental data obtained at T < 100°C. Two

exceptions, though, are the data of Parks and Pohl (1988) and Tremaine et al. (1981), which provide information on the speciation of U(IV) at temperatures up to 300°C. However, these studies focus exclusively on the formation of hydroxyl complexes of U(IV) and, thus, cannot be used for comparison with the results reported here. The dataset of Guillamont et al. (2003) does account for sulfate complexation of U(IV), but suggests that ambient conditions are predominated by simple U(IV)-sulfate complexes, such as $U(SO_4)_2$ and $USO_4^{2+}$. Identification of $U(OH)_2SO_4^{°}$ as the predominant sulfate species at elevated temperatures suggests changes in the speciation scheme and replaces simple sulfate species with mixed hydroxyl-sulfate complexes.

It should be noted that this effect, though relatively uncommon, has been described for a few hard bases, such as Zr, Nb, Ta and Sn (e.g., Aja et al. 1995; Migdisov et al. 2011; Timofeev et al. 2015; Timofeev et al. 2017). For example, speciation of Zr in fluoride-bearing solutions has been shown to be predominated by simple fluoride complexes at near-ambient conditions (Aja et al. 1995), whereas at elevated temperatures it is predominated by hydroxyl-fluoride species (Migdisov et al. 2011). Similar effects were found for Nb and Ta fluoride complexes (Timofeev et al. 2015; Timofeev et al. 2017). In addition, hydroxy-fluoride and hydroxyl-chloride complexes have been described for high-T speciation of Sn(IV) (Ryzhenko et al. 1997). It is notable that most of the species described in the previous studies are neutrally charged, as is $U(OH)_2SO_4^{°}$. This is in good agreement with the general trend for high-T speciation in aqueous solutions: heating tends to result in alteration of the positional and orientational constraints of water molecules, partial disruption of their three dimensional (3D) hydrogen bonding network which stabilizes highly charged species, and, thus, promotion of ion pairing/association and metal complex formation (Seward et al. 2013).

Besides its neutrality, another characteristic feature of $U(OH)_2SO_4^{°}$ is its unexpectedly high stability at elevated temperatures. Tetravalent uranium is traditionally assumed to be immobile under reducing conditions (e.g., Allard, 1982; Sani et al. 2004; Carbol et al. 2005; Opel et al. 2007). This paradigm was recently challenged by Timofeev et al. (2018), who demonstrated that at temperatures above 200°C, uranium can be appreciably mobile at high temperatures, even under reducing conditions, if appropriate ligands (Cl in the case of Timofeev's study) are available for complexation. However, the experiments of Timofeev et al. (2018) were performed at appreciably acidic conditions ($pH_T < 2.5$-3.0). Moreover, they have shown that the ability of chloride-bearing fluid to carry uranium decreases with a power factor of 4 when pH increases. As conditions move toward weakly acidic and near neutral, this ability become insignificant.

Data presented in this study, however, suggest sulfate-bearing solutions, in contrast to chloride-bearing solutions, can develop U concentrations of several ppm when in equilibrium with $UO_2$ at $pH_T$ as high as 5. An example of aqueous species distribution as a function of the activity of sulfate is shown in Figure 3-9 for 300°C and at $pH_T$ of 2 and 5. The calculations were performed for the system saturated with respect to $UO_2$; in order to illustrate competition between chloride and sulfate complexes of U(IV), calculations were performed for solutions containing 1m NaCl. As it can be seen from Figure 3-9(a), and consistently with the findings of Timofeev et al. (2018), acidic conditions combined with elevated temperatures greatly promote the ability of aqueous solutions to carry uranium at reducing conditions. It is evident from this figure that at low concentrations of sulfate, in the field of $UCl_4$ predominance, uranium concentrations predicted for such systems can reach the level of hundreds of ppb, whereas at higher concentrations of sulfate, in the field of predominance of $U(OH)_2SO_4^{o}$ (log $a(HSO_4^-) > -6.4$), concentrations of dissolved U steadily increase, reaching and exceeding ppm levels. Such extreme conditions are, however, relatively rare (primarily due to very high acidity), and Figure 3-9(b) illustrates a more realistic scenario. This diagram models dissolution of uraninite in a solution of the same chemistry, but at pH(T) of 5. As is shown, at this near neutral pH (at 350°C, pH of neutral solutions is 6.145 due to pKw changing with temperature) chloride complexes do not contribute significantly to the mass balance of dissolved uranium. However, the concentrations of U developed due to the contribution of

U(OH)$_2$SO$_4$° are high enough to make this species predominant in aqueous solutions and to develop uranium concentrations exceeding ppm level at log $a$(U(OH)$_2$SO$_4$°) $> -3$. Most notably, for both acidic and near-neutral conditions, it is the U(IV) species that limits the total U solubility.
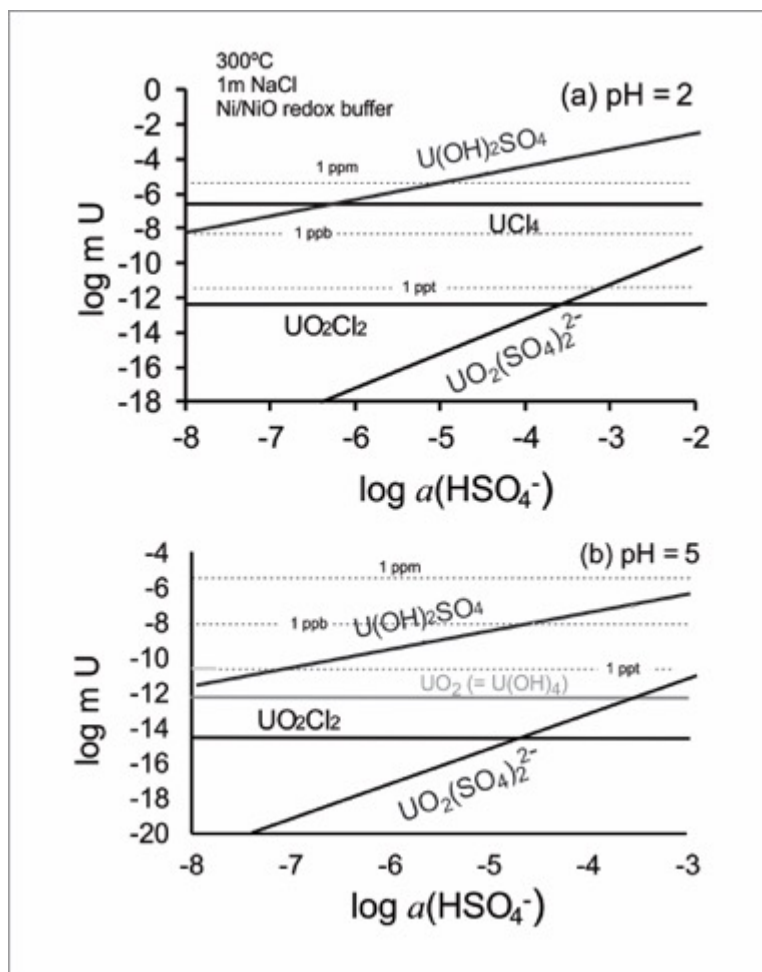


**Figure 3-9. Distribution of predominant species at (a) pH of 2 and (b) pH of 5 at 300°C and conditions corresponding to Ni/NiO buffers**

These findings have important implications for both mobilization of U in natural hydrothermal systems and assessment of potential impacts of breaching engineered barriers in nuclear waste disposal sites. Many natural systems tend to fall in the more neutral pH range, such as Cigar Lake, Canada (Sunder et al. 1996), Jachymov, Czech Republic (Casas et al. 1998), and the Oklo natural reactor (Brookins 1990), all of which are naturally reducing systems and analogous to potential granitic disposal sites. Thus, the scenario of chloride-based transport of reduced U is applicable to only a few specific cases of highly acidic solutions, whereas sulfate-based complexes are likely to be more abundant (upon availability of the ligand in the solution). We foresee that the findings reported in this contribution may lead to re-evaluation of several genetic models proposed for high-T uranium-bearing ore-forming systems.

In the case of nuclear waste disposal sites, a typical solution, which can interact with used fuel in the scenario of an engineered barrier breaching event, is also very different from acidic fluid investigated by Timofeev et al. (2018), and its composition is much closer to the solutions we studied here. As has been shown by a set of studies on high-T interaction of ground water with a variety of clay backfills (250°C to 300°C; Cheshire et al. 2014; Caporuscio et al. 2017; Cheshire et al. 2018), the solution that could potentially penetrate into a canister containing spent fuel or waste form (Engelhard et al. 2016; Guo et al. 2016) can contain up to hundreds of ppm of sulfate (due to high-T decomposition of clay's sulfides), and is at the pH range of 5 to 7. It should be noted that the values of pH reported in the above studies are those determined at 25°C, and it is likely that these values do not correspond to pH(T) developed in solutions at experimental conditions. Thus, evaluating the ability of these fluids to transport U, similar to the diagram illustrated in Figure 3-9(b), we performed thermodynamic calculations assuming near-neutral acidity of the solutions at a pH(T) of 5. Models of uranium species distribution in solutions of the above compositions (in equilibrium with $UO_2$) are illustrated in Figure 3-10. As is shown, the $U(OH)_2SO_4$ species still controls the total uranium solubility. It can also be seen that, in contrast to the models not accounting for sulfate speciation of U(IV) (which predict vanishingly small solubility of U), the contribution of sulfate complexes results in concentrations of dissolved uranium ranging from tens to hundreds of ppb. The highest levels of U solubility were predicted for 300°C. Temperature decrease has a dramatic effect on solubility levels, and at temperatures lower than 200°C to 220°C, the concentrations of dissolved U in such solutions are predicted to decrease below 1 ppt.
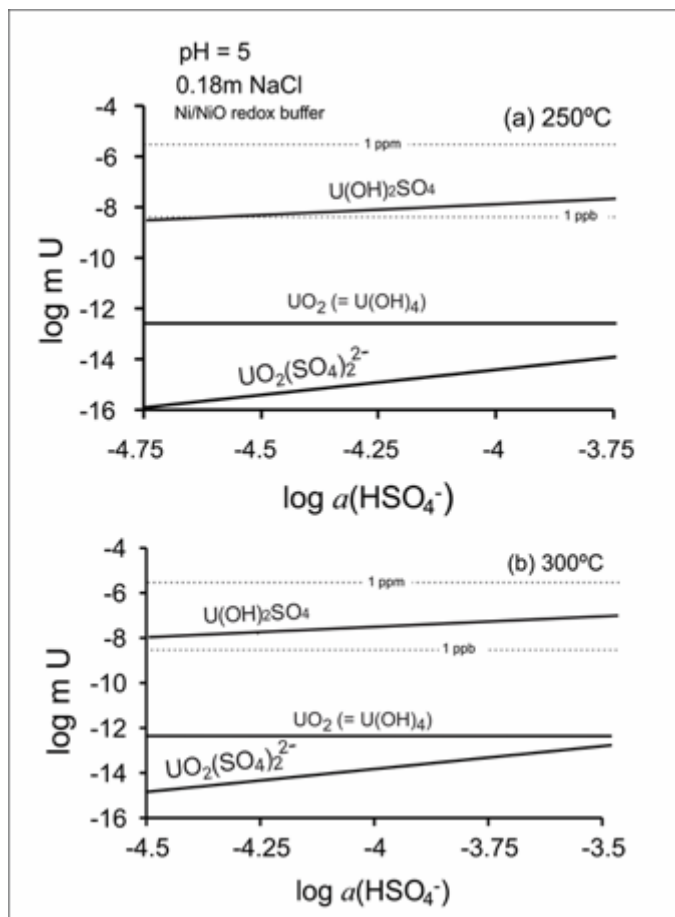
NOTE:    Concentrations are calculated for solutions saturated with respect to solid $UO_2$. Logarithms of uranium molality of each species are plotted against logarithms of hydrosulfate activity over the range of 50 – 300 ppm $Na_2SO_4$.

**Figure 3-10.  Distribution of predominant species at pH of 5 at 250°C and 300°C and conditions similar to nuclear waste disposal sites**

## 3.5    Conclusion

The experimental results obtained in this study indicate the unexpectedly high stability of U(IV)-sulfate aqueous complexes in the temperature range of 250°C to 350°C. The predominant sulfate complex of U(IV) was identified as the neutral aqueous species, $U(OH)_2SO_4^{\circ}$. The previously described chloride complex of U(IV), such as $UCl_4^{\circ}$ (Timofeev et al. 2018), has a stability that has a strong negative correlation with pH and as such plays an important role only in acidic solutions. In contrast, the species identified in this study contributes appreciably to the mass balance of dissolved uranium even in more realistic solutions of near-neutral acidity. It has been demonstrated that, in sulfate-bearing solutions, the $U(OH)_2SO_4^{\circ}$ species controls the solubility of U at reducing conditions. Within realistic ranges of sulfate compositions, uranium concentrations in solutions can develop ranging from hundreds of ppb to hundreds of ppm and even more when in equilibrium with uraninite, a mineral phase commonly encountered in both natural and engineered systems.

## 4.    MODELING OF HIGH TEMPERATURE THMC PROCESSES

## 4.1    Introduction

In the underground EBS, bentonite is typically used as a buffer material to isolate the disposed underground nuclear waste from the surrounding environment. These materials are characterized by high swelling properties, absorption capabilities, and low permeability, as well as a nonlinear response of sorption.  The interaction between the sorption and the environment makes it complex and difficult to predict sorption behavior. To incorporate the effects of new phenomena (at differing chemical and mechanical conditions), numerous experiments are necessary to improve the understanding of sorption performance during different processes underground, and in particular, mechanical constitutive models are required for clays when simulated numerically.

The goal of this section is to develop a coupled THMC model to evaluate mechanical changes induced by the chemical alteration in EBS bentonite and the natural system clay formation under various processes, attempting to provide necessary information for decisions on repository temperature limits.

In a multiyear effort of studying the effect of chemical changes on mechanical under high temperature, we have conducted exploratory simulations for various chemical, hydrological conditions, different types of bentonite and host rocks. We have also developed and tested several constitutive relationships for mechanical-chemical (MC) coupling, which is the key part of THMC model that allows us to evaluate the direct impact of chemical changes on mechanical behavior. In a previous THMC model (e.g., Zheng et al. 2015), the coupling between chemical and mechanical processes was carried out via an Extended Linear Swelling Model (ELSM). However, such model does not accurately describe the transient state of swelling, neglects the history of mechanical change, and is unable to account for the impact of cations exchange on the swelling. Since then, the double structure BExM (Sánchez et al. 2005) has been implemented to link mechanical process with chemistry. As a result, the model can simultaneously incorporate the effects of exchangeable cations, ionic strength of pore water and abundance of swelling clay on the swelling stress of bentonite.

This section contains updates from the milestone report (Zheng et al. 2019) submitted on May 31, 2019. The first part of the section contains the status of the dual structure model, BExM, implemented in the simulator TOUGHREACT-FLAC. It includes an introduction on the MC coupling through BExM. The second part of this section presents results of two modeling scenarios: new temperature simulations at the bentonite-container interface—"high T" and "low T" cases—as a function of the stress path evolution. The third part of the section describes a new simulator, TReactMech. TReactMech is a coupled THMC code, recently developed at LBNL, to simulate coupled THMC processes using surrogate models, which can be incorporated into the Generic Disposal System Analysis (GDSA) model. Preliminary test cases were run with TReactMech on a Linux platform. The first case is a benchmark example to test the code against the analytical solution, and to compare the results with TOUGH-FLAC simulations. The second case describes an ongoing generic modeling of a clay repository with bentonite EBS with peak temperature of 200°C at the canister/bentonite interface.

## 4.2    Double Structure Model

### 4.2.1    Introduction on BExM

In this section, we introduce a dual structure model, BExM. The Barcelona Basic Model (BBM) was developed for simulations of unsaturated soils, considering only the soil macrostructure in a constitutive model. The microstructure is incorporated to extend the BBM to a dual structure model such as BExM to enable simulating the behavior of expansive soils, taking into account the dependency of swelling strains and swelling pressures on the initial stress state and on the stress path, strain accumulation upon suction cycles and secondary swelling. In the dual structure model, the total volume ($V$), the total void ratio ($e$),

and porosity ($\phi$), of the material are divided into two components: microstructural and macrostructural. The microstructure can swell to invade the macroporosity, depending on the mechanical confinement and load level, and thus make permeability changes during soil swelling not proportional to the total strain and deformation of the expansive clay. Equations to describe the mechanical behavior of microstructural and macrostructural levels and the interaction between structural levels are not expressed here for the sake of simplicity.

A one-way coupling approach, in which chemical changes affect mechanical behaviors of bentonite through the evolution of volume fraction of smectite, exchangeable cation concentration, and ionic strength (via osmotic suction), is taken into account through BExM. The mathematical formulations for MC coupling are summarized below.

The original BExM predicts the microstrains induced by the effective stress for the whole microstructure, ignoring the effects of the evolution of volume fraction of smectite. When the material is hydrated, only the smectite in the microstructures interacts with the water invaded and swells. The swelling capacity of the material should be proportional to the volume fraction of smectite $f_s$,. Thus, the elastic microstructural volumetric strains are assumed to depend on the change in the microstructural effective stress as follows:

$$\mathrm{d}\varepsilon_{vm}^e = \frac{f_s}{K_m} \mathrm{d}\hat{p} \qquad\qquad \textit{Equation 4-1}$$

where $\hat{p} = p + s_m$, $\hat{p}$ is the effective mean stress, $p$ is the net mean stress, which is the total mean stress $\bar{\sigma}$ minus gas pressure $p_g$, and $s_m$ is the microstructural suction. The total suction, $s_m$, contains two components, matric suction, $s$, and osmotic suction, $s_o$, i.e., $s_m = s + s_o$. Apparently, there is a relationship between the liquid saturation and the the matric suction, $s$. The effect of ionic strength of the pore water on microstructural strain is computed as:

$$s_o = -10^{-6} \frac{RT}{V_w} \ln a_w \qquad\qquad \textit{Equation 4-2}$$

where $V_w$ is the molar volume of water (in m³/mol), $R$ is the ideal gas constant, $T$ is the temperature (in K), and $a_w$ is the activity of water. $a_w$ is calculated in TOUGHREACT (Xu et al. 2011) as follows:

$$\ln a_w = -\Phi m^* \frac{1}{55.51} \qquad\qquad \textit{Equation 4-3}$$

where $\Phi$ is the osmotic coefficient of the solution, and $m^*$ is the sum of the molarities of all species in the solution.

In Equation 4-4, $K_m$ is calculated as

$$K_m = \frac{e^{\alpha_m \hat{p}}}{\beta_m} \qquad\qquad \textit{Equation 4-4}$$

where $\alpha_m$ is the material parameter. The effect of exchangeable cations is linked to mechanics through the dependence of $\beta_m$ (Equation 4-5) on exchangeable cation concentration as shown in the following equation (Gens 2010):

$$\beta_m = \sum_i \beta_m^i x_i \qquad\qquad \textit{Equation 4-5}$$

Gens (2010) and Guimarães et al. (2013) proposed that $\beta_m^i$ is proportional to the ionic hydrated radius, and inversely proportional to its valence. $\beta_m$ is the sum over ionic species. We calibrated the values of $\beta_m^i$ for different cations against laboratory experiments.

We launched a series of simulations to investigate the swelling capacity of bentonite and to calibrate the parameters of BExM for Full-scale Engineered Barrier EXperiment (FEBEX) bentonite against experiments conducted by Castellanos et al. (2008). Based on simulations of swelling pressure experiments, parameters of BExM are calibrated, and the optimal parameters are listed in Table 4-1. The void ratios of e_micro and e_macro are recalculated based on the experimental data reported by Lloret et al. (2003). The simulation results of the swelling pressure test are displayed in Figure 2-4.

**Table 4-1.  Parameters of BExM for FEBEX bentonite**

| Parameters defining the BBM for macrostructural behavior |
|---|
| $\kappa = 0.030$ $\quad$ $\kappa_s = 0.006$ $\quad$ $\lambda(0) = 0.08$ $\quad$ $p_c = 0.5$ MPa $\quad$ $r = 0.90$ $\quad$ $\zeta = 1$ MPa$^{-1}$ $\quad$ $p_0^* = 6.5$ MPa |
| $\alpha_a = 0.5$ $\quad$ $\alpha_0 = 1 \times 10^{-5}$°C $\quad$ $\beta_m^{Na} = 2.574 \times 10^{-9}$ MPa$^{-1}$ $\quad$ $\beta_m^{K} = 0.257 \times 10^{-9}$ MPa$^{-1}$ |
| $\beta_m^{Mg} = 3.346 \times 10^{-9}$ MPa$^{-1}$ $\quad$ $\beta_m^{Ca} = 2.574 \times 10^{-9}$ MPa$^{-1}$ |
| **Parameters defining the law for microstructural behavior** |
| $\alpha_m = 2.1 \times 10^{-2}$ MPa$^{-1}$ $\quad\quad$ $\chi = 1$ |
| **Interaction functions** |
| $f_{ic} = 1 + 0.9 \tanh\left[20\left(\frac{p_r}{p_0} - 0.25\right)\right]$ $\qquad\qquad$ $f_{is} = 0.8 - 1.1 \tanh\left[20\left(\frac{p_r}{p_0} - 0.25\right)\right]$ |
| **Initial conditions** |
| $e_{macro} = 0.21$ $\quad$ $e_{micro} = 0.48$ $\quad$ $f_s = 0.5428$ $\quad$ $s_o = 0.777$ MPa |

NOTE:    BBM = Barcelona Basic Model
             BExM = Barcelona Expansive Model
             FEBEX = Full-scale Engineered Barrier EXperiment

## 4.3   Generic Model Development

The model used in this report is similar to that given in previous publications (Liu et al. 2013; Zheng et al. 2014; Zheng et al. 2015; Zheng et al. 2016; Zheng et al. 2017a). We briefly describe below each element of the THMC model, focusing on the updates since June 2019 after the submission of Zheng et al. (2019).

### 4.3.1    Simulator

Zheng et al. (2016) reviewed an application of several THMC simulators, and concluded it is difficult to apply these simulators to real problems. The numerical simulations in this study are conducted with TOUGHREACT-FLAC3D, which sequentially couples the multiphase fluid flow and reactive transport simulators, TOUGHREACT (Xu et al. 2011) and the finite-difference geomechanical code FLAC3D (Itasca 2009). The coupling of TOUGHREACT and FLAC3D was initially developed in the work by Zheng et al. (2012) to provide the necessary numerical framework for modeling fully coupled THMC processes. Recently, the model was upgraded using multiple constitutive models, such as the dual structural BExM and ELSM, which will be discussed in more detail below.

### 4.3.2    Modeling Scenarios

The model is applied to a hypothetical bentonite-backfilled nuclear waste repository, comprising a horizontal nuclear waste emplacement tunnel at a 500-m depth in Opalinus clay (Figure 4-1). The case is a pseudo two dimensional (2D) model with Y-axis aligned parallel to the tunnel, with 1-m thickness along the *y*-axis. The *z*-axis is vertical, while the horizontal *x*-axis is perpendicular to the tunnel. While the canister is modeled as a heat source with mechanical properties of steel, the THC changes in the canister and its interactions with EBS bentonite are not considered for the sake of simplicity.

An initial stress field is imposed by the self-weight of the rock mass. Zero normal displacements are prescribed on the lateral boundaries of the model. Zero stress is applied to the top, and vertical displacements are zero at the bottom of the model domain. An open boundary condition is applied to assign the liquid pressure at top and bottom, and initially the model domain is in a hydrostatic state. The initial temperature at the top is 11°C and 38°C at the bottom, with a thermal gradient of 27°C/km. The nonisothermal model simulations were conducted with a time-dependent heat power input. The power curve in Figure 4-1 was adopted from representative heating data obtained from the U.S. DOE's Used Fuel Disposition Campaign for PWR used fuel. This heat load is then scaled in the 2D model to represent an equivalent line load, which depends on the assumed spacing between individual waste packages along an emplacement tunnel. The heat load for the "low T" case corresponds to an initial thermal power of 3144 W (total power, equal to about 220 W/m along the length of the heater) for a 4-PWR-element waste package after aging for 60 years, a 50-m spacing between emplacement tunnels, and 3-m spacing between the 5-m long packages. The input power is estimated to increase the temperature to 100°C at peak inside bentonite buffer. The heat load for the "high T" case represents similar waste package and spacing, except with only 20 years of aging, and will induce 200°C at peak in the buffer. Initially the EBS bentonite has a water saturation of 65% and the clay formation is fully saturated. From time zero, the EBS bentonite undergoes simultaneously re-saturation, heating, chemical alteration, and stress changes.
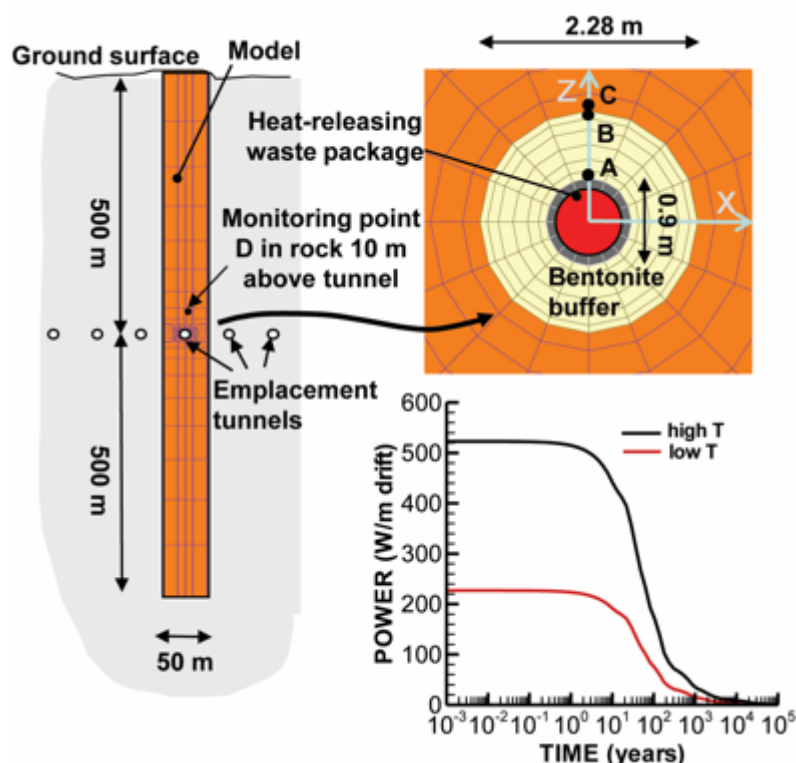
NOTE:   Modeling monitoring points: A—inside the bentonite near the canister, B—inside the bentonite and near the EBS-natural system interface, C—inside the clay rock formation and near the EBS-natural system interface, D—inside the clay rock formation at a distance of 10 m from the canister. Power curves in simulations: "high T" is for the 200°C peak temperature in the buffer); and "low T" is for the 100°C peak temperature in the buffer.

Source: Rutqvist et al. 2014.

**Figure 4-1.  Modeling domain for test example of a bentonite, back-filled, horizontal emplacement drift at a depth of 500 m**

## 4.4    Modeling Results

To study bentonite alteration using a coupled THMC model, the simulator was upgraded, more constitutive relationships were tested, and more scenarios were analyzed. While the previous work focused only on the mechanical behavior, we now employed the dual structure model BExM for the same scenarios under the same geological formation. As described in Section 4.2.1, the MC coupling method through the dual-structure model takes account for the effects of the volume fraction of smectite, exchangeable cations and ionic strength on swelling capacity. Two scenarios of generic repository cases as described in Section 4.3.2 were simulated with each model to illustrate the swelling behavior of the bentonite. We first present high temperature ("high T") cases in this section. The coupling is approximated as one-way, i.e., the mechanical behavior does not affect the fluid, thermal transports or chemical reactions. Thus, it neglects poro-elastic changes in host rock pore space. The evolution of temperature, liquid saturation and pore pressure is the same for all cases, which helps distinguish the effect on stress by different models.

### 4.4.1    Results of the High Temperature Case

Figure 4-2 presents the stress paths in the 3D $q$-$p$-$s_m$ space and the corresponding projection on the $p$-$s_m$ plane. We present the stress paths at Points A and B with BExM to show the evolution of both macro- and micro-structures. Figure 4-3(a) and (b) display the 2D stress paths together with the evolution of $p_0$ in terms of suction. Figure 4-3(c) and (d) present the changes of void ratio (macro, micro, and total) in terms of suction. Figure 4-3(e) and (f) depict the evolution of the values of the interaction functions movement in the various stages of the analysis.

At Point A, which is close to the heater, at the beginning of the test, since the temperature is not high, the bentonite undergoes the wetting process, and it swells initially, so that the interaction function $f_{is}$ is triggered as shown in Figure 4-3(e). When temperature increases rapidly to over 100°C, the bentonite is drying. Simulations show that the suction increases and the liquid saturation decreases, activating MC mechanism at microscale. The interaction function $f_{ic}$ is positive and induces small compressive plastic macrostructural deformation. Moreover, the bentonite at Point A undergoes confinement accumulation from the external zones of the buffer and host rocks, so the macrostructure also contracts due to the increase of the mean net stress. Both processes compact the macrostructure, resulting in growth of $p_0$, and reduction of the total void ratio. After about 1 year, the bentonite at Point A undergoes hydration again: the liquid saturation grows and suction reduces, resulting in swelling of the bentonite and activating the interaction function $f_{is}$. The function $f_{is}$ is positive and induces tensile plastic macrostructural strain, but then it becomes negative, and, consequently, induces the compressive plastic strain. The mean net stress still increases during this stage, resulting in the macrostructure contraction. However, later in this stage, the temperature is close to 180°C, inducing a significant thermal expansion at macroscale and causing a macrovoid ratio increase. The total void ratio increases during this phase, while $p_0$ follows a complicated increase/decrease path until it becomes steady when the material is fully saturated. Postsaturation, all state variables at Point A remain practically unchanged, expect the interaction function changes between $f_{ic}$ and $f_{is}$ paths. The final loading-collapse (LC) curve on Figure 4-3(a) is to the right of the initial one, indicating the increment of the elastic domain, and the hardening of the material.

A different behavior is taken place at Point B that is close to the host rock and is affected by the hydration boundary (Figure 4-3(b), (d), and (f)). Bentonite at Point B is initially under compression due to the high confinement from the host rock. The simulations show a slight contraction at macroscale and the total and macrovoid ratio decrease. The microstructure is also under compression, which is implied by the interaction function, which follows $f_{ic}$ path triggered by the MC mechanism. Then, the bentonite at point B undergoes the hydration process, with the increase in the liquid saturation and a decrease in suction, resulting in bentonite swelling and activation of the MC mechanism. The evolution of $f_{is}$ at point B is similar to that at Point A during the wetting phase. Firstly, $f_{is}$ is positive, indicating the tensile plastic macrostructural strain, then it becomes negative, indicating the compressive plastic strain. Later, thermal expansion at macroscale also occurs, when the bentonite reaches full saturation, causing a slight increase in the macrovoid ratio. The total void ratio increases during this phase, mainly due to the contribution of microstructural swelling. During this phase, also some suction increases happens, so the interaction function changes to the MC mechanism with $f_{ic} > 0$ for a short period, then it goes back to the MS path. This implies a large microstructural swelling due to the strong reduction of microstructural effective stress. After the saturation, macrostructure contracts again, mainly, due to accumulation of effective stress at macroscale, when liquid pressure dissipates, resulting in the reduction of the macro and total void ratio. The final LC curve moves left slightly, which is due to the reduction of the elastic domain, and softening of the material.
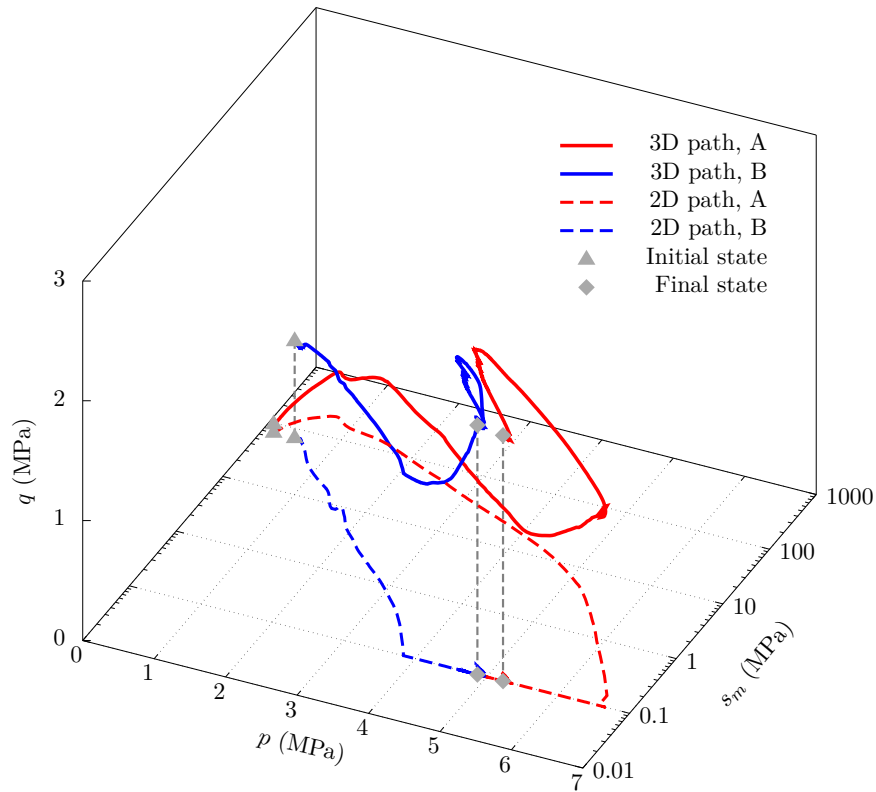
**Figure 4-2. Stress paths at Points A and B in 3D $q$-$p$-$s_m$ space for the "high T" case**
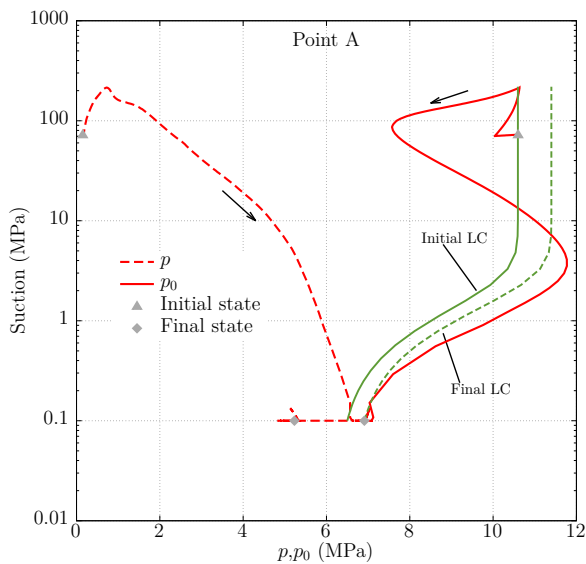


(a) Stress path of Point A on $p$-$s_m$ plane
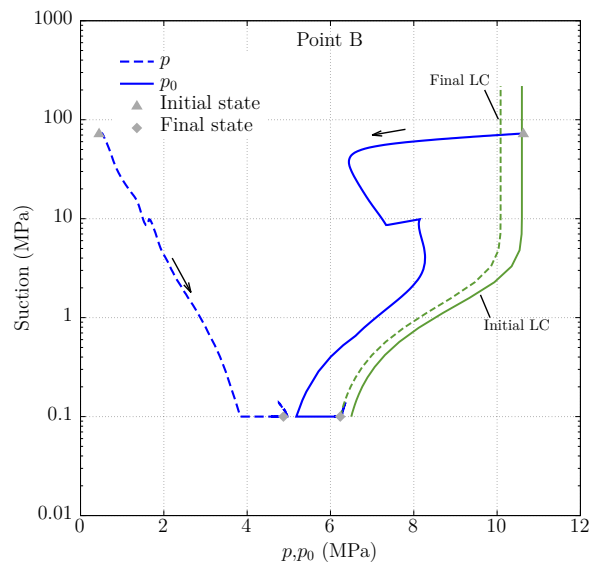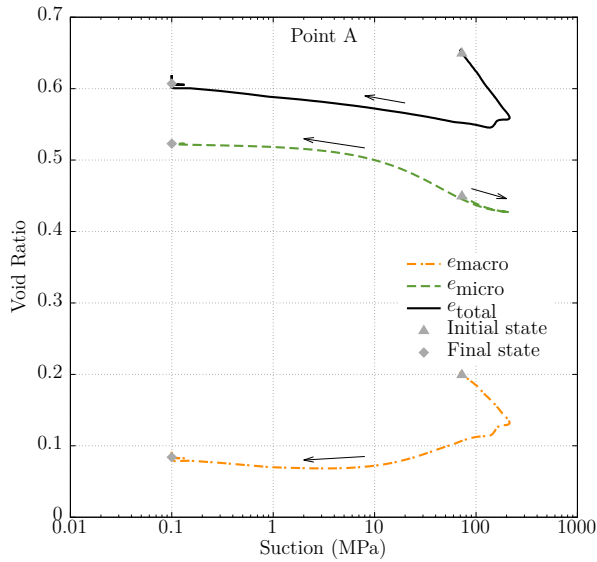
(b) Stress path of Point B on $p$-$s_m$ plane

(c) Void ratio evolution at Point A
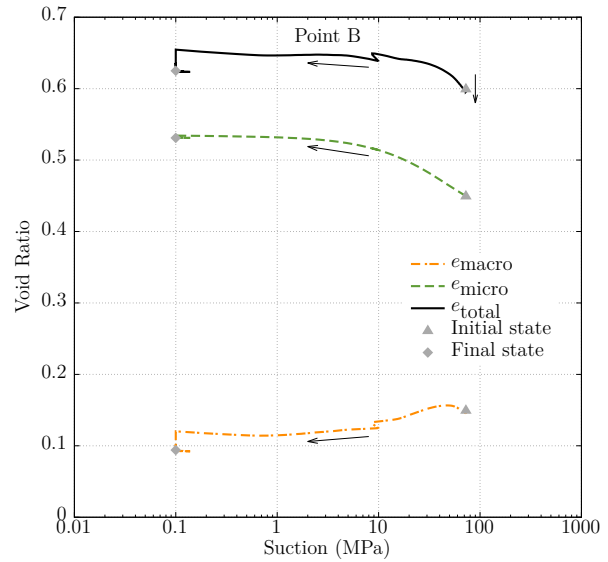
(d) Void ratio evolution at Point B
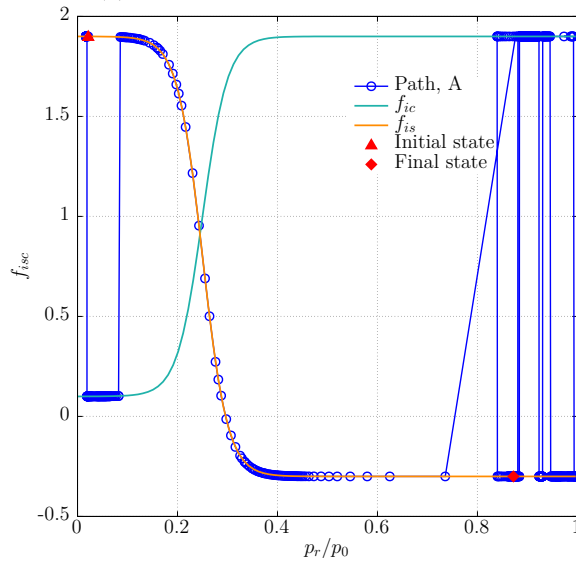
(e) Interaction function at Point A
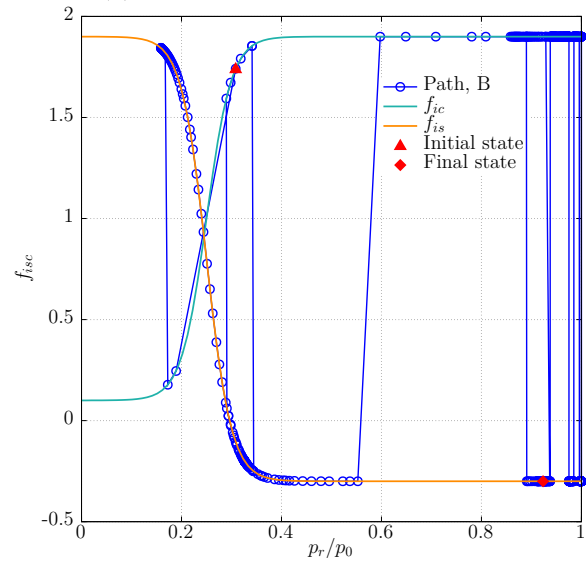
(f) Interaction function at Point B

NOTE:    In (a) and (b), LC = loading-collapse.

**Figure 4-3.  Simulation results of bentonite behavior at Points A and B
with FEBEX bentonite for the high T case**

## 4.4.2    Results of the Low Temperature Case

In the "low T" case, since the temperature is below 100°C in the buffer, the desaturation process is suppressed. Figure 4-4 presents the stress paths in the 3D $q$-$p$-$s_m$ space and the corresponding projection on the $p$-$s_m$ plane, showing similar saturation paths at both Points A and B on the $p$-$s_m$ plane. Figure 4-5(a) and (b) display the stress paths together with the evolution of $p_0$ with suction changes ($p_0$ is an apparent pre-consolidation stress for the current value of suction). Figure 4-5(c) and (d) present the

relationship between the void ratio (macro, micro and total) and the suction. Figure 4-5(e) and (f) illustrate the evolution of the values of the interaction function as a function of $p_r/p_o$.

The stress path on $p$-$s_m$ plane for the "low T" case is different from that simulated for the "high T" case. Since Points A and B in "low T" case are characterized by similar saturation processes, they both exhibit similar behavior in "high T" case. However, for "low T" case, the different location of the final LC curve implies that the shrinkage of the elastic domain.
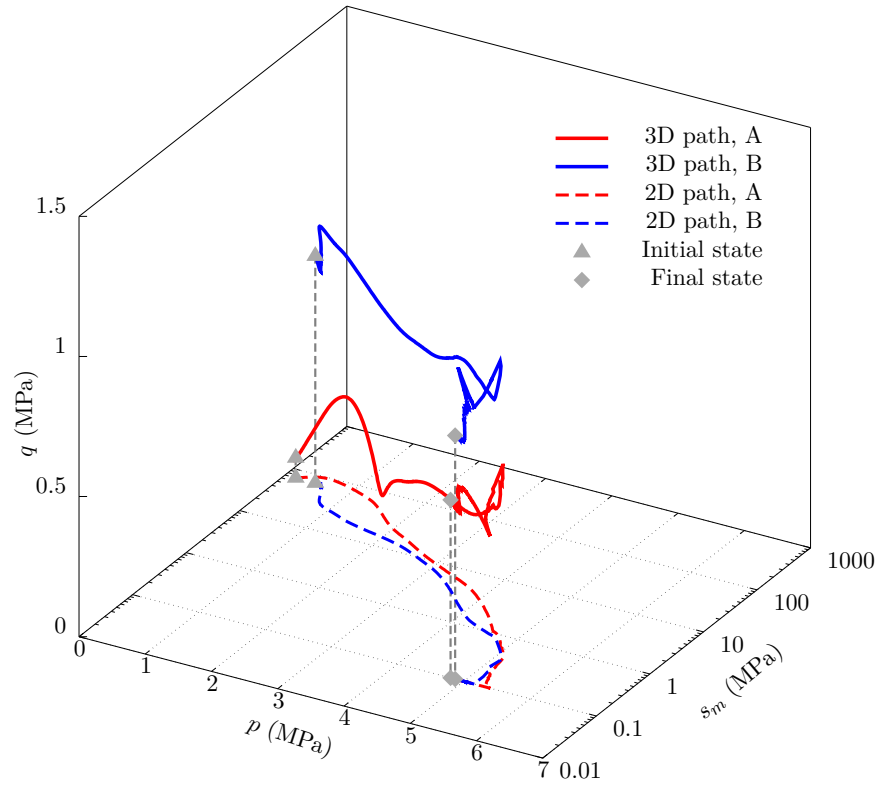


**Figure 4-4. Stress paths at Points A and B in 3D $q$-$p$-$s_m$ space for the "low T" case**
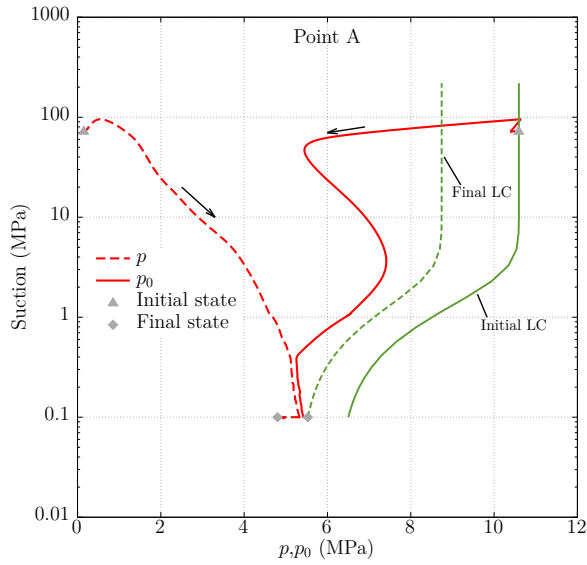
(a) Stress path of Point A on $p$-$s_m$ plane
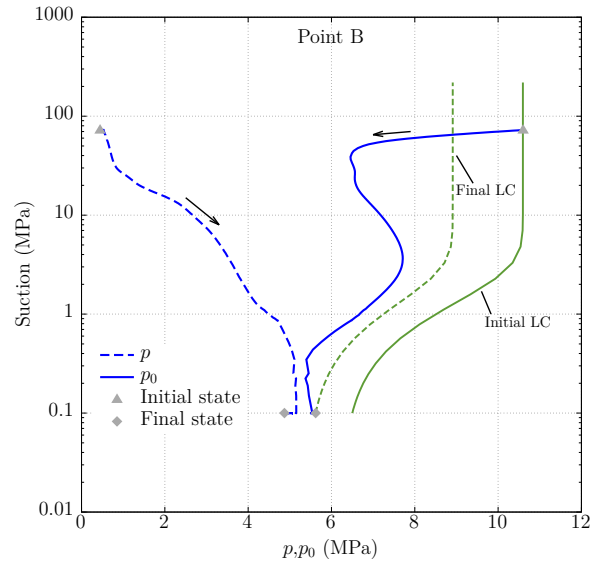


(b) Stress path of Point B on $p$-$s_m$ plane



(c) Void ratio evolution at Point A



(d) Void ratio evolution at Point B
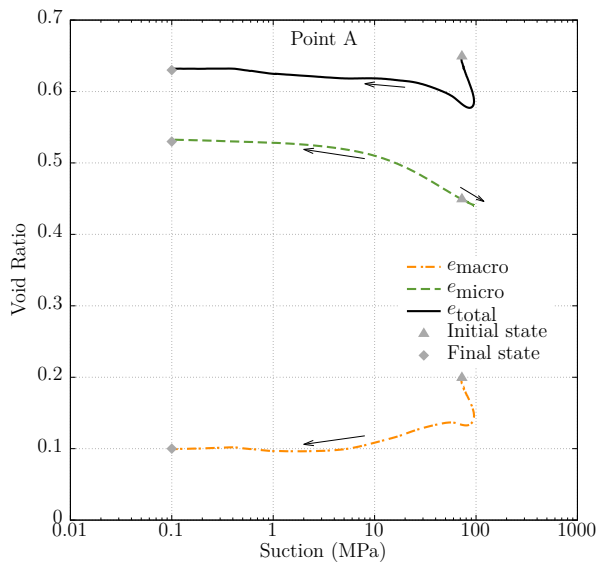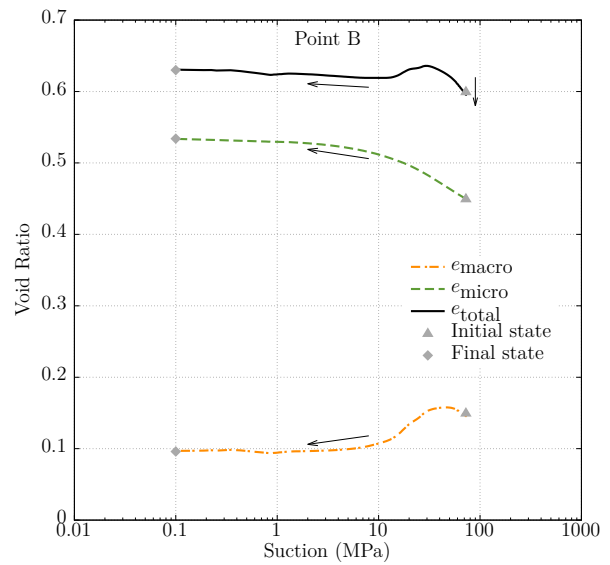
(e) Interaction function at Point A                 (f) Interaction function at Point B
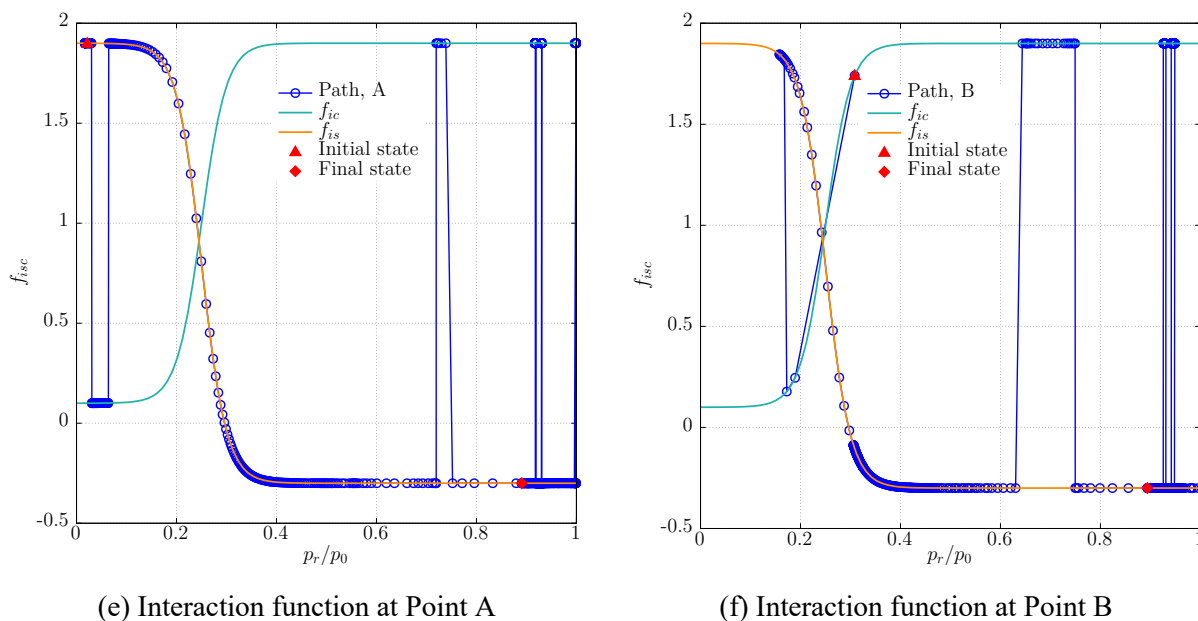
**Figure 4-5.  Simulation results of bentonite behavior at Points A and B
with FEBEX bentonite for the "low T" case**

It is not clear how to interpret the pattern of the swelling stress from the results of simulations using the dual-structure model, because the microswelling strain is calculated directly in the framework of the model. Moreover, because of the non-linear behavior of the elasto-plasticity in both macro- and micro-structures, it is difficult to distinguish the swelling stress from the total stress. Therefore, in Figure 4-6, we present the mean net stress for unsaturated bentonite and the mean effective stress for fully saturated bentonite during the simulation to illustrate the accumulation of stress in the solid skeleton of bentonite. At Point A, the mean effective/net stress for the "high T" case is about 6.7 MPa at peak, which is higher than the peak stress of 5.3 MPa for the "low T" case. This difference can be explained by the effect of a more significant drying of bentonite in "high T" case. Figure 4-6 illustrates that after reaching the peak points, stresses in both cases are reduced as the effective stresses are plotted instead of net stresses when bentonite changes from unsaturated condition to fully saturated. After 100 years, pore pressure drops after its peak value, and the effective stress starts to increase for the "high T" case, which can be explain by the chemical effect and declining of the osmotic suction. Later, the effective stress in the "high T" case increases higher than that in the "low T" case due to combined effects of the swelling capacity increase and the large pore pressure reduction. Also, no volumetric collapse occurs since the material state does not reach the LC curve. The key variables affecting the LC curve is the net mean yield stress at full saturation, $p_0^*$, and macrostructural stiffness parameters, $\lambda(s_m)$ and $\kappa$, which are obtained in laboratory experiments, but quite dependent on the compaction status of samples. At Point B, both "high T" and "low T" cases exhibit similar stress evolutions, but the stress in "high T" case is 0.4 MPa lower than that for the other case due to the fast saturation process and strong confinement induced by the higher thermal stress in the "high T" case. However, later, around 40,000 years, the stress recovers to the same level as for the "low T" case.
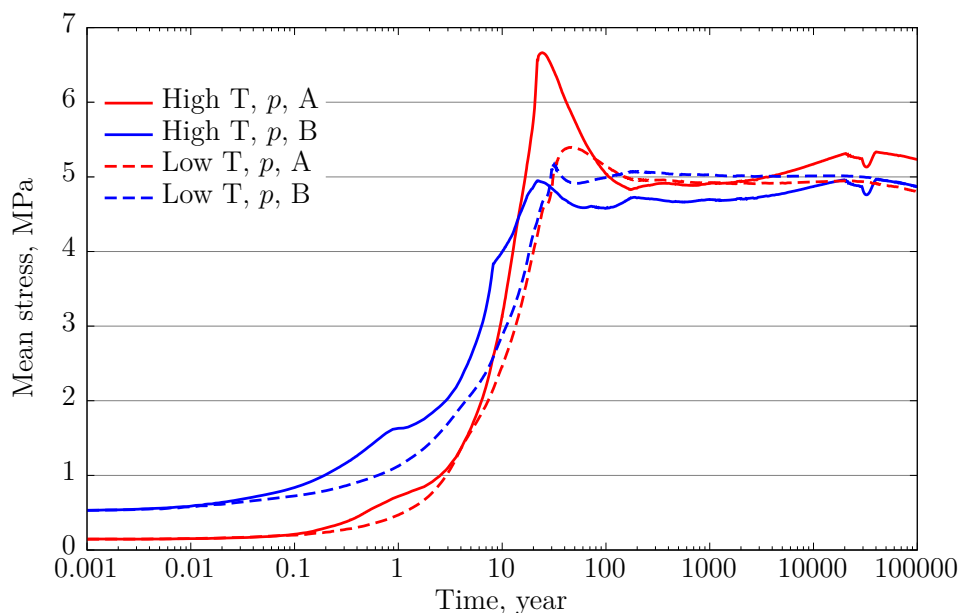
**Figure 4-6. Simulation results of stress at Points A and B with FEBEX bentonite for the "low T" and "high T" cases**

## 4.5 New TReactMech Simulator and Linux Platform

### 4.5.1 Introduction on TReactMech

In FY19, as a part of an effort for integrating the coupled THMC model into the GDSA framework, we started to transition numerical simulations the Linux platform using a new numerical simulator TReactMech, recently developed at LBNL. TReactMech introduces a parallel coupled continuum geomechanics capability into the thermal-hydrological-mechanical-chemical-biogeo (THMCB) parallel simulator TOUGHREACT V3.X-OMP (Sonnenthal and Spycher 2014; Xu et al. 2011; 2006), with improvements to the TOUGH2 multiphase flow core (Pruess et al. 1999). The geomechanical formulation is based on a 3D continuum finite-element model with full 3D stress calculations, plastic deformation via shear and tensile failure (Kim et al. 2012; 2015; Smith et al. 2015).

TReactMech is ideally suited for a continuum representation of fractured and porous rock masses at scales of meters to tens of kilometers. However, TReactMech can also simulate processes at the scale of individual fractures, such as for simulating hydraulic fracturing, or single-fracture deformation at the core-scale. The continuum model approach considers local (grid-block scale) averaging of fracture porosities, permeabilities, and other properties, in comparison with discrete fracture models that capture fracture aperture changes typically using statistical realizations of fracture size distributions and orientations. Applications of TReactMech to Enhanced Geothermal System stimulation modeling and THMC experiments on rock cores are presented in publications by Sonnenthal et al. (2015, 2018) and Kneafsey et al. (2017).

In TReactMech, heat and fluid flow, stress, and reactive transport equations are solved using the sequential non-iterative approach, as shown schematically in Figure 4-7. A system of fluid flow and heat transport equations are solved simultaneously as in TOUGH2 (Pruess et al. 1999) with modifications to consider multiple coupled geochemical and geomechanical effects on porosity and permeability, as well as taking into account new capabilities, such as temperature-dependent thermal properties. TReactMech

uses a hybrid parallel computation approach, in which the geomechanics are solved using Petsc/MPI and the reactive chemistry with OpenMP. Geomechanics (3D stress equations, strain and failure strain) simulations are performed after fluid and heat flow, followed by simulations of transport of aqueous and gaseous species, mineral-water-gas reactions, and finally permeability-porosity-capillary pressure changes owing to geomechanical and geochemical changes to porosity or fracture aperture.



Source: Sonnenthal et al. 2018.
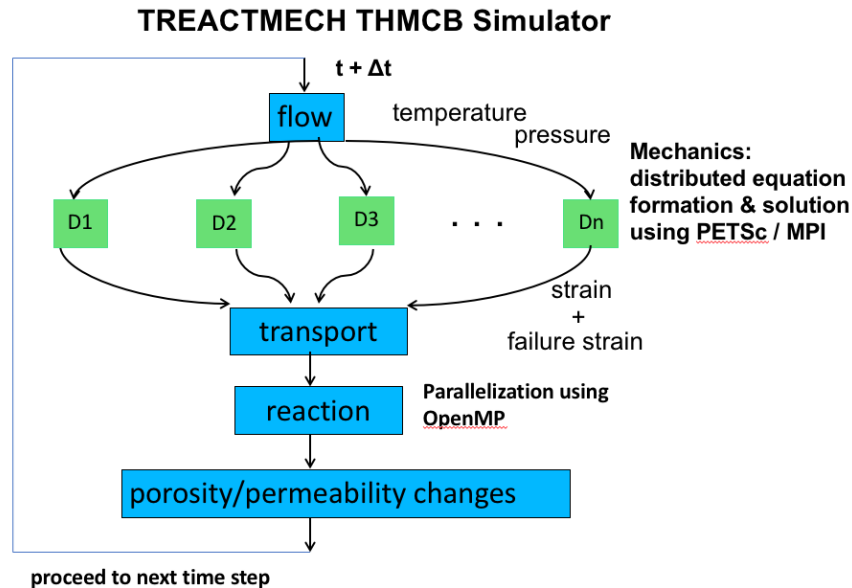
**Figure 4-7.  TReactMech flowchart**

## 4.5.2    3D THM Modeling Benchmark

The goal of this section of the report is to present the results of TReactMech modeling of a basic benchmark 3D test case, considering thermal-hydrologic-mechanical (THM) processes to validate the code implementation against the analytical solution. The case study includes simulations of the consolidation of an infinite homogeneous saturated porous medium around a constant point of the heat input power. The analytical solution for this problem was provided by Booker and Savvidou (1985) and Smith and Booker (1993), considering that the pore water and the solid skeleton of clays are incompressible. The 3D model domain is a cube of $15 \times 15 \times 15$ m. Considering symmetry planes at $x = 0$, $y = 0$, and $z = 0$, only an eighth of the model is simulated. The domain near the heat source is refined with a smaller mesh for better accuracy. The heat source is a cube with 2.5-cm radius (Figure 4-8(a)). In order to simulate the THM problem, we also modified the simulator to match all theoretical assumptions used in the derivation of the Booker and Savvidou (1985) analytical solution.

The initial temperature and pore pressure are set to 0°C and 0 Pa, respectively. Regarding thermal and hydraulic conditions and considering symmetry conditions, the three symmetry planes are impermeable and adiabatic. At far field, the temperature and pore pressure are set to 0°C and 0 Pa, respectively. At the heat source, a constant heat power of Q=150 W is instantaneously applied at $t = 0$. Regarding mechanical conditions, all model domain boundaries are free except the symmetry planes, where null displacement conditions are applied normal to the boundaries. A homogenous and isotropic material is considered. The

model parameters in the benchmark test are listed in Table 4-2. The modeling outputs are temperature, pressure, stresses and displacements up to 365 days at the monitoring points, as listed in Table 4-3.

**Table 4-2. Model parameters of the benchmark example**

| Parameters | Values |
|---|---|
| Porosity | $\phi = 0.15$ |
| Equivalent thermal conductivity [W/(m·K)] | $\lambda = 1.7$ |
| Equivalent density [kg/m³] | $\rho = 2445$ |
| Equivalent heat capacity [J/(kg·K)] | $C_p = 1000$ |
| Permeability [m²] | $k = 4.5 \times 10^{-20}$ |
| Young modulus [MPa] | $E = 4500$ |
| Poisson's ratio | $\nu = 0.3$ |
| Density of solid grains [kg/m³] | $\rho_s = 2700$ |
| Heat capacity of solid grains [J/(kg·K)] | $C_{ps} = 773$ |
| Volumetric coefficient of thermal expansion of solid grains [1/K] | $\alpha_s = 4.2 \times 10^{-5}$ |
| Density of water [kg/m³] | $\rho_w = 1000$ |
| Compressibility of water [1/Pa] | $c_w = 5 \times 10^{-10}$ [a] |
| Heat capacity of water [J/(kg·K)] | $C_{pw} = 4180$ |
| Dynamic viscosity of water [Pa×s] | $\mu_w = 1 \times 10^{-3}$ |
| Volumetric coefficient of thermal expansion of water [1/K] | $\alpha_w = 4 \times 10^{-4}$ |

NOTE:    [a] The analytical solution in Booker and Savvidou (1985) assumes the water is incompressible, indicating $c_w \approx 0$.
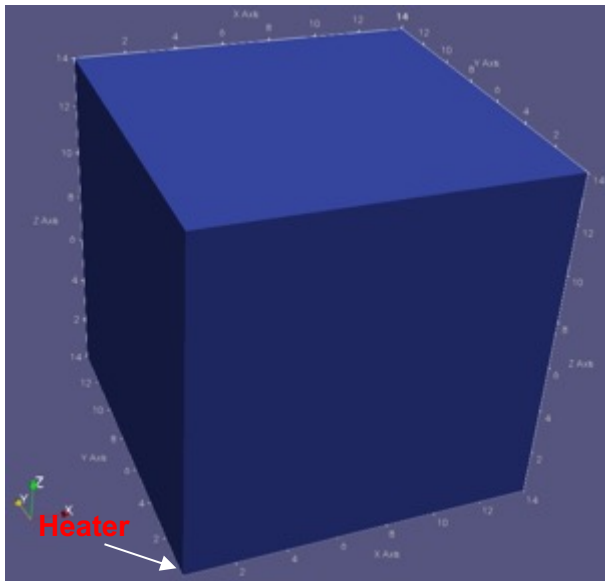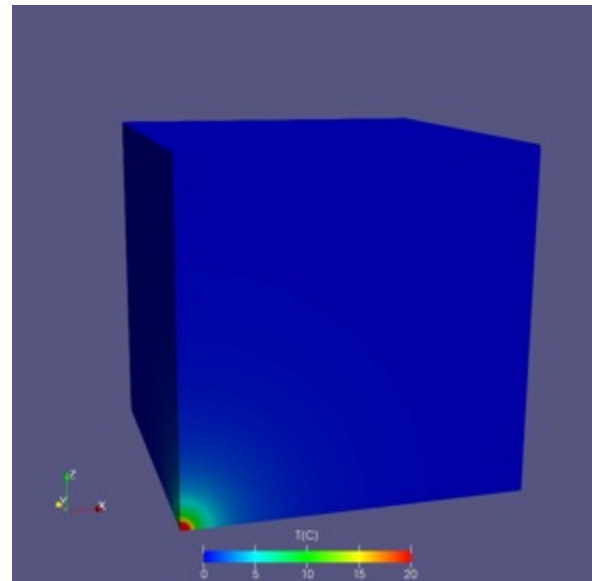


(a)                                                                     (b)

**Figure 4-8.  (a) Modeling domain of the benchmark modeling test, and (b) result of simulations of the temperature distribution in the modeling domain after 1 year**

**Table 4-3.  Points for numerical results for 3D THM benchmark**

| Points | $(x, y, z)$ Coordinates | Quantity |
|--------|-------------------------|----------|
| P1 | (0.35, 0, 0) | Temperature, pressure |
| P2 | (1.375, 0, 0) | Temperature, pressure |
| P3 | (0.35, 0.45, 0.625) | Temperature, pressure, stress |

Simulation and analytical results of temperature at points P1, P2, and P3 are plotted in Figure 4-9. The calculated temperature at point P1 is slightly higher than the analytical solution in Figure 4-9(a), which is likely due to the size effect of the heat source. Except this difference at point P1, an overall good prediction of temperature between numerical and analytical solutions is obtained. Also, a good agreement on pore pressure is achieved (Figure 4-9(b)). The peak of the pore pressure from the modeling at the point P1 is higher by 0.1 MPa of the analytical solution, which is consistent with the higher temperature simulated at P1.

As temperature increases, the pore pressure at all points grows, reaching the peak pressure, and then it dissipates to the zero during a long period. Figure 4-9(c) displays the normal stress evolution at point P3, showing that the numerical results match the analytical solution well, except the peak value for each stress is slightly lower, and later the stress reduces more than the analytical solutions, which could be caused by the boundary effects. The numerical results of shear stress evolution at P3 match the analytical solution as well.



(a)                                                                    (b)

(c)



(d)
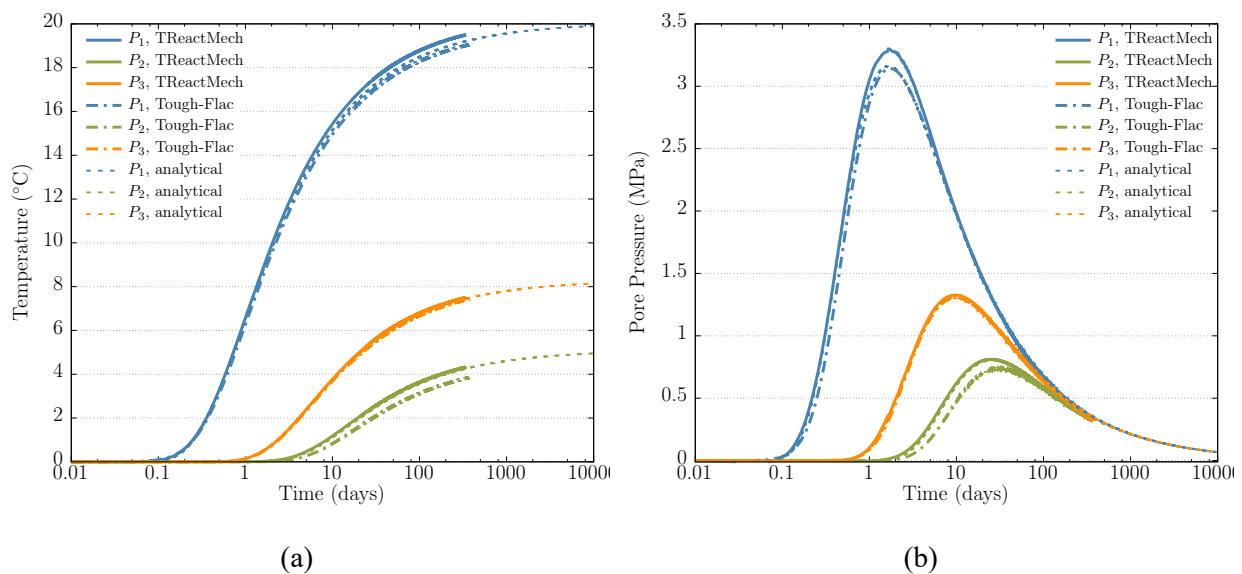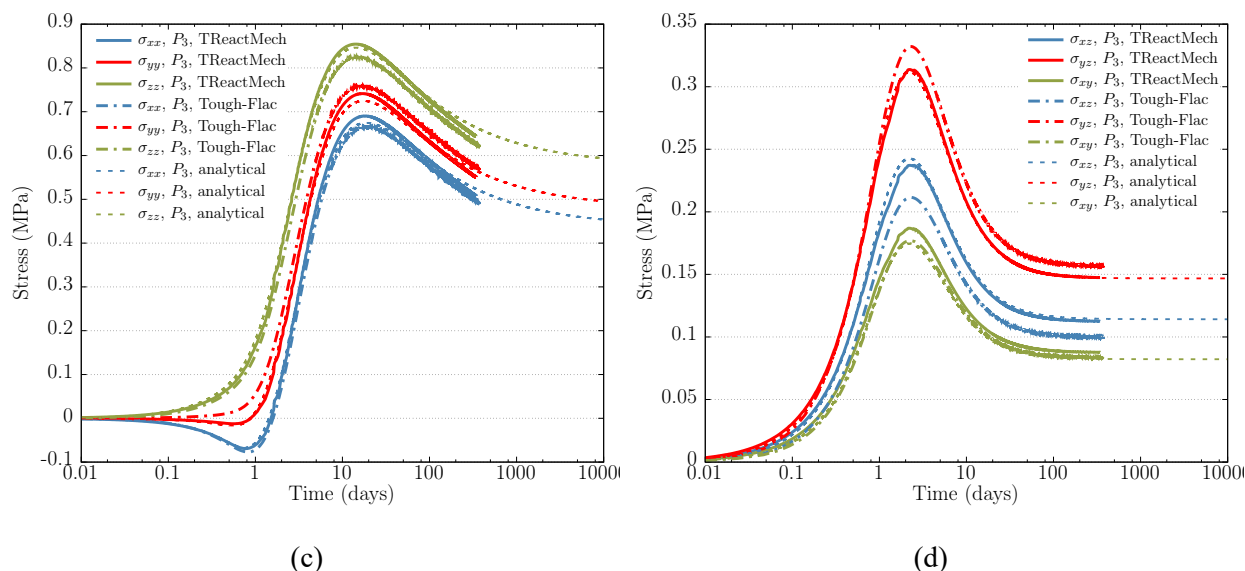
NOTE:    P1 is at (0.35, 0, 0), P2 is at (1.375, 0, 0), and P3 is at (0.35, 0.45, 0.625).

**Figure 4-9.  Simulation results of 3D THM modeling: (a) temperature evolution
at P1, P2, and P3; (b) pore pressure evolution at P1, P2, and P3;
(c) normal stress changes at P3; and (d) shear stress changes at P3**

In general, a good agreement between numerical simulations and analytical solutions is obtained, which verifies the correctness of the THM models' computation using the new simulator. Figure 4-9 also shows that the results of TReactMech simulations match well with the TOUGH-FLAC simulations of the same benchmark case.

### 4.5.3    THMC Modeling of Bentonite in the Nuclear Waste Disposal

After the benchmark test, TReactMech was used to simulate the generic case described in Section 4.3.2. We generated a similar model following the same geological formation, and used the same EBS material—steel cell at the center surrounded by FEBEX bentonite and Opalinus clay shown in Figure 4-10. In the first attempt at simulating the generic case, TReactMech did not converge. Recently the simulation domain was reduced to 20 × 20 m with uniform 0.1 × 0.1 m elements, attempting to overcome the convergence issue. Only half of the domain is simulated to reduce the number of elements. During the heating period, the unsaturated bentonite is placed in the tunnel, and the surrounding clay is assumed as fully saturated. Since the domain is much smaller than the initial simulation, it is difficult represent the pore pressure and stress conditions. More work to improve the simulation is undergoing.
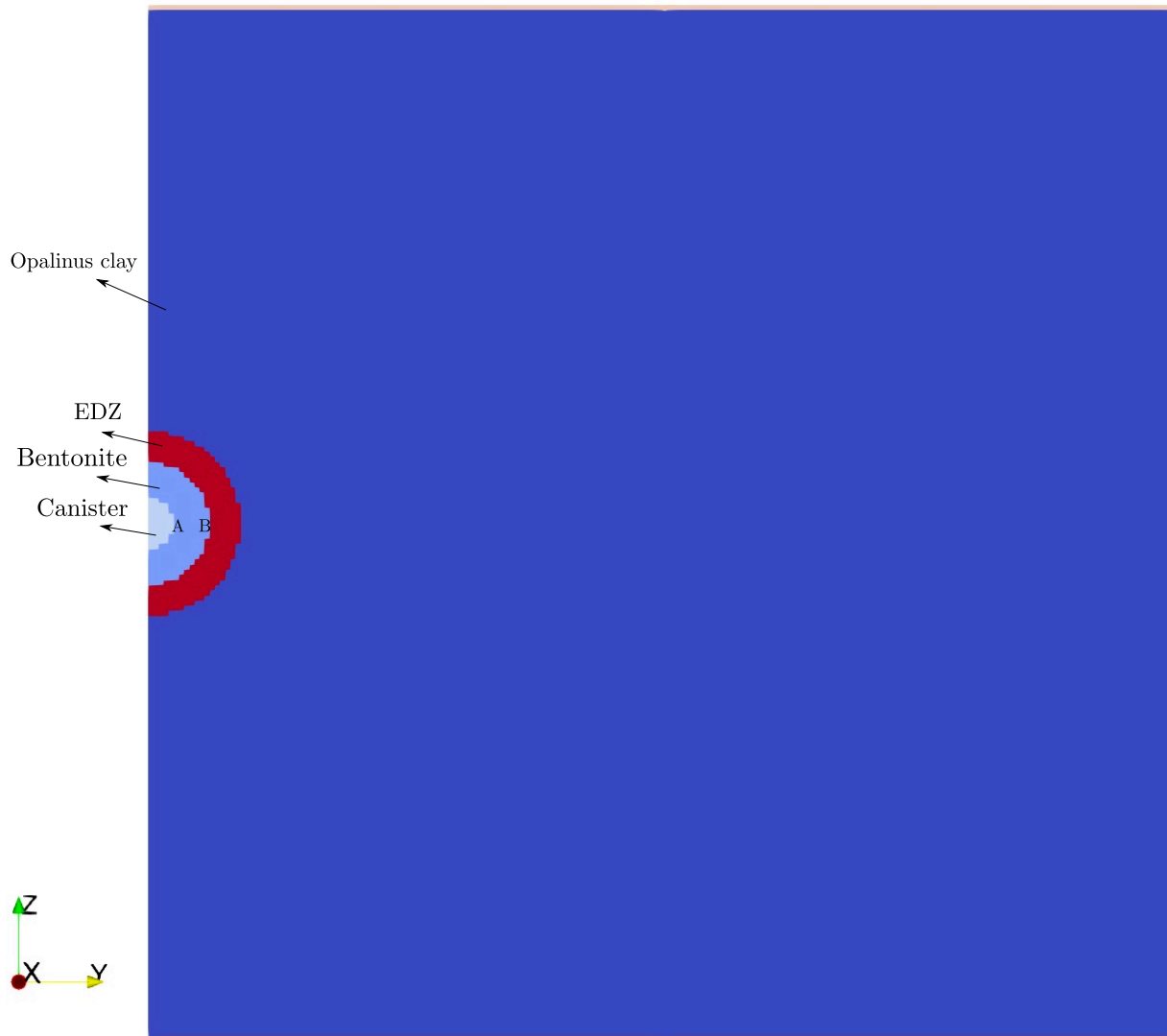
**Figure 4-10.  Modeling domain**

We simulated the excavation process to obtain the initial flow status before the bentonite is refilled in the tunnel. Due to the implicit modeling of the excavation in TReactMech, the grid is presented in the simulation domain as shown in Figure 4-10. The method to simulate the excavation process is by reducing the stiffness and density of the material inside the tunnel. Based on it, we can obtain the initial hydraulic status before the heating starts.

Figure 4-11 through Figure 4-14 demonstrate the results of simulations of temperature, pore pressure, stress, and liquid saturation at Points A and B in "high T" case. The pore pressure distribution in the heating phase shows that the pore pressure increases to 5 MPa then it remains constant. This result occurs because the hydraulic pressure and the stress are not well simulated in the small modeling domain (Figure 4-13). The stresses at Points A and B increase to 4.5 MPa and then remain constant. This issue will be investigated later with larger domain with the entire geological information. The liquid saturation is well captured in the current model shown in Figure 4-14.
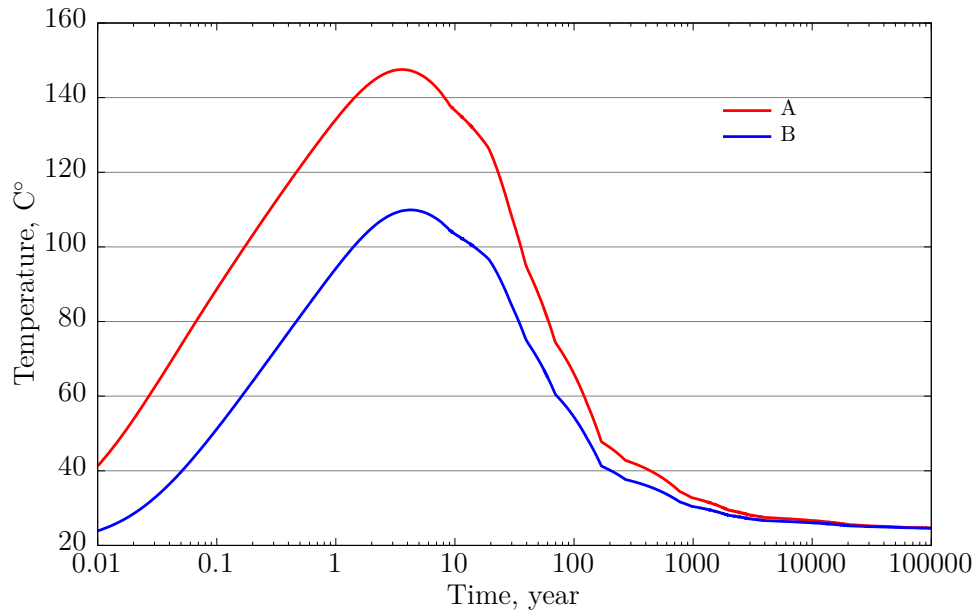
**Figure 4-11. Simulation results of temperature at Points A and B in "high T" case**
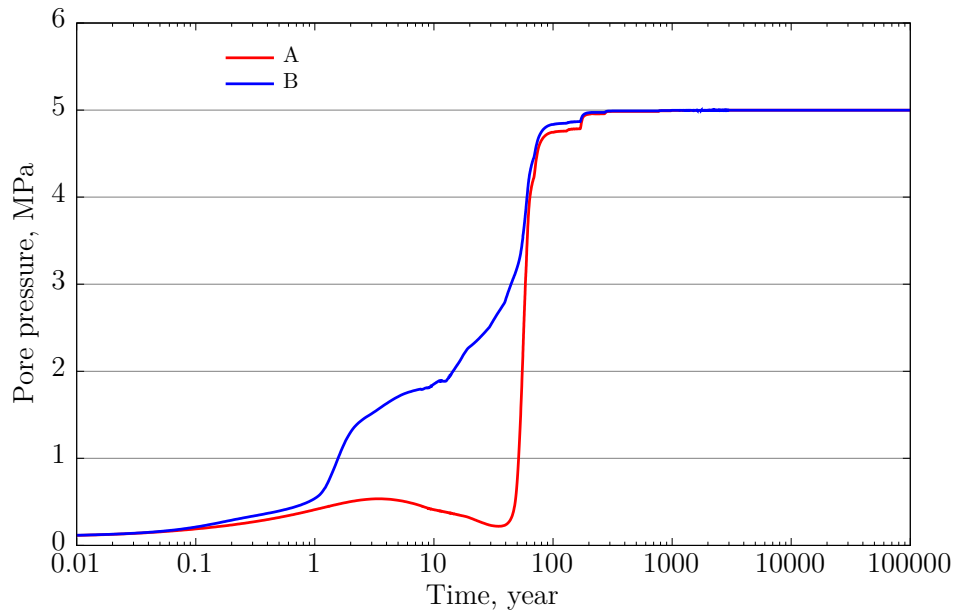


**Figure 4-12. Simulation results of pore pressure at Points A and B in "high T" case**
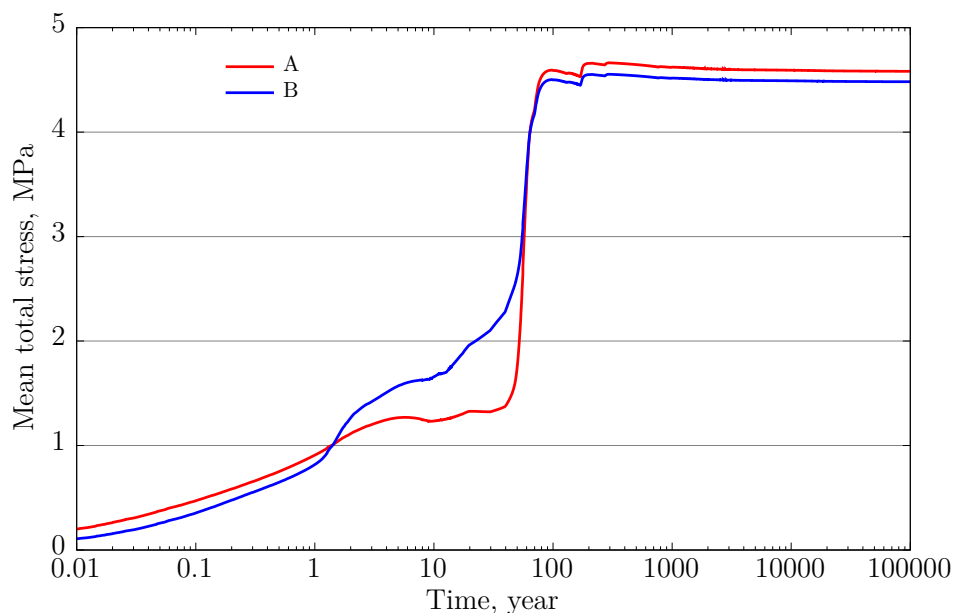
**Figure 4-13.  Simulation results of mean total mean stress at Points A and B in "high T" case**
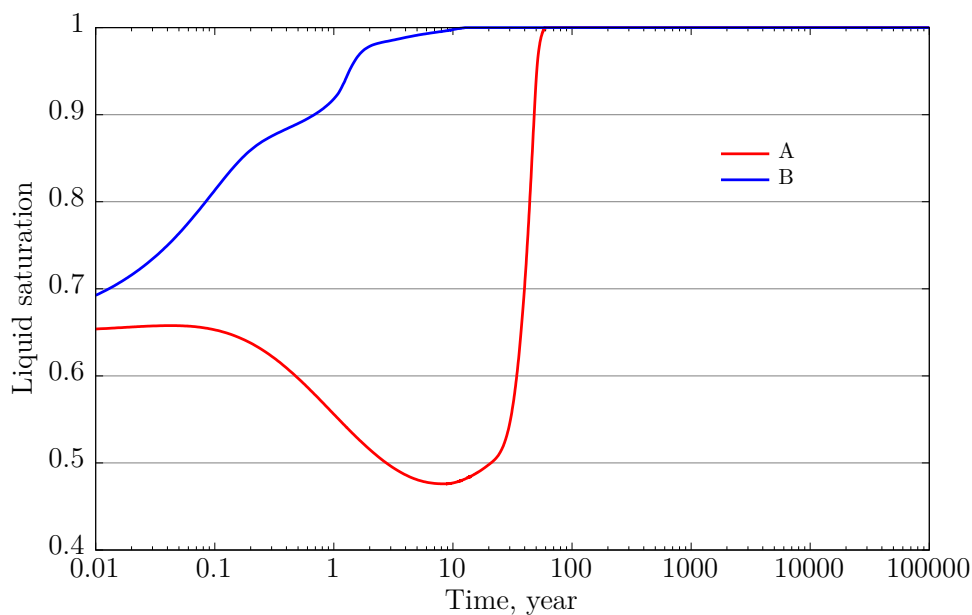


**Figure 4-14.  Simulation results of liquid saturation at Points A and B in "high T" case**

## 4.6    Summary and Future Work

### 4.6.1    Summary of Current Modeling Work

In the past few years, we have dedicated our efforts to developing a coupled THMC model to evaluate the chemical alteration and associated mechanical changes in a generic repository, and to consider the interaction between the EBS bentonite and the natural system clay formation. Two main scenarios were developed for comparison: a "high T" case, in which temperature near the waste package can reach about

200°C, and a "low T" case, in which the temperature can reach about 100°C. The coupling between chemical and mechanical processes is the key part of THMC model needed to evaluate the impact of chemical changes on the mechanical behavior. In FY19, we started to use a new simulator TReactMech to work on the Linux platform, which is more suitable for large-scale computation and better able to incorporate other mathematical and physical tools for modeling of THMC processes. The milestones that have been reached are as follows:

- We added the dual structure model, BExM, to link mechanical process with chemistry in TOUGHREACT-FLAC to allow us to simultaneously incorporate the effects of exchangeable cations, ionic strength of pore water and abundance of swelling clay on the swelling stress of bentonite.

- We ran new high T and low T simulations. The ultimate goal is to investigate the thermal limit of clay repository. Reliable evaluation of the impact of long-term geochemical effect on mechanical behavior will help determine whether a clay repository can sustain higher temperature.

- We introduced the new simulator TReactMech on a Linux platform. Based on simulations of an initial 3D THM benchmark test, we obtained good agreement between numerical simulations by TReactMech and TOUGHREACT-FLAC and an analytical solution, which verifies the correctness of the new simulator.

## 4.6.2    Future Work

To improve the simulator for modeling coupled THMC processes, in the remaining time of FY20, we are planning:

- To investigate chemically induced deformation in solid skeleton related to the change of solution compositions, and to derive an improved constitutional model for simulations of the swelling pressure in compacted clays. We are going to develop a stricter MC coupled model in the framework of poromechanics. A better quantitative understanding of how chemical change controls the material structure is required. Studies will be focused on developing and verifying such a relationship and searching data for parameter calibration.

- To derive a reduced order model that can be integrated into the PA model in GDSA. The importance of bentonite alteration and its impact on mechanical behavior needs to be integrated into the PA model to assess their relevance to the safety of a repository. Specifically, we will first implement bentonite swelling models, such as linear swelling, state surface, BBM, and BExM into a parallel THMC simulator TReactMech, and then a reduced order model will be developed based on a large number of THMC simulations.

## 5.  INTEGRATION OF COUPLED THC MODEL WITH GDSA USING REDUCED-ORDER MODEL

### 5.1  Introduction

In parallel with the development of mechanistic models describing various impacts of THMC processes on the EBS (e.g., Rutqvist et al. 2014; Zheng et al. 2017b), within the SFWST Campaign, Sandia has been developing generic PA models by simulating thermal and hydrological processes at the repository scale (Mariner et al. 2017). The PA methodology for nuclear waste disposal has been developed and improved over the past several decades to compute the radiological risk to public health (e.g., Rechard et al. 2014). The current PA model includes the repository structure (i.e., canister arrays and tunnels) as well as the multiple components along the radionuclide transport pathway, from waste packages to EBSs, to the natural geological environment, and finally to the biosphere.

However, there remains the challenge of integrating THMC/THC complex processes within EBS into the overall PA, on account of model complexity and computational cost. This creates two problems for both planning/designing disposal systems and developing comprehensive PA models. First, the uncertainty associated with these processes is not accounted for in the overall PA. Although conservative assumptions could be developed, it is often difficult to justify such assumptions for complex systems involving formidably intricate parameter interactions and feedbacks. Second, without having all the processes integrated, it is impossible to identify which parameters are important for reducing the overall uncertainty, or what kind of measurements/datasets need to be collected during the performance-confirmation process.

Over the past several decades, ROMs have been developed for nuclear waste disposal and general subsurface system applications in order to integrate complex processes into PA models. These initial efforts were made to simplify physical/mechanistic models of disposal systems and to incorporate flow and radionuclide transport models into multiple canister configurations—for example, through compartment-model representation (Ahn et al. 2002; Murakami and Ahn 2011). Although such ROMs can provide intuitive representation, their applicability is often limited, since they are site or system-specific and not scalable to other types of environments and repository configurations. Recent ROM developments have been focused on mathematical and statistical methods, such as polynomial chaos expansion (PCE) or Gaussian process regression, which use an ensemble of Monte Carlo simulation results from high-fidelity model runs (e.g., Pau et al. 2014; Swiler et al. 2019). The effective uncertainty quantification has been demonstrated based on ROMs (Pau et al. 2014; Wainwright et al. 2014). These statistical methods provide a flexible way to reduce the complexity of models that can be applied to any system or under any condition, although their performance has to be tested and validated, particularly for highly nonlinear systems.

The ultimate goal of this study is to develop a ROM-based methodology and toolsets for integrating complex, coupled models (such as THMC or THC) into the overall PA of nuclear waste disposal. The particular focus is to compute the spatial/process-integrated adsorption partition coefficient ($K_d$) in the PA models. The single-canister THMC/THC models, for example, include a complex geochemical model resolving each clay mineral type, surface/aqueous complexation as well as fine domain discretization. The PA model, on the other hand, may have only one grid block for a container and buffer in the EBS to describe the transport of radionuclides using the $K_d$. Using ROM, we aim to compute the buffer-averaged $K_d$ as a function of time and various parameters. The ROM is used to construct probabilistic distributions to take into account the uncertainty associated with those parameters as well as the processes not included/resolved in the PA model. The PA model can take the determined $K_d$ values according to those parameters in the uncertainty quantification (UQ).

In this report, as the first step, we evaluate the spatial temporal evolution of $K_d$ with the buffer-host rock system. The host rock (argillite) is assumed to have the properties of Opalinus Clay (Bossart 2011;

Lauber et al. 2000). We then perform a GSA using the THC model developed in a bentonite-argillite system. The GSA is used to evaluate the impact of each parameter on the performance measure ($K_d$ in our case) over the full range of multidimensional parameters (Wainwright et al. 2014). GSA can investigate the nonlinearity and interactions among parameters needed to improve our system understanding. It is particularly important to select the parameters to be included in the ROM. We have set up the pipeline between the simulation optimization and the calibration code iTOUGH2 and the THC code TOUGHREACT for GSA. This set-up can further be used for the ROM development.

## 5.2  Model Setup

### 5.2.1  THC Model

While the detailed THC model is described in Chapter 3 of the FY19 report (Zheng et al. 2019), the model is described here for completeness. The model domain includes two material zones for the bentonite and argillite host rock. Bentonite is located within the interval from 0.45 m to 1.135 m from the heat source, with the remaining domain up to 50 m used to simulate the host rock. The initial conditions in the model domain were: temperature of 12°C, EBS bentonite water saturation of 59%, and a suction of $1.11 \times 10^5$ kPa. The host rock was fully saturated. The model simulation was conducted in a nonisothermal mode with a time-dependent heat power input (Rutqvist et al. 2014). Two-phase flow models were used to simulate the unsaturated stage in the bentonite barrier. The bentonite becomes fully saturated before the assumed canister failure time of 1000 years.

To describe the U transport, the model use a two-site protolysis nonelectrostatic surface complexation and cation exchange sorption model—2 SPNE SC/CE (Bradbury and Baeyens 2011). In this model, surface protonation reactions that involve a strong site and two weak sites are used to describe acid-base titration measurements, whereas surface complexation reactions with the one strong site and two weak sites are needed to describe the sorption edge and isotherm measurements for the sorption of U(VI) on smectite (montmorillonite) and illite. In addition, the model includes aqueous complexation (particularly, carbonate species), and cation exchange reactions. A numerical model was developed using TOUGHREACT. After the simulation, we computed the "apparent" $K_d$ value at each grid point based on the ratio of the concentrations between the aqueous phase and solid phase.
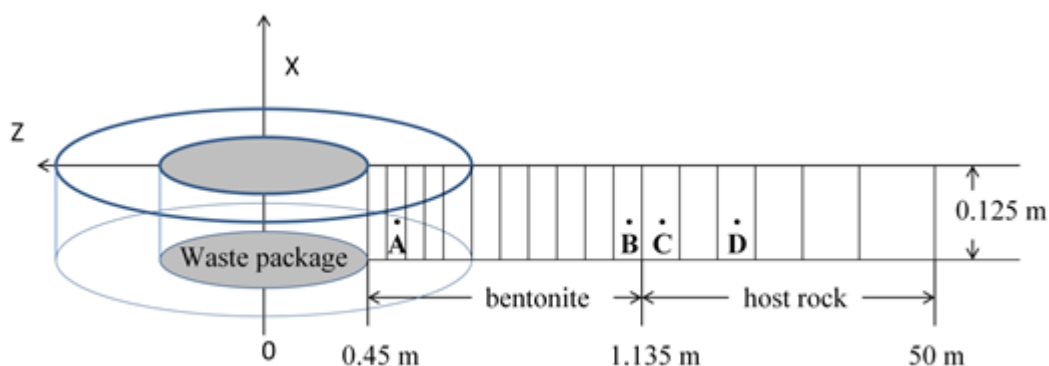


NOTE: Not to scale. Points A and B are located within the bentonite at $r = 0.479$ m and $r = 1.13$ m, respectively, and Points C and D are within the host rock at $r = 1.285$ m and $r = 11.07$ m, respectively.

Source: Zheng et al. 2019.

**Figure 5-1.  Mesh used for the THC model**

### 5.2.2    Global Sensitivity Analysis using THC-iTOUGH2

In general, a sensitivity analysis examines the relation between a parameter that is an input to the numerical model, and an observable variable that is an output of the numerical model. Sensitivity analyses have been used to (1) build parsimonious data-driven models, (2) identify key processes in diagnostic models, (3) determine influential factors in prognostic models, and (4) defend the robustness of a particular model. More specifically, sensitivity analyses can help to (5) identify which (uncertain) parameters have the greatest effect on model predictions and prediction uncertainties, and consequently (6) which properties need to be estimated with high accuracy. In contrast to the derivative-based, local sensitivity method (Cacuci 2003), GSA methods, such as the Morris and Sobol' methods (Morris 1991; Sobol 2001; Saltelli et al. 2008), explore the parameter space so that they provide robust sensitivity measures in the presence of nonlinearity and interactions among parameters. The Morris one-at-a-time (OAT) method is a computationally frugal method that changes one parameter at a time from randomly generated reference parameter sets, and computes the difference in outputs.

In this work, we coupled iTOUGH2 (Finsterle 2010) with TOUGHREACT through the PEST protocol. iTOUGH2 has been developed as an inverse modeling and parameter estimation tool for various modules of the nonisothermal multiphase flow and transport simulator TOUGH2 (e.g, Pruess et al. 2012). As analysis capabilities have been added, iTOUGH2 has become an integrated framework for hydrogeological modeling under uncertainty—from test design to site characterization to prediction—including parameter estimation, uncertainty analysis, sensitivity analysis and ROM (Pau et al. 2013). Moreover, all iTOUGH2 analysis tools can be applied to any stand-alone, text input/output (I/O)-based simulator through the use of the PEST interface (Finsterle 2010; Finsterle and Zhang 2011).

The ranges of the chemistry parameters used for the sensitivity analysis are tabulated in Table 5-1.

**Table 5-1. List of parameters and their range that are varied within GSA**

| Parameters | Range |
|---|---|
| Site density ($cm^2$/g): ill_sOH | $10^{-6} - 10^{-4}$ |
| Site density ($cm^2$/g): ill_w1OH | $10^{-6} - 10^{-4}$ |
| Site density ($cm^2$/g): ill_w2OH | $10^{-6} - 10^{-4}$ |
| Site density ($cm^2$/g): sme_sOH | $10^{-6} - 10^{-4}$ |
| Site density ($cm^2$/g): sme_w1OH | $10^{-6} - 10^{-4}$ |
| Site density ($cm^2$/g): sme_w2OH | $10^{-6} - 10^{-4}$ |
| Initial pore water composition: $Ca^{+2}$ | $10^{-3} - 10^{-1}$ |
| Initial pore water composition: $H^+$ | $10^{-9} - 10^{-7}$ |
| Volume fraction: smectite | $0.3 - 0.95$ |
| Volume fraction: illite | $0.01 - 0.2$ |

## 5.3    Results of Simulations of $K_d$

### 5.3.1    $K_d$ in Reference Case

Figure 5-2 shows the temporal evolution of pH and U(VI), calcium and carbonate aqueous concentrations at the four points within the buffer and host rock. In Figure 5-2(a), the pH is stable within the bentonite for the first 10,000 years due to the buffer created by surface protonation reactions, and then increases from 10,000 to 30,000 years, and eventually plateaus until 100,000 years. The increase in pH is attributed to the processes of dissolution of smectite and precipitation of illite (i.e., illitization), which consume protons. The calcium and carbonate concentrations (Figure 5-2(b) and (c)) decrease, as the pH increases after 30,000 years.

The U(VI) concentration increases near the canister (Figure 5-2(d), Point A), but not significantly at the rock/buffer interface (Points B and C). The bentonite barrier is effectively retarding the migration of U(VI) released from the waste package. U(VI) concentration at Points B and C is not significantly above the background U(VI) concentration, and decreases below the background after 10,000 years when pH increases. This is because the decrease in $HCO_3^-$ concentration leads to stronger strong adsorption of U(VI).
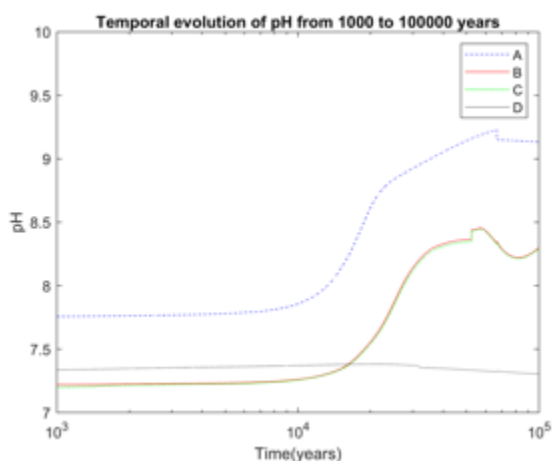


(a)
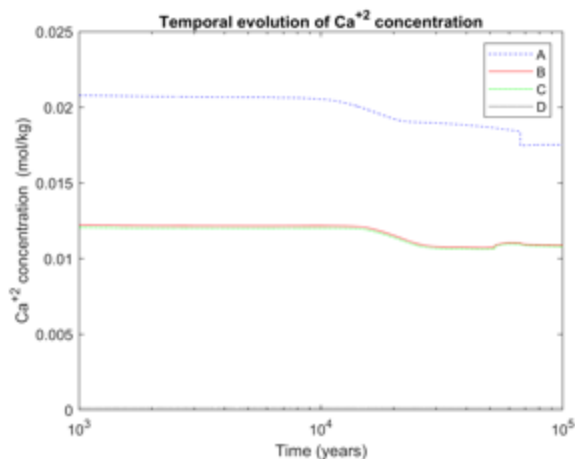


(b)
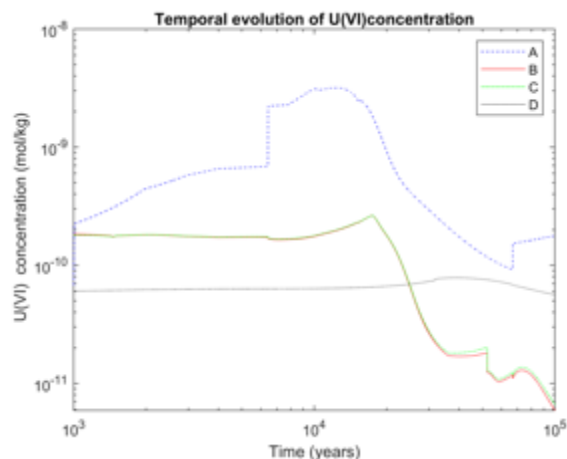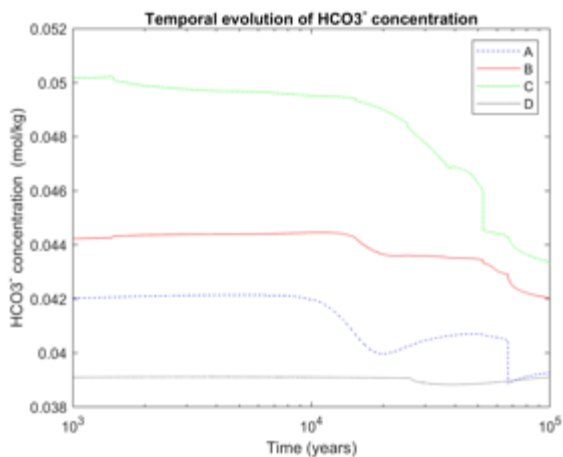
(c)                                                                              (d)

**Figure 5-2.  Simulated (a) temporal evolution of pH, and (b) concentration of calcium,
(c) concentration of carbonate, and (d) concentration of U(VI) at Points A–D.**

Based on the simulated U(VI) concentrations in the aqueous and solid phases, we computed the $K_d$ values at each grid block (Figure 5-3). The $K_d$ values vary with time and space within the same material. The $K_d$ has a one-order-of-magnitude difference within the bentonite buffer, and more than two-orders within the host rock. The $K_d$ values increase at all the locations around 30,000 years, as the pH increases and carbonate concentration decreases, which is shown in Figure 5-3. Although the variability is large, the temporal evolution is "spatially consistent" since the lines are approximately parallel within the EBS and the buffer/host-rock interface.
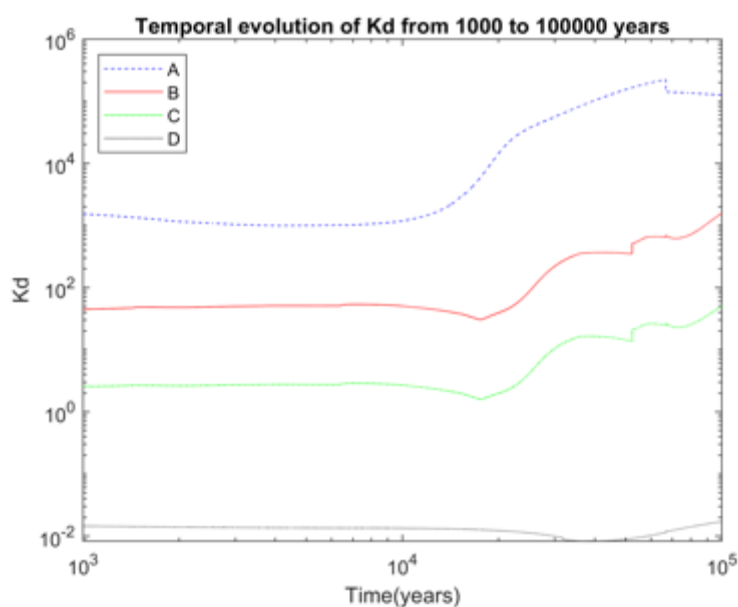


**Figure 5-3.  Simulated $K_d$ at Points A–D as a function of time**

(a)

(b)

(c)

(d)
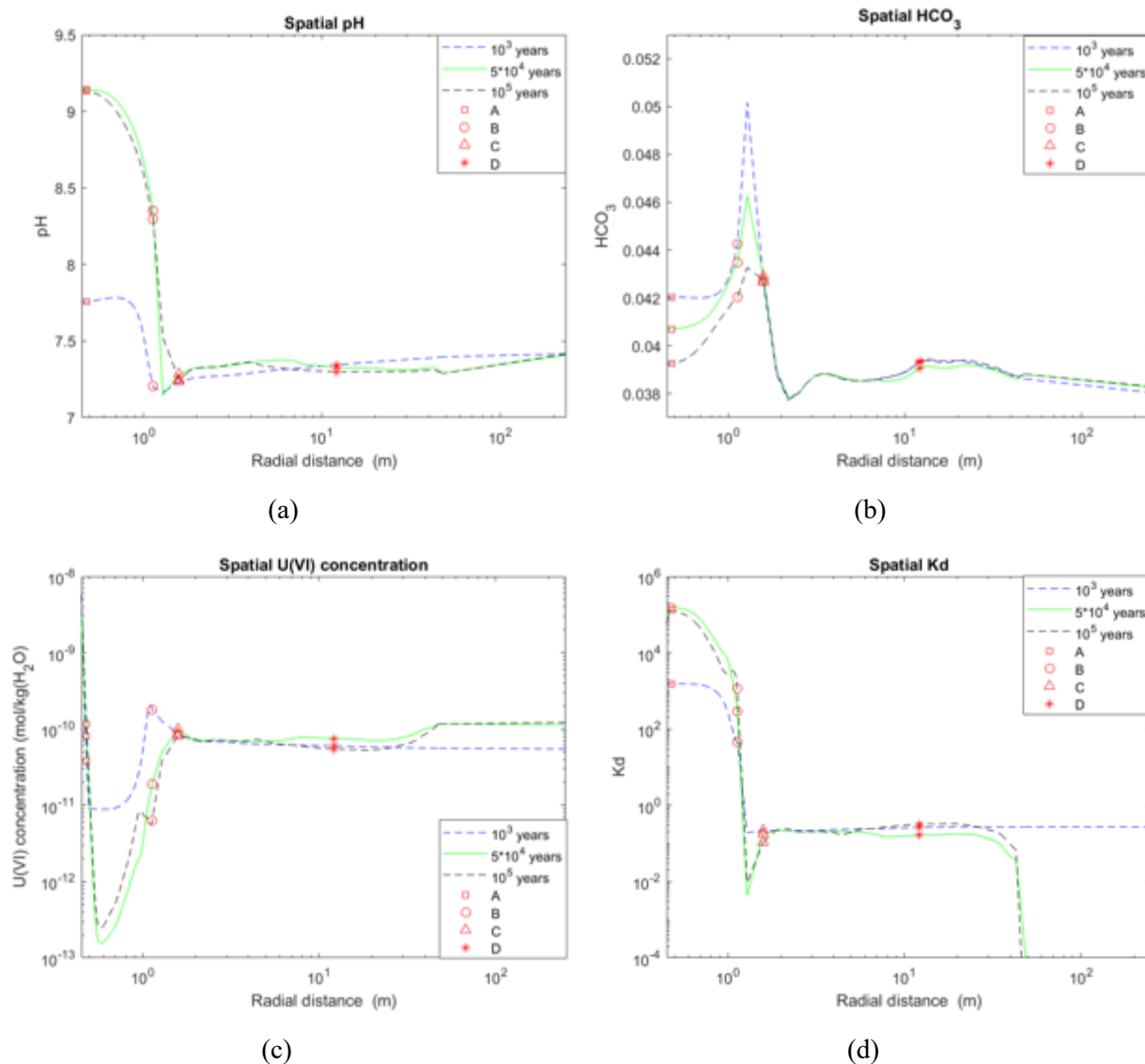
**Figure 5-4. Simulated (a) temporal evolution of pH, (b) carbonate concentration, (c) U(VI concentration, and (d) $K_d$ as a function of space and time (1000, 50,000 and 100,000 years)**

The radial distribution of $K_d$ shown in Figure 5-4 indicates that $K_d$ is higher near the canister, and gradually decreases toward the buffer/rock interface. The $K_d$ profile is similar to the pH profile at these three time points. The carbonate concentration, on the other hand, increases with the distance from the canister toward the buffer/rock interface, and it decreases in the host rock. The dependency of $K_d$ on the pH and carbonate concentration is shown in Figure 5-5. The $K_d$-pH relationships are approximately linear over time with the positive correlations at the three points (A, B, and C; except for the point within the host rock) with a similar slope (i.e., parallel lines). However, the $K_d$ vs. pH relationship obtained in this study is different from that determined by Dong et al. (2012), Bea et al. (2013), and Tournassat et al. (2018), who evaluated the $K_d$ decrease in the pH range from 7 to 9, assuming that carbonate concentration remained constant. The increase of the $K_d$ with the increase of pH, determined in the current study, can be

explained by the fact that the carbonate concentration decreases as the pH increases, hence decreasing the concentration of carbonate complexes with U(VI).
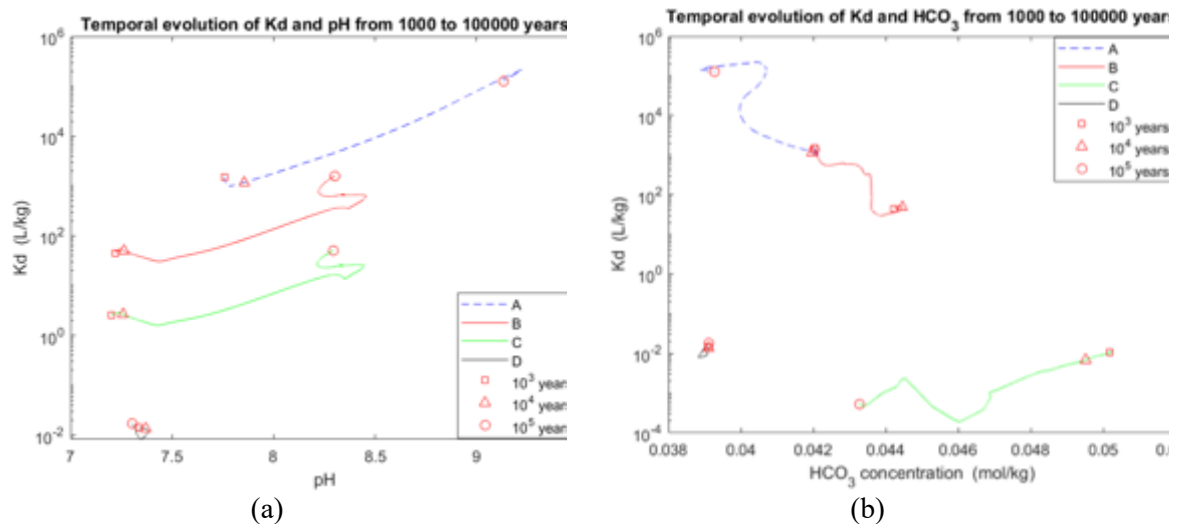


NOTE:    The lines represent the four points. The time stamps are placed to represent the temporal changes.

**Figure 5-5.  Simulated (a) K$_d$ versus pH and
(b) K$_d$ versus carbonate concentration at Points A–D**

We also evaluated the application of different statistical methods for spatial averaging of K$_d$ in the buffer, since the PA model typically includes only a single grid block to represent the buffer. Figure 5-6 shows that simple (arithmetic) averaging (green line in Figure 5-6) gives higher K$_d$ values, since K$_d$ values vary over one-order of magnitude across the buffer, and the higher K$_d$ values increase the averaged value. The geometric mean – which is often used for spatial averaging of permeability – still over estimates K$_d$. It is apparent that the uncertainty in calculations of K$_d$ could also be caused by calculations of K$_d$ as the ratio of the total concentration in the solid over the aqueous phase concentration using different numerical block volumes, which increase with the radial distance in the cylindrical coordinate model domain.
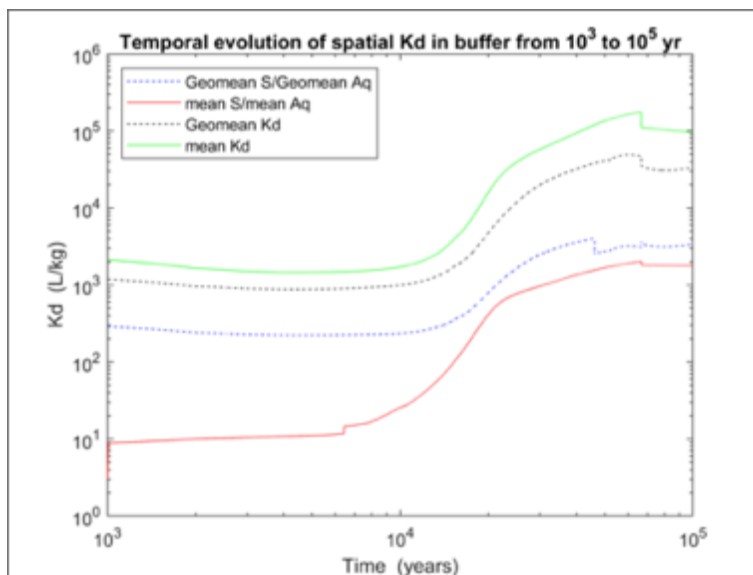
NOTE:   "Geometric mean S/ Geometric mean Aq" is the geometric mean (or averaging) of solid concentrations at all the grid blocks divided by the one of aqueous concentrations, "mean S/mean Aq" is the simple mean of solid concentration divided by the one of the aqueous concentrations, "Geomean $K_d$" is the geometric mean of $K_d$ at all the grid blocks, and "mean $K_d$" is a arithmetic mean of $K_d$.

**Figure 5-6.  Comparison of different $K_d$ values spatially averaged over the buffer**

## 5.4    Summary and Future Work

In this study, we are developing a methodology to couple the detailed THC model with the PA model. The particular focus is on using the THC model for computing the $K_d$ as a function of time and space and an averaged across EBS, which can be plugged into the PA model. As the first step, we simulated the THC process within a buffer-argillite system using TOUGHREACT, and computed $K_d$ at each grid block over time.

The results show that although the $K_d$ varies for more than one order of magnitude over the space and time, the temporal evolution is spatially consistent, indicating similar trends of the $K_d$ values at all the grid blocks. This would make it possible to develop the statistical representation of the $K_d$ evolution across the space in a relatively straightforward manner. In addition, the dependency of $K_d$ on pH is fairly linear, which could also be used to create the ROM, although the dependency has to be evaluated for different geochemical conditions and parameters in the UQ study. The spatial averaging was applied to determine the $K_d$ value representing the entire buffer as a single grid block in the PA model. The $K_d$ value averaged over the buffer overestimated the overall adsorbed mass, compared to the apparent $K_d$ over the buffer (calculated based on the buffer-averaged adsorbed and aqueous concentrations). Validation of the results of numerical studies is needed based on a comparison with experimental data.

# 6.  STUDYING CHEMICAL CONTROLS ON MONTMORILLONITE STRUCTURE AND SWELLING PRESSURE

## 6.1   Introduction

Clay rich materials are critical components of engineered barriers for the safe long-term storage of nuclear waste. Swelling clays, such as montmorillonite clays, are particularly valuable for EBS barriers because their expansive behavior is expected to provide a mechanical support to repositories and close pathways for preferential flow or diffusion. Despite many decades of study, predictive models for swelling and diffusion-driven mass transport through swelling clays remain elusive. It is well established that montmorillonite clays adopt crystalline or osmotic swelling states with given water contents (Holmboe and Bourg 2013; Norrish 1954; Rotenberg et al. 2009). It is not presently possible to predict swelling pressure and microstructure under relevant and dynamically changing conditions. Numerous physical and chemical variables have been shown to have a major influence on clay swelling: clay layer charge, water activity, electrolyte ion composition, and confining pressure being the dominant controlling variables (Sun et al. 2015; Teich-McGoldrick et al. 2015). Other factors, such as the crystalline alignment of individual clay layers, have shown to depend on ion composition, and are, therefore, likely to influence swelling (Whittaker et al. 2019). Moreover, the macroscopic swelling pressure and transport properties are governed by the microscopic structure of swelling clays. Compacted clays are composed of particles of stacked clay mineral layers, also called tactoids, which are arranged in complex, but poorly understood arrangements.

In this work package, we combine novel experimental and simulation studies to address critical needs for the development of improved models for clay swelling and diffusive transport.

First, we implemented molecular-scale models to quantify the relative free energies of montmorillonite clay systems under different physical configurations and aqueous solution conditions. Traditional models implementing the Derjaguin-Landau-Verwey-Overbeek (DLVO) and the Modified Gouy-Chapman (MGC) theory can reasonably predict osmotic swelling (in symmetric monovalent, low ionic-strength electrolyte) provided molecular-level information (e.g., distance of closest approach) is available; however, these continuum model predictions break down for hydrates with basal spacing ~ 10–12 Å (1–2 water layers), where water molecules need to be treated as discrete. Our novel approach explicitly links the molecular and continuum scales by parameterizing thermodynamic models for the equilibrium distribution of coexisting swelling states directly from these molecular-scale energetic data. This work integrates molecular and continuum scale modeling efforts to upscale simulation results towards the development of a predictive macroscopic model of mass transport in engineered clay barriers.

Second, we constructed complementary experimental systems to interrogate the dynamic structural rearrangement of swelling clays under conditions relevant to EBS operation. As described in Section 4.4 of Zheng et al. (2019), we constructed a specialized oedometer for measuring the swelling pressure of compacted clay and simultaneously measuring key aspects of the clay microstructure using synchrotron x-ray methods. This system was constructed by collaborators at the BRGM, France, and testing and calibration have been completed. The system was scheduled to be delivered to LBNL by October 16, 2019 for laboratory experiments. An in-situ small-angle x-ray scattering (SAXS) experiment to obtain quantitative distributions of pore sizes during interlayer ion exchange was scheduled for November 20–22, 2019. In a further approach described below in Section 7, x-ray nanotomography will be developed to imaging swelling structural transformations with ~40-nm resolution.

## 6.2   Atomistic Simulations of Cis-vacant MMT

Molecular simulations have proven to be effective for predicting the structural and dynamical properties of layered silicate minerals, including clays. The molecular simulation also indicated that the detailed

consideration of the clay structure and charge distribution significantly impact the ion adsorption (Lammers et al. 2017) and mass transport properties in the interlayer (Tournassat et al. 2016). Prior studies have shown that simulations using classical descriptions of interatomic forces can capture the equilibrium structures of hydrated swelling clays and micas, the diffusivity of interlayer ions, and the transformations between crystalline swelling states as a function of water activity. To date, all prior simulation studies have investigated clays with a trans-vacant *(tv)* structure, while most montmorillonite clays have a cis-vacant *(cv)* structure. Thus, the initial goal of our simulation effort, and the starting point for parameterization of the proposed model for clay swelling, was to develop a molecular model for cis-vacant clay that mimics the structure of Wyoming montmorillonite (Wy-MMT). First, we developed a more accurate structural description of montmorillonite, and second, we attempted to validate the model through comparison of the energy landscape for the rotation of stacked MMT layers against recently acquired imaging data (Whittaker et al. 2019).

## 6.2.1    Modeling the Cis-vacant Clay Layer

While several atomistic models have simulated the diffusion (Bourg and Sposito 2011), exchange kinetics (Tournassat et al. 2016) and swelling (Hsiao and Hedström 2017; Teich-McGoldrick et al. 2015) in MMT clays, an assumption of centrosymmetry is imposed by considering clay sheets with trans-octahedral vacancy positions. This assumption yields a pyrophyllite-like structure (which is trans-vacant) whereas available data indicate that most MMT have cis-vacant structure (Zheng et al. 2019, Figure 4-1; Drits and Zviagina 2009).

The key product of this activity is the first atomistic model for 2:1 cis-vacant clay that is directly comparable to experimental data, and we use this clay layer model henceforth in all our simulations.

### 6.2.1.1    Simulation Configuration

Interatomic interaction terms through van der Waals forces and electrostatics are obtained from ClayFF, which is a robust classical force field for a range of mineral interface simulations. The interaction parameters for the water molecule are obtained from the extended simple point charge (SPC/E) water model (Mark and Nilsson 2001). The Lennard-Jones interaction terms between unsimilar atom types are calculated via Lorentz-Berthelot mixing rules. We employ periodic boundary conditions in our simulations, a cutoff distance of 15 Å for short-range interactions, and Ewald's summation method with an accuracy of 99.99% for long range electrostatics. A grand canonical Monte Carlo (GCMC) approach with a target chemical potential, $\mu$, that of an imaginary reservoir, in combination with molecular dynamics (MD) simulation in the grand canonical ensemble ($\mu$VT) was employed to determine the amount of water adsorbed in the interlayers for a given basal spacing. The temperature and pressure of the reservoir were fixed at 300 K and 1 atm, respectively, with a bulk density of 0.998 g/cm$^3$. We obtained the target chemical potential from a GCMC simulation of pure water at 300 K in a box of size $40 \times 40 \times 40$ Å$^3$ resulting in ~2100 molecules. Using this target chemical potential of −49.0 kJ/mol (Boţan et al. 2011), insertions and deletions of water molecules occur in the clay interlayer in combination with Monte Carlo moves such as translation and rotation of molecules to yield the hydrate of MMT in pure water. The system was subsequently equilibrated in the canonical (NVT; T = 300 K) ensemble for 1 ns and subsequently, in the isothermal-isobaric systems (NPT; P = 1 atm, T = 300 K) for 5 ns to allow for the diffusion of water and ions.

### 6.2.1.2    Interlayer Structure of Cis-Vacant MMT

The resulting hydrate contained 5 water molecules per unit cell per layer for Na-MMT and 4.95 water molecules per unit cell per layer for K-MMT. Bourg and Sposito (2011) reported an average of 5.1 water molecules per unit cell for the water layer bound to *tv* MMT, and we infer that the difference in water content in the adsorbed layers is due to the slightly more hydrophilic nature of *tv* MMT (Minisini and Tsobnang 2005). Atomic density profiles for equilibrium one-layer (1W) and two-layer (2W) hydrates for

Na-MMT and K-MMT are presented in Figure 6-1. In addition to atomic radii being a factor, the more negative hydration enthalpy of sodium resulted in a 1W Na-MMT hydrate with higher water content than its K-MMT equivalent. For the 2W states with a basal spacing of ~15.5Å, the difference in water content was less significant. While the arrangement of interlayer water perpendicular to *c* was notably similar in the sodium and potassium cases, the preferential residence of the cations was different. In the 1W and 2W cases for Na-MMT (Figure 6-1(a) and (c)), the sodium cations tend to reside in the interlayer midplane. Studies have confirmed that sodium ions prefer tightly bound hydration shells and therefore, are likely to be in the middle surrounded by interlayer water (Teich-McGoldrick et al. 2015; Honorio et al. 2017).

The equilibrium structure for K-MMT, on the other hand, revealed that potassium ions preferred residing in the interlayer midplane in the 1W case (Figure 6-1(b)), and close to the basal surfaces in the 2W case (Figure 6-1(d)). Existing reports for potassium hydrates present conflicting data, particularly for the 1W configuration. Liu and Lu (2006) performed MD simulations on an Arizona-MMT model wherein the potassium ions form inner sphere complexes with the ditrigonal cavities of the clay layer and consequently, exist close to the clay layer. Similarly, Tambach et al. (2004) inferred through molecular simulations that potassium ions, with their relatively small hydration energy, favored less hydration and screened the negatively charged clay platelets more effectively than sodium and therefore, would likely exist on the clay surface. It should be noted that both these molecular models were of trans-vacant configurations of MMT. However, Vao-soongnern et al. (2015) presented x-ray adsorption spectroscopy data that indicate the residence of potassium above the ditrigonal cavities on the *a-b* plane but in the midplane for the 1W structure, and bound to the basal surfaces in the 2W structure along *c*. The results of our study agree with this observation and are also confirmed by TEM data (Whittaker et al. 2019) for the 2W case. The favorable local charge compensation mechanism in *cv* MMT alluded to in the introduction section leads to a reduction in the surface basal charge of the clay layer. This could explain the weaker adsorption of potassium ions in the 1W structure. Its large atomic radius combined with a poor tendency to hydrate could cause it to migrate to towards the basal surfaces as the water activity increases when more water is squeezed into the interlayers.



(a)



(b)

(c)

(d)
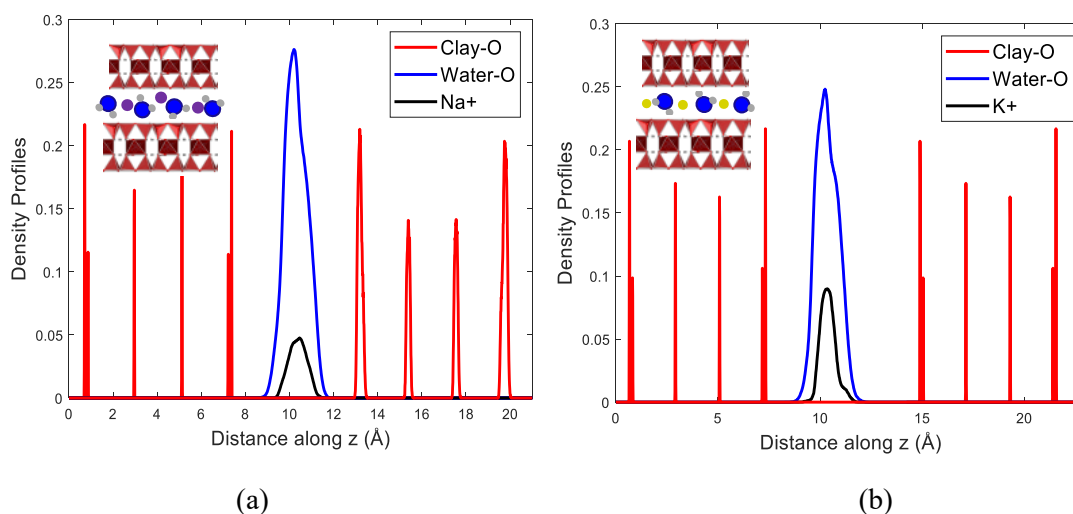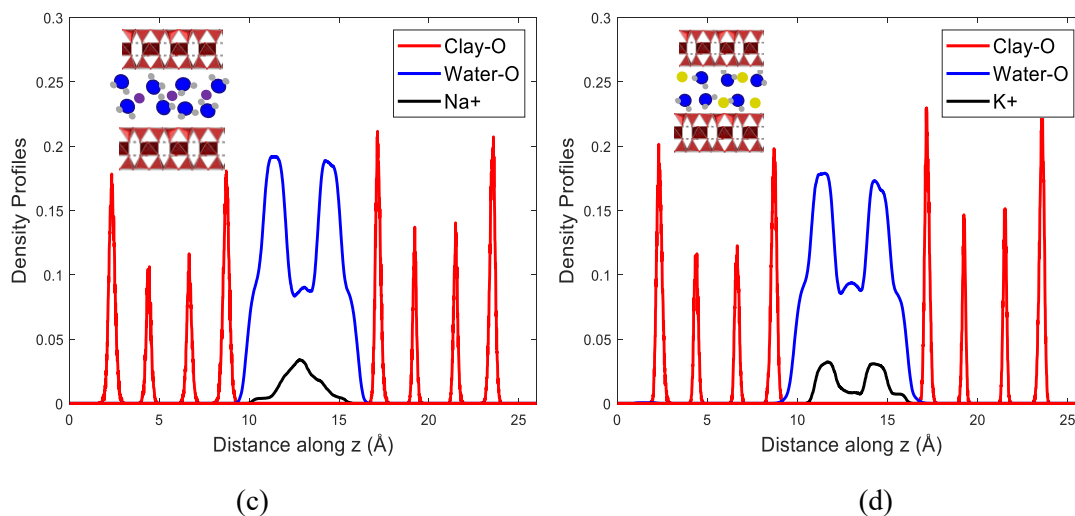
**Figure 6-1. Interlayer atomic density profiles of water ions for cis-vacant MMT for (a) 1 water layer Na-MMT, (b) 1 water layer K-MMT, (c) 2 water layer Na-MMT, and (d) 2 water layer K-MMT**

In addition to the interlayer structure perpendicular to the plane of clay layers, we also studied the adsorption of water in the interlayer parallel to the clay surface. Figure 6-2 presents the density map of interlayer water in a 2W hydrate, acquired from snapshots every 100 ps over the duration of 10 ns equilibration. The water density map correlated strongly with the position of the hydroxyl group in both *tv* and *cv* clay, whereas the presence of adjacent hydroxyl groups seemed to induce more structure to the water in *cv* clay. As a result, the near-surface water profile on *cv* clay is more 'ice-like' and a larger proportion of water molecules in the first monolayer is tightly bound to the clay surface.



(a)

(b)

(c)                                                                                        (d)
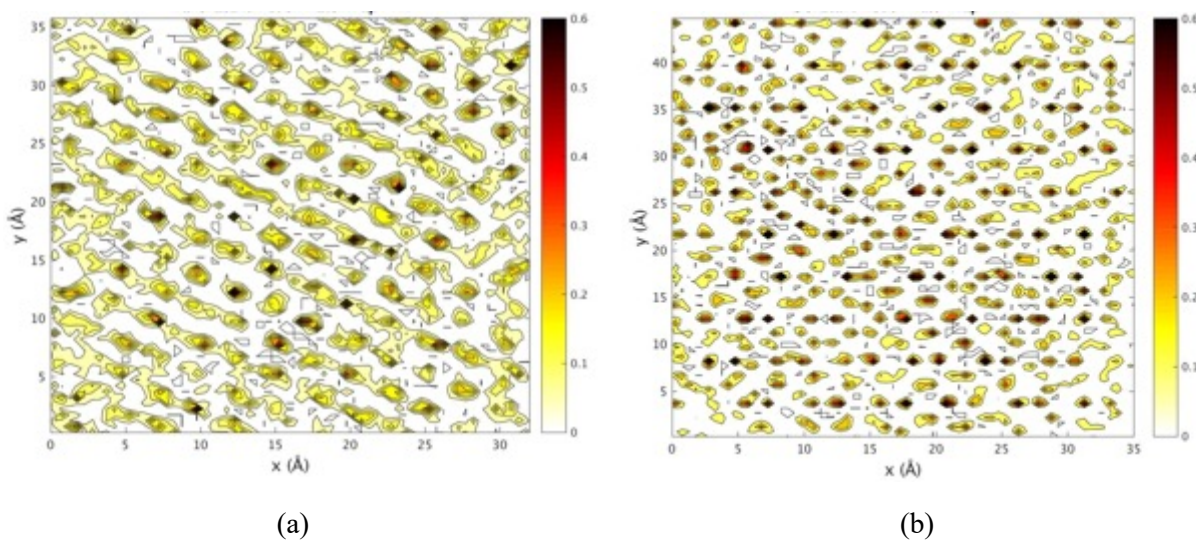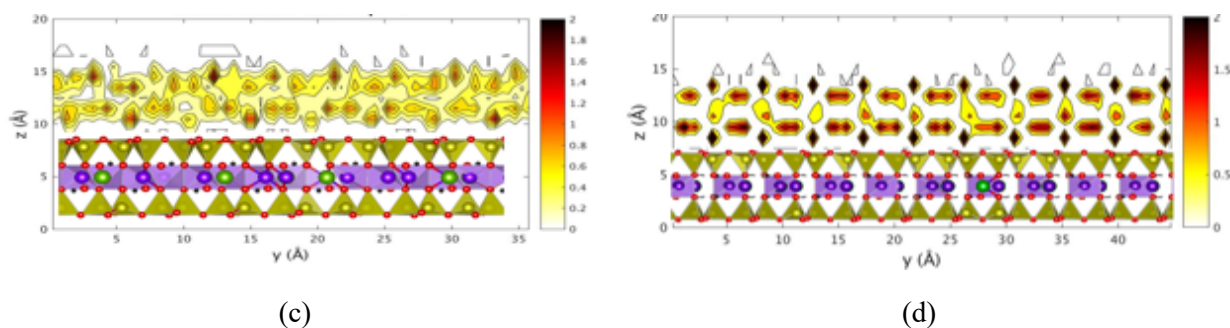
**Figure 6-2.  Density map of interlayer water: on the x-y plane (a) trans-vacant surface and (b) cis-vacant surface, and on the x-z plane (c) trans-vacant surface and (d) cis-vacant surface**

## 6.2.2     Rotation Energetics for Clay Stacking

We investigated the stacking behavior by performing MD simulations of MMT in bulk water for energetically favorable rotational configurations. We report here the final results of the study that was partially described in Section 4.2.2 of Zheng et al. (2019).

### 6.2.2.1     Simulation Configuration

Two layers of MMT—a large square layer containing 180 unit cells, and a hexagonal MMT layer on top containing ~ 45 unit cells—are stacked with monovalent ions in the interlayer (Zheng et al. 2019, Figure 4-2). We employed OH, and $OH_2$ terminations to the edges of the hexagonal top layer to obtain a neutral edge charge. Periodic boundary conditions ensure that the bottom square layer is infinitely large and does not require edge terminations. The top layer is far enough (> 1.5 nm) from the edges of the simulation volume in order to avoid cross-boundary interactions with its image. Four configurations are chosen to study energetically favorable stacking preferences with relative misalignments of 0° (perfectly aligned), 30°, 60°, and 120° between the two MMT layers. These configurations also ensure that the distances across the boundary between the periodic images of the top layer stay consistent for comparison of energy landscapes. The system was first equilibrated in the NVT (T = 298 K) ensemble for 1 ns and subsequently, in the NPT (P = 1 atm, T = 298 K) for 5 ns.

We identified two approaches to studying energetics corresponding to relative orientation: (1) the two layers were held at a predefined misalignment and equilibrated, thus, yielding an average potential energy measure; (2) the two layers were actively rotated relative to each other yielding instantaneous potential energy variations Myshakin et al. (2014). The equilibration of the four configurations (0°, 30°, 60°, and 120°) provided the average potential energy measure. The energy units were normalized to kJ/mol of $O_{20}(OH)_4$.

In order to explore clay particle reorientation at near-crystallographic orientations, the second approach was implemented. Upon rotation of the layers about their relative centers-of-mass, potential energy variations were monitored, and the positions of interlayer species were calculated as a function of the misalignment angle between adjacent clay layers relative to their original positions. Rotation rates ranging from 1°/ps to 0.0005°/ps were explored to avoid energy overshoots during active relative rotation of the layers and found convergence at 0.001°/ps. The density distribution of water and ions remain fairly undisturbed along the direction perpendicular to the plane of clay during active rotation at this rate.

### 6.2.2.2    Simulation Results

The contributions from pair interactions and electrostatics were calculated relative to the energy state of the 0° orientation; in both homoionic clays, the near-crystallographic orientations (0°, 60°, and 120°) exhibited very similar free energies. Based on Figure 6-3 from approach (1) described above in Section 6.2.2.1, the electrostatic interactions were more favorable when the misalignment was 30° between the two layers; however, this configuration resulted in an energy maximum and suggested the presence of an energy barrier to a set of clay layers from rotating freely between 0° and 30°. This energy barrier was nearly 1.5 kT per mol of clay in the Na-MMT and 1.8 kT per mol of clay in the K-MMT case. The relative free energy differences among the 0°, 60°, and 120° cases were slightly lower in the K-MMT compared to the Na-MMT system. This finding is consistent with our TEM images that suggest a higher likelihood for K-MMT to exhibit preferential alignment than Na-MMT (Whittaker et al. 2019).



(a)                                                                                    (b)
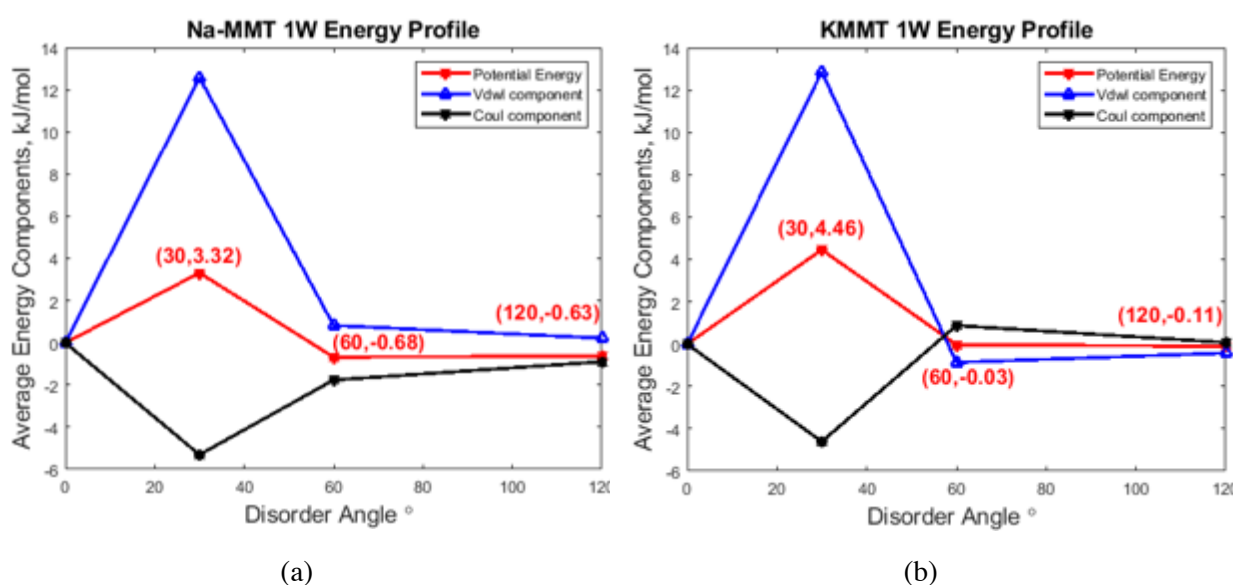
NOTE:    Energy profiles determined from static simulations of favorable (0, 60, 120°) and unfavorable (30°) crystallographic orientations.

**Figure 6-3.  Equilibrium potential energy and energy breakdown for (a) Na-MMT and (b) K-MMT in bulk aqueous solution**

The potential energy variations (with the average equilibrated potential energy of zero) for the 1W and 2W hydrates of Na-MMT using approach (2) are illustrated in Figure 6-4. Results indicate that the potential energy wells during rotation are freely accessible up to relative misalignment angles of 6-8°, which is consistent with observed turbostratic stacking in Na-MMT. While the largest energy well for the 1W hydrate has a magnitude of ~1.5 kT, the 2W hydrates have lower energy barriers to rotations. The addition of water and the subsequent rearrangement of cationic species in the interlayer seem to induce rotational plasticity to the layers in the crystalline swelling regime, i.e., the imposed crystallographic misalignment is irreversible.

TEM data of homoionic montmorillonite (Na-MMT and K-MMT) showed that while turbostratic disorder exists in both cases, the effect is less pronounced in the case of K-MMT. Figure 6-4 presents the energy landscape for K-MMT in the 1W hydrated state. However, our data indicates that the energy barriers of the 1W K-MMT hydrate are in the same order of magnitude as the Na-MMT case. This implies that rotational plasticity of clay crystals does not significantly change for the two cationic species included in the study. We deduce that the energy variations during active rotation are higher than the mean thermal fluctuations observed during equilibration. Although the potential energy ranges appear to be freely accessible, we do not observe large rotational plasticity in these clay crystals (Whittaker et al. 2019).



(a)                                                                                (b)

(c)
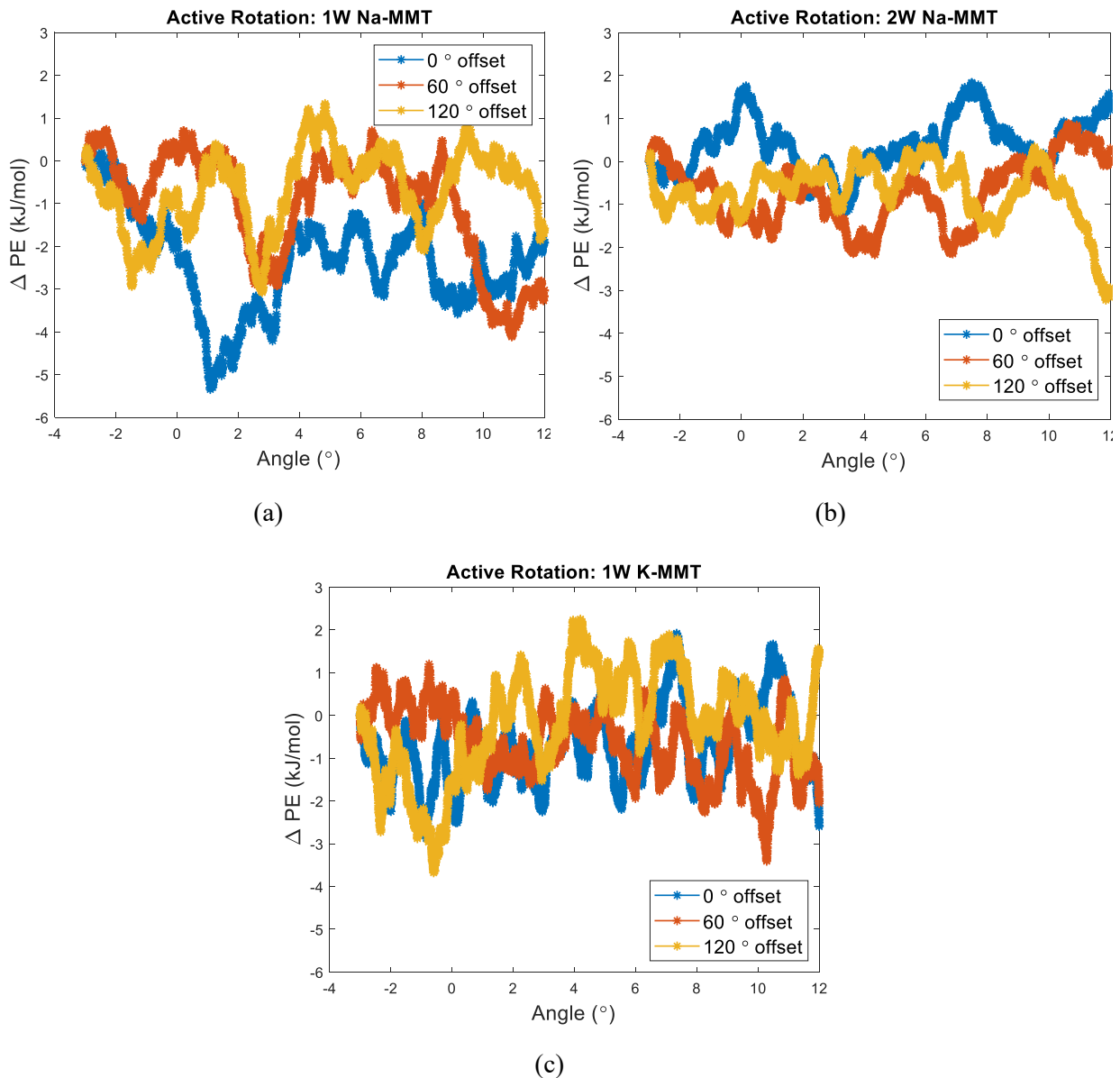
**Figure 6-4.  Potential energy during active rotation for
(a) 1W Na-MMT, (b) 2W Na-MMT, and (c) 1W K-MMT**

### 6.2.3    Summary of Results from Atomistic Simulations

The key findings from the atomistic simulations reinforce the notion that the energy landscape for hydrated montmorillonites favor misalignments between layers yielding turbostratic structure. More layers of water molecules in the interlayer reduce the energy barrier to rotation and perhaps overcome layer-layer interactions that prefer rotational rigidity. Knowledge of the fundamental forces among clay layers and with the interlayer species that contribute to rotational disordering is important for the development of models for swelling and dynamic exchange processes.

## 6.3    Thermodynamics of Mixed-Electrolyte Swelling Clays

### 6.3.1    Thermodynamic Modeling Approach

We are in the process of developing and parameterizing a new thermodynamic model to predict the distribution of coexisting swelling states and/or bulk swelling pressures as a function of water activity and electrolyte composition in saturated aqueous solution. We envision that this model can be directly integrated into reactive transport models such as TOUGHREACT and CrunchFlow. Most existing thermodynamic models for montmorillonite treat clay swelling as a reaction between fully hydrated and anhydrous end-members (Ransom and Helgeson 1994; Vieillard et al. 2011), and have only been developed for single electrolyte swelling reactions. In reality, experimental data show clearly that for a given water activity and electrolyte composition, the clay system contains a mixture of multiple coexisting hydration states such that, for example, 2W hydrates of MMT coexist with 3W hydrates (Berendet et al. 1995; Vidal and Dubacq 2009; Whittaker et al. 2019). Because the molar volumes of clays are not equal to linear mixtures of anhydrous and "fully hydrated" end-members, this approach cannot be used to accurately predict volumetric expansion, swelling pressures, or any terms related to the pressure-volume work in clay rich materials (Vidal and Dubacq 2009). Moreover, perturbations to the bulk electrolyte composition are expected to affect the equilibrium distribution of swelling states (e.g., addition of $K^+$ in a pure NaCl electrolyte suspension will collapse some fraction of clay particles).

Our approach explicitly represents the crystalline hydrates as thermodynamic species in the system and is distinct from existing models in that it determines the equilibrium distribution of swelling states as a function of water and aqueous cation activities. This approach allows us to calculate, for example, changes in bulk volume and bulk distribution coefficient associated with chemical perturbations in solution. A predominance diagram of equilibrium swelling pressures as a function of electrolyte composition for pure Wy-MMT is plotted in Figure 6-5. The swelling pressure is defined following the macroscopic experimental definition as pressure changes required to obtain a definite water content, corresponding to the 1 water layer hydrate, and is given by

$$P_s(m) = P - P_0 \qquad \textit{Equation 6-1}$$

where $P_0$ and $P$ are the pressures of a clay paste before and after volumetric compression, respectively, at water content $m$ after compression (Sposito 1972), with $P_0$ defined as 1 bar.
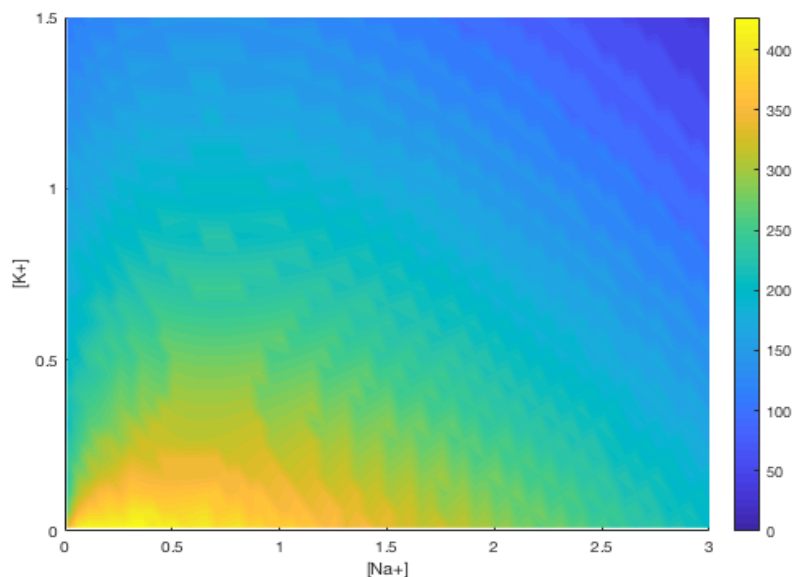
**Figure 6-5.  Calculated swelling pressure (in bars) for Wy-MMT
as a function of aqueous electrolyte concentrations of Na⁺ and K⁺**

While the preliminary version of this thermodynamic model makes the simplifying assumption that both ion exchange and water adsorption reactions within the clays are thermodynamically ideal, accounting for non-ideal solid solution thermodynamics is required to reproduce key aspects of the experimental data. For homoionic clays, a positive excess free energy of mixing between the 2- and 3-water layer crystalline hydrates explains the lack of phase coexistence. We employ MD simulations of clay swelling for homoionic and mixed ion clays to determine the physiochemical basis for observed phase mixing thermodynamics.

### 6.3.2     Molecular Simulations of Mixed-electrolyte Swelling Clays

The assumption of thermodynamic ideality, particularly for the water adsorption reactions, is inadequate (Vidal and Dubacq 2009). To accurately model the thermodynamics of clay swelling in a mixed electrolyte, it is necessary to constrain the free energies of clay systems *in aqua*. A molecular simulation study is designed to calculate the per molar free energies and excess free energies of mixing of swelling/collapse reactions driven by ion exchange in saturated clay materials. In particular, these simulations are designed to allow us to simultaneously calculate selectivity coefficients for each swelling state and excess free energies of mixing of mixed swelling states, in order to relax the assumption of ideality that is currently imposed. To this end, our models consist of four layers of a swelling clay mineral, while the relative concentrations of cations in the bulk fluid are varied, subject to the constraint $[Na^+] + [K^+] = 1$ M. We also generate some cases with coexisting interlayer states (2W and 3W hydrates) for each of these mixed-electrolyte concentrations to evaluate the free energies of mixing.

### *6.3.2.1     Simulation Study Design*

The test case models are generated by varying electrolyte concentrations, and by varying the proportion of 2W-3W hydrates with 2W and 3W as end-members, yielding a total of 25 combinations. By calculating the basal spacing, excess free energy of mixing of swelling states, and the selectivity coefficient for each phase, the evolution of disjoining pressure and fraction of a phase (certain *n*-layer hydrate) will be acquired for given water activity and electrolyte composition. This study will be a valuable extension to our current understanding of phase changes in single electrolyte solution (Honorio et al. 2017), and

provide us insights into the links between ion exchange/adsorption (molecular phenomenon) and macroscopic clay mechanics.

### 6.3.2.2    Simulation Configuration

Figure 6-6 illustrates a molecular model of a pure 2W hydrate in 1M NaCl solution ($[K^+] = 0$). Each clay layer consists of 37 unit cells with a structural charge of −0.57 per $O_{20}(OH)_4$; the edges of the clay layer along the *y*-dimension are periodically replicated (therefore, requiring no termination) and the edges along the *x*-dimension are terminated with H, OH, $OH_2$. The size of the simulation volume ensures that layers do not interact across edges. The initial basal spacings are set to be near-optimal values based on reported values in literature for tv clays.
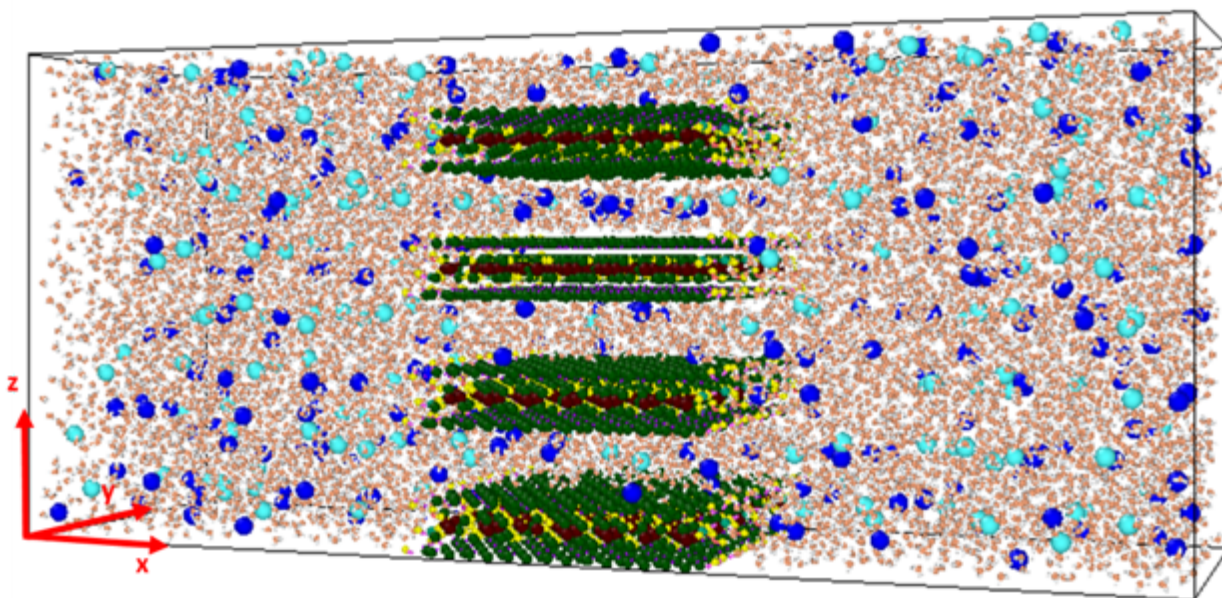


NOTE:    Green atoms = clay oxygens, yellow = clay hydrogens, dark red = clay aluminum, pink = water oxygens, blue = sodium ions, cyan = chloride ions.

**Figure 6-6.  Simulation system with 4 MMT layers in 1M NaCl solution**

The system is subsequently equilibrated in the NVT (T = 300 K) ensemble for 1 ns and subsequently, in the NPT (P = 1 atm, T = 300 K) for 5 ns to allow for the relaxation of the clay hydrate and the diffusion of water and ions. This also allows the clay hydrates to interact with the surrounding bulk fluid and establish equilibrium basal spacings corresponding to the activity of water. We use these simulations, first in the homoionic electrolyte configuration to study swelling free energies and excess free energy of mixing of mixed 2W/3W phases. The swelling reaction in homoionic electrolyte is characterized by

$$MMT3 \iff MMT2 + nH_2O \ (l) \qquad\qquad Equation\ 6\text{-}2$$
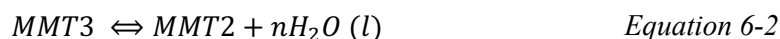
where *n* corresponds to the number of water molecules per unit-cell for a given electrolyte type and composition. We find in Section 6.2.1.2 that this number is 5 for NaMMT and 4.95 for KMMT. The per molar swelling energy for this phase transformation can be written in terms of the per molar free energy

of the end-members and the chemical potential of water, as shown in Equation 6-3. The chemical potential of water is obtained from NPT (300 K, 1 atm) simulations of pure water. At a density of 1.01 g/cc, consistent with our bulk solution density in Figure 6-6, we calculate the chemical potential of water to be −48.9 kJ/mol.

$$\Delta \bar{G}_{swelling} = \bar{G}_{NaMMT2} - \bar{G}_{NaMMT3} + 5\mu_w \qquad \qquad Equation\ 6\text{-}3$$

Obtaining the per molar free energies of the clay end-members ($\bar{G}_{NaMMT2}$ and $\bar{G}_{NaMMT3}$) requires the separation of energy contributions from the clay and the solution phase. Since the concentration and density of the bulk solution are kept constant for various pure and mixed hydrate phases (single electrolyte case), we confirm that the per molar free energy of the solution ($\bar{G}_{soln}$) remains the same (see Table 6-1). The number of clay layers also stay consistent ($n_{MMT}$ is constant), however, the variation in the overall size of the system leads to differences in $n_{soln}$ in Equation 6-4. We also calculate the average basal spacings of the hydrates over the course of the equilibration.

$$G_{system} = n_{soln}\bar{G}_{soln} + n_{MMT}\bar{G}_{MMT}$$

$$\bar{G}_{MMT} = \frac{G_{system} - n_{soln}\bar{G}_{soln}}{n_{MMT}} \qquad \qquad Equation\ 6\text{-}4$$

**Table 6-1.  Calculated basal spacings of hydrates, concentration, and per molar free energy of bulk solution from simulations**

| Hydrate | Bulk NaCl Concentration (mol/dm³) | $\bar{G}_{soln}$ (kJ/mol) | $d_{001}$ ($MMT2, MMT3$) (Å) |
|---|---|---|---|
| MMT2 | 0.97 | $-62.82 \pm 0.55$ | $(15.95 \pm 0.06, N/A)$ |
| 75% MMT2 – 25% MMT3 | 1.06 | $-60.96 \pm 0.11$ | $(15.99 \pm 0.02, 19.00 \pm 0.02)$ |
| 50% MMT2 – 50% MMT3 | 0.96 | $-61.71 \pm 0.12$ | $(16.26 \pm 0.03, 18.84 \pm 0.02)$ |
| 25% MMT2 – 75% MMT3 | 0.96 | $-60.40 \pm 0.53$ | $(16.34 \pm 0.06; 18.98 \pm 0.04)$ |
| MMT3 | 0.98 | $-60.75 \pm 0.33$ | $(N/A, 18.94 \pm 0.03)$ |

The change in equilibrium basal spacings between the pure and mixed states indicate the presence of strains when hydrates exist in mixed states. MMT2 hydrate exhibits tensile strain (tendency to swell) as its composition decreases in the mixed phases, whereas MMT3 exhibits a slighter tendency towards compression in the basal spacing in its mixed states. This implies a higher energy penalty for the 2W hydrate to exist in its mixed state compared to the 3W hydrate.

### 6.3.3    Future Work

To complement this hypothesis, we will also study the free energy of mixing associated with these states using Equation 6-5, where N corresponds to the mole fraction of the 2W and 3W states in the mixed hydrate and $\bar{G}_{mixed}$ is the per-molar free energy of the mixed hydrate obtained from simulations.

$$\Delta\bar{G}_{mixing} = \bar{G}_{mixed} - (N_{MMT2}\bar{G}_{MMT2} + N_{MMT3}\bar{G}_{MMT3}) \qquad \textit{Equation 6-5}$$

Based on preliminary results, we observe non-ideal mixing between the 2W and 3W phases, with asymmetry in the excess free energy of mixing that indicates sub-regular solid solution behavior. We will determine the suitability sub-regular solution fit to be integrated into our thermodynamic model described above, and use these results to refine our thermodynamic model for clay microstructure and swelling pressure.

# 7.    TRANSMISSION X-RAY MICROSCOPE FOR IN-SITU NANOTOMOGRAPHY OF BENTONITE AND SHALE

## 7.1    Introduction

x-ray imaging, in particular x-ray computed tomography (XCT), can provide detailed three-dimensional (3D) structural information of complex materials including fluid-saturated rocks. Synchrotron x-ray sources provide high brightness and tightly collimated sources of x-rays and thus enable XCT to be performed with substantially higher signal-to-noise than conventional laboratory sources. Moreover, the high brightness enables time-lapse observations of the dynamic evolution of stressed and/or reacting rock-fluid systems. Researchers in the Energy Geoscience Division at LBNL have established a major program at beamline 8.3.2 of the Advanced Light Source (ALS) using synchrotron-radiation based XCT to study processes relevant to DOE subsurface energy applications including to date geologic carbon sequestration and fossil fuel extraction (Voltolini et al. 2017). That program developed specialized environmental cells for the study of rocks-fluid processes at elevated temperature, hydrostatic pressure and uniaxial stress. The approach recently contributed to the FEBEX study of the stability of engineered barriers, contributing to the conclusion that variation in barrier properties exceeds the effect of heating at the analyzed locations. The best spatial resolution attainable at this beamline is approximately 600 nm, achievable for ~1-mm diameter samples, which is too coarse for studying clay associated structures in bentonites and shales.

TXMs use specialized x-ray optics including a zone plate (ZP) lens to achieve higher resolution imaging, currently approaching ~40 nm for samples less than 200 μm. Initially, TXMs were applied to the static imaging of polymers, Earth and biological samples at soft-x-ray energies (< 1 keV), but later studies showed the potential of higher-energy x-ray TXM for the study of dynamic processes in composite engineered and natural materials (Meirer et al. 2011; Nelson et al. 2012). TXMs at US synchrotrons (Andrews et al. 2010; Yin et al. 2006) have become popular imaging tools for materials and environmental sciences but such facilities cannot provide access over timescales (e.g., from hourly to monthly) required to track the long-term evolution of barriers and rocks under conditions relevant to subsurface storage of nuclear waste. Recently, the experimental program at ALS beamline 11.3.1 was relocated, providing an opportunity to develop—in partnership with the ALS—a TXM at a fraction of the cost of a completely new beamline or a commercial nanotomography instrument.

The goals of this project are to construct a new TXM at the ALS that will be primarily dedicated to energy geoscience studies for a 2-year period, and to use the imaging capabilities to study clay-rich barriers and rocks that are under consideration for underground storage of spent fuel and nuclear waste.

Descriptions of the ALS beamline and the TXM design are given in Sections 5.2 – 5.4 of Zheng et al. (2019). A conceptual model of the uniaxial stress-strain cell is given in Section 5.5 of Zheng et al. (2019). Here we provide progress reports and a revised project schedule.

## 7.2    Progress Report on TXM Commissioning

The construction of the TXM has proceeded rapidly following the hire of postdoctoral scholar Dr. Michael Nichols, co-funded by the ALS and Prof. Mike Czabaj (University of Utah). Working under the supervision of ALS Senior Engineer Alastair MacDowell, and co-supervised by Drs. Czabaj and Gilbert, Dr. Nichols has achieved the key commissioning goals on the agreed schedule. Delays totaling about two weeks have arisen due to late delivery of key components and due to challenges in scheduling ALS engineering work.

### 7.2.1    Microscope Design and Construction

The optomechanical components of the microscope have been designed, purchased or machined and fully assembled inside the hutch (Figure 7-1), with the exception of the Zone Plate that is anticipated to be received from Applied Nanotools by October 4th. Hardware integration with LabView control software has been completed for all plug and play components and the camera/detector system. Cable termination and software integration for stage and objective control is outstanding. A separate data analysis computer with 512 GB of central processing unit (CPU) memory and 24 GB of graphics processing unit (GPU) memory for the reconstruction, visualization and analysis of large 3D data sets has been ordered.
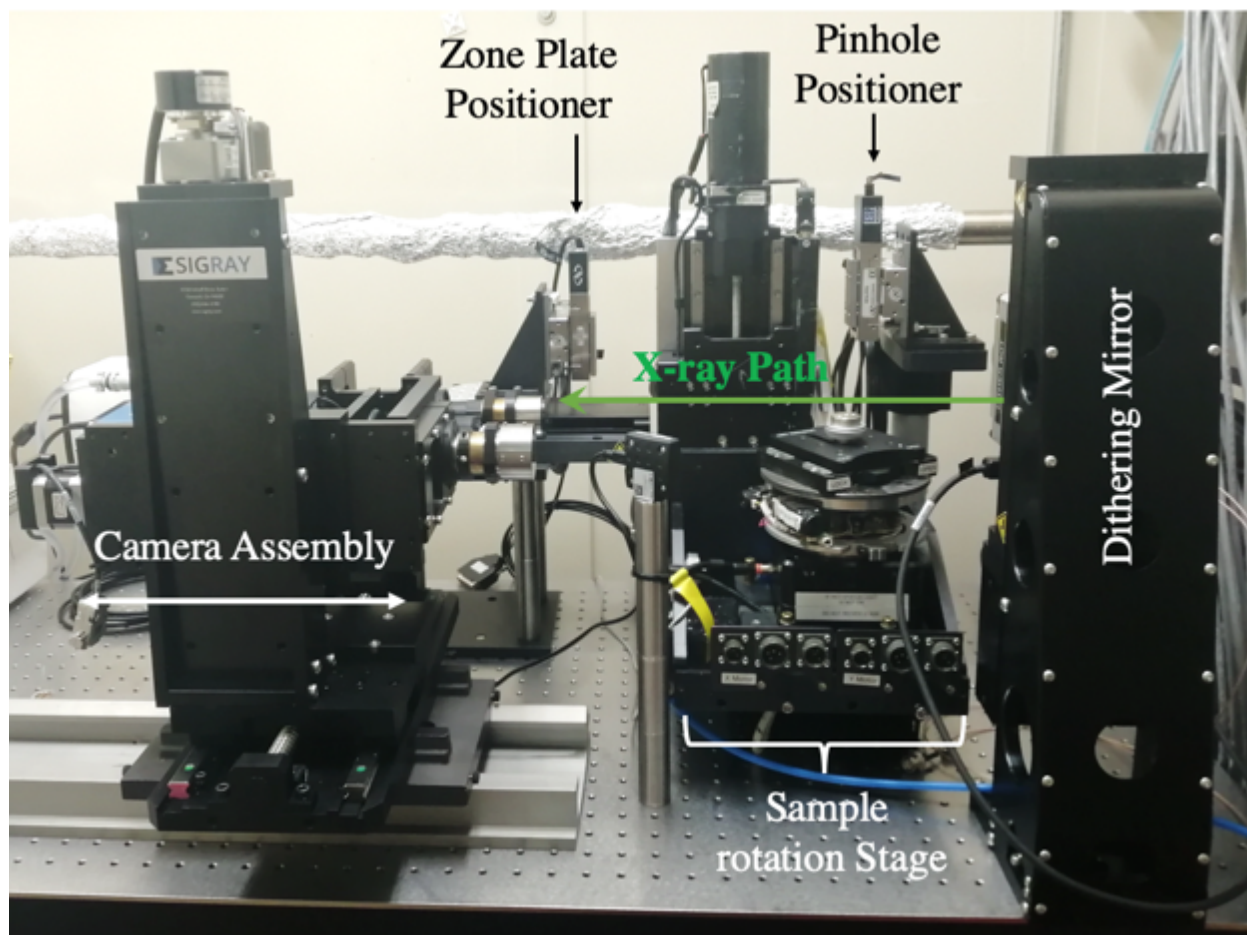


**Figure 7-1.  Photograph of the TXM components assembled in the experimental hutch of beamline 11.3.1 of the ALS**

### 7.2.2    Beamline Operations and X-ray Safety

X-ray safety is a priority and we have collaborated with the ALS on all the reviews necessary to open the beamline shutter and receive x-ray beam in the hutch. All operational 11.3.1 beamline controls behind the shield wall have been tested. Relevant radiation safety compliance procedures are expected to be completed by the publication date of this report, which is required before the final beamline review can be scheduled. The x-ray can be used only after a successful review.

Seismic safety is essential aspect of research in a tectonically active region. The zanite vibration damping block and custom breadboard have been secured in the hutch and all compliance procedures have been completed including anchorage, pull tests, etc.

### 7.2.3    Additional Work and Revised Schedule

The major activities for microscope analysis and commissioning are as follows:

- Activities required for x-ray operations

  - Complete and present the abbreviated ALS Beamline Design Review
  - Schedule and perform ALS Beamtime Design Walk-Through

- Activities required for TXM commissioning

  - Receive and install Zone Plate
  - Vibrational analysis of zanite table and microscope
  - Optical analysis of the beam at each individual microscope component

X-ray operations were scheduled to commence in early FY20 with TXM commissioning was to proceed over the next 4 weeks. The experimental emphasis was expected to rapidly transition from characterizing the imaging performance of the instrument using calibration standards to performing initial studies of clay and shale samples under ambient conditions. The first in-situ studies were expected at 6 weeks following x-ray operation.

## 7.3    Progress Report on Uniaxial Stress-Strain Cell

Postdoctoral scholar Dr. Harrison Lisabeth has led the design and construction of the novel miniature stress-strain cell that will be used for in-situ nanotomography studies of the mechanical deformation of bentonite and shale samples. The goal of this sub-project is to construct a cylindrical sample cell compatible with the TXM that allows pore-, grain- and smectite particle-resolved imaging of the swelling and restructuring of bentonite and the deformation and re-sealing of shale.

### 7.3.1    Uniaxial Stress-Strain Cell Construction

The designs for the stress-strain cell system have been finalized and all components ordered. Most components have been delivered and the system is being assembled. As described in the conceptual diagram in Figure 5.6 of Zheng et al. (2019), samples will be contained within an x-ray transparent Kapton cylinder and mechanically compressed between two opposed stainless-steel pistons. Strain will be measured by strain gages on the piezo stack and force will be measured by a custom load cell affixed to the stage. The control system can use either stress or strain as a feedback for constant stress or constant strain rate experiments. A unique feature of the miniature stress-strain cell is the creation of a sub-millimeter flow channel within both of the needle-shaped pistons that compress the sample.

Due to size constraints, we opted for a Physique Instrumente (PI) miniature piezo stage with 20-micron travel in the $x$-, $y$- and $z$-directions and with a nominal 0.2-nm resolution. The stage will be controlled by a PI E-727 controller with 100-kHz sampling rate and 20-kHz servo-control rate (Figure 7-2(a) and (b)). A crucial objective for the planned experiments is the ability to flow aqueous solutions of known composition through the sample. We successfully manufactured the uniaxial compression pistons with an off-axis flow conduit in FY19 (Figure 7-2(c)).
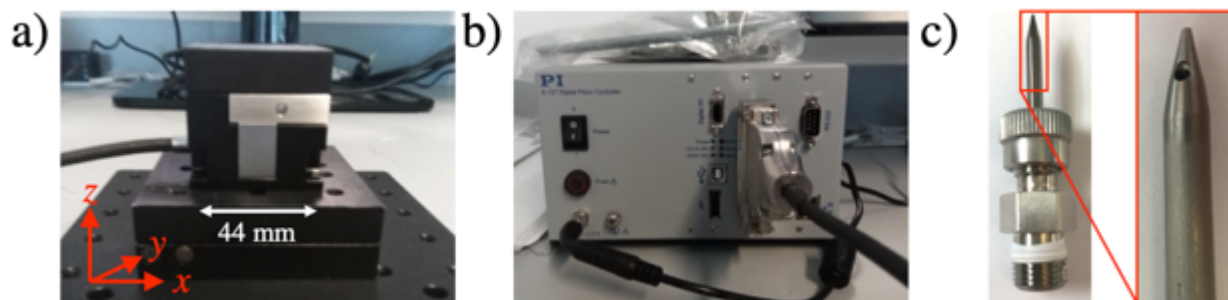
**Figure 7-2. Photographs of key components of the uniaxial stress-strain cell: (a) the *x,y,z* stage, (b) the controller, and (c) a compression piston with fluid flow hole**

### 7.3.2    Uniaxial Stress-Strain Cell Testing

Initial experiments are under development that will use an optical benchtop set up comprised of the loading system and a long working distance microscope coupled with a charge coupled device (CCD) camera (Figure 7-3). Initial experiments will involve compressing single mineral grains and grain-grain contacts to record stress-strain curves while imaging optically. These will be used to assess repeatability of data as well as to streamline sample selection and preparation techniques before the nanotomography system is functional.



**Figure 7-3. Benchtop experiment set-up with display showing a single quartz grain, ~200 microns in diameter, on top of the sample holder**

# 8. IN-SITU ELECTORCHEMICAL TESTING OF URANIUM DIOXIDE UNDER ANOXIC CONDITIONS

## 8.1 Introduction

In a reducing or anoxic environment, the oxidation of uranium dioxide ($UO_2$) SNF can only occur from the production of oxidants from the radiolysis of contacting water in the EBS of the geologic repository. Within the SFWST program, a model that captures the role of oxidant production is termed the Radiolysis Model (RM). The EBS environment, however, is expected to limit oxidation through the production of $H_2$ gas from anoxic corrosion of iron. These processes have been described in a Mixed Potential Model (MPM) or Fuel Matrix Dissolution Model (FMDM) by modeling the corrosion rate of spent fuel combining the RM submodel with an electrochemical corrosion model (Buck and Wittman 2014; Jerden et al. 2015). Other components contained in the EBS may result in the occurrence of more complex processes (Caporuscio et al. 2017).

Previously, experimental techniques for validation of the corrosion model under oxidizing conditions have used flow through experiments but these would be inadequate to describe the processes that might occur under anoxic conditions. To validate the FMDM, it is necessary to obtain measurements of the values predicted by the model, namely, the electrochemical corrosion potential. Besides using macroscale approaches to study the multiphase chemistry, it is important to probe the interfacial phenomena at the solid-liquid interface directly using novel chemical imaging approaches. Of particular relevance to the new approach presented in this report, a commercial in-situ liquid cell was recently used to study the electron beam induced radiolysis of $UO_2$ particles in solution (Buck et al. 2018) and the dissolution of boehmite (Conroy et al. 2017). A vacuum compatible and transferrable microfluidic reactor, namely the SALVI device, was invented at the PNNL and it has enabled in-situ liquid SEM (Yang et al. 2011a; Yang et al. 2014) and in-situ liquid ToF-SIMS (Yang et al. 2011a; Yu et al. 2017). Compared to the existing wet cell SEM approaches, (Thiberge et al. 2004; Nishiyama et al. 2010), the liquid surface is probed directly by the primary electron beam, because the microfluidic cell is partially open to vacuum with micrometer-sized apertures. In addition, the beam effect and memory effect can be minimized by flowing the liquid (Yang et al. 2011a; Yang et al. 2014). This technique has provided an unique in-situ chemical mapping approach for investigating challenging solid-liquid, air-liquid, and liquid-liquid interfaces, as illustrated by Ding et al. (2016), Sui et al. (2017), and Yu et al. (2018). This multimodal imaging tool could also be used to study materials relevant to geological disposal where we are interested in several complex interfacial processes. We started studies with two model systems, $UO_2$ and iron oxide ($Fe_3O_4$) in water to demonstrate feasibility and to develop the capabilities to perform this for spent fuel. These two systems also represent the major chemical components described in the FMDM for the EBS.

### 8.1.1 The SALVI Cell

The vacuum-compatible, microfluidic device, termed SALVI was developed at PNNL by Yu and co-workers (Yang et al. 2011b; Yu et al. 2011; Yu et al. 2013). The design details have been provided in many other papers and a version of SALVI is now available commercially as the Wet Cell II Liquid Probe System marketed by Structure Probe, Inc. (West Chester, PA). A polydimethylsiloxane (PDMS) block with a 100–500 μm wide by 300 μm deep channel was bonded with a 50 nm thick silicon nitride (SiN) membrane after oxygen plasma treatment. Approximately 10 μL of the analyte liquid mixture was injected into SALVI via its polytetrafluoroethylene tubing and sealed by polyether ether ketone union afterwards. A photo of a SALVI device is shown in Figure 8-1(a). Figure 8-1(b) shows the SALVI device installed in the SEM stage prior to in-situ liquid SEM analysis. Figure 8-1(c) shows the port on the SEM instrument where the electrochemical workstation feedthrough is installed. Figure 8-1(d) depicts the SALVI device mounted on the ToF-SIMS stage prior to shuttling into the main chamber. Figure 8-1(e) depicts the relative location of the main chamber and where the SALVI is located during analysis (Yu et al. 2019b).
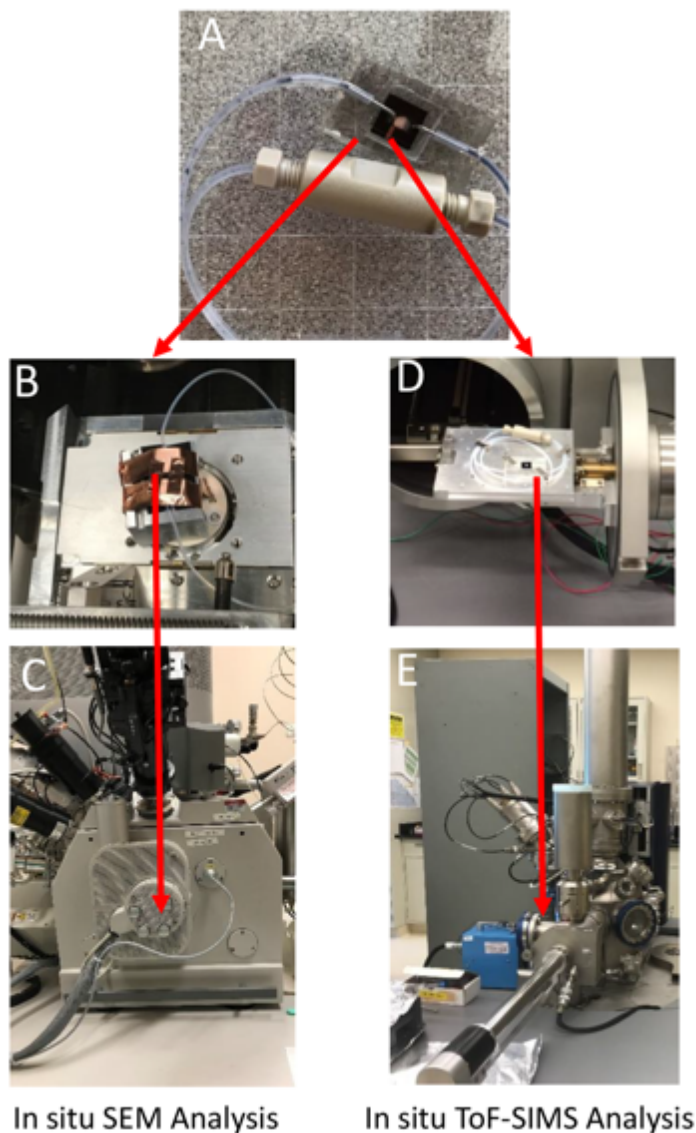
**Figure 8-1. (a) Vacuum-compatible SALVI device, (b) SALVI installed on SEM stage in Quanta SEM (c) Quanta SEM, (d) SALVI installed on ToF-SIMS stage before loading to the loadlock in the IONTOF ToF-SIMS V instrument, and (e) IONTOF ToF-SIMS V instrument**

## 8.2    Experimental Setup

This section describes the experimental setup for the in-situ testing.  We describe the effort in the micrometer scale $UO_2$ electrode fabrication first. Then we follow with more details concerning in-situ liquid ToF-SIMS and in-situ liquid SEM setups.

### 8.2.1    Adapting UO₂ as a Working Electrode in the SALVI E-cell

This section describes the development of the electrode and the next steps needed for the fabrication of the micrometer gold electrode.

### 8.2.1.1    Development of the Electrode

One of the key developments required to study $UO_2$ electrochemistry in-operando is to integrate $UO_2$ as the working electrode (WE) in the SALVI E-cell. We started by using gold (Au) WE sputter coated on a SiN membrane as a conductive layer and substrate for the $UO_2$ to attach to. The source of $UO_2$ is from the environmental barrier. The dimension of the source $UO_2$ material is rather large for microanalysis using the microfluidic cell. The microfluidic cell requires that the WE be in the tens of micrometer scale. The maximal size of $UO_2$ is estimated to be approximately 10 to 20 μm. We selected microfabrication processes based on following three principles: (1) the footprint dimension should be around a 1:1 ratio of the target $UO_2$ WE which is ~ 10 × 10 μm and no more than 20 × 20 μm; (2) microfabrication methods are required for the precision required by the $UO_2$ electrode size in tens of micrometers; and (3) the performance of the $UO_2$ WE should be verified and compared against bulk experiments. The reference electrode (RE) and counter electrode (CE) is the same as our existing E-cell devices using other materials. Platinum (Pt) is used for both the RE and CE. A slight potential shift is expected when using Pt as RE compared to bulk experiments as demonstrated in previous experiments. However, this slight device performance difference does not affect the investigation of the electrochemistry (Liu et al. 2014; Yu et al. 2016).

The dimensions of the $UO_2$ WE are estimated to be approximately 10 × 10 μm and less than 20 × 20 μm. In order to minimize interference from the Au substrate that can also function as a WE when potential is applied, the Au substrate should be just slightly bigger or almost the same size as the $UO_2$ lift-out. The Au substrate film is fabricated on the SiN membrane (Figure 8-2). The Au substrate is designed to be in the center of the SiN membrane with a dimension of 0.5 × 0.5 mm, and the electric connection structure with a dimension of ~ 500 × 2 mm is placed on the edge of the SiN window (Figure 8-2) for the external wire connection.
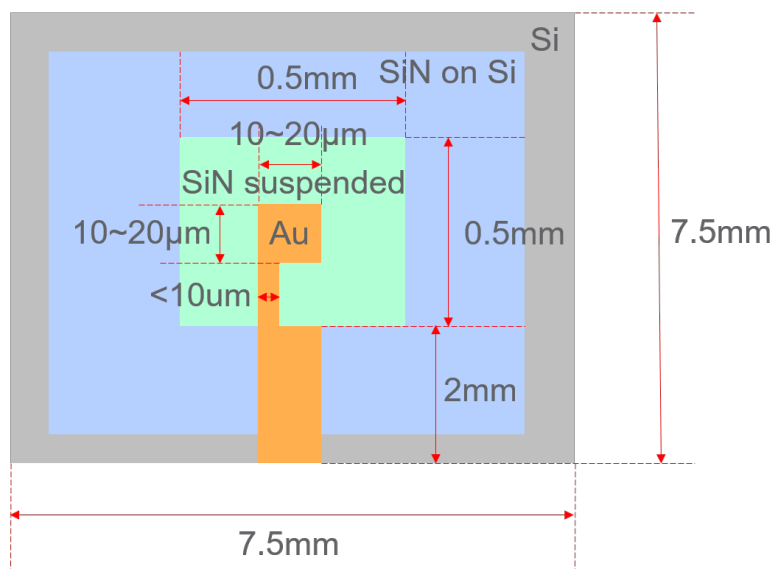


**Figure 8-2.  Schematic of gold substrate on SiN membrane window**

Since the Au substrate requires micrometer-level precision, we utilized microfabrication processes including shadow masking and photolithography. To test feasibility, we first made several Cr structure prototypes by shadow masking to mimic the effect prior to using Au. The shadow mask was fabricated by photolithography dry etching (deep reactive ion etching (DRIE), Oxford-100) and wet etching (KOH). A

fabricated shadow mask had several electrode-shape holes. Individual SiN chips could be attached to one side of the shadow mask before sputtering the metal layer (Denton sputter coater) resulting in an electric conductive substrate layer with the desired features once the mask was removed.

We first tested $400 \times 400$ μm and $500 \times 500$ μm features with the shadow mask method. With the combination of photolithography dry etching and wet etching, we successfully fabricated a shadow mask containing $400 \times 400$ μm and $500 \times 500$ μm features. Several tested Cr features were sputter coated on the SiN chips shown in Figure 8-3. Completed Cr test features showed improved features, yielding a more than 75% size reduction of the footprint (i.e., from $2 \times 2$ mm to $\sim 450 \times 450$ μm). This shows the possibility of improvement for making smaller gold electrode substrates.
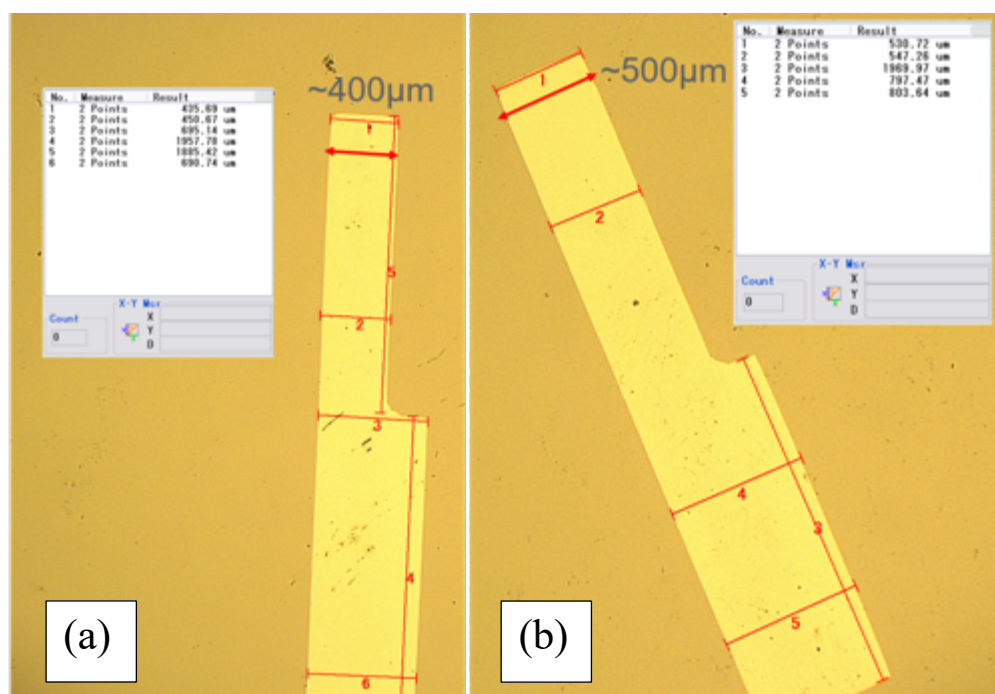


**Figure 8-3.  Microelectrode features using shadow masking:**
**(a) ~400 × 400 μm and (b) ~500 × 500 μm**

We then attempted to achieve a $15 \times 15$ μm feature with the shadow masking technique. However, because the actual etching aspect ratio was not close to 1:10 throughout the whole feature, it was challenging to obtain fine features using wafer DRIE at the micrometer level within the 300-μm thick wafer. The etched depth of $15 \times 15$ μm was shallower than the 500 μm $\times$ 2 mm feature used for wire connection, which was caused by the uneven etching rate. Therefore, we were not able to achieve the $15 \times 15$ μm feature goal using the shadow mask.

### 8.2.1.2    *Next Step for the Fabrication of the Micrometer Gold Electrode*

Since the shadow mask method was not successful for making $\sim 15 \times 15$ μm features, we plan to apply other microfabrication approaches. Specifically, we will use photolithography to make features directly on premade SiN chips. Figure 8-4 gives a simple illustration of the etching steps to achieve the finer micrometer scale features needed to incorporate the $UO_2$ WE in the microfluidic E-cell. A layer of platinum will be sputtered as an adhesive layer for the gold layer of ~20-nm thick. Afterwards, the gold layer will be sputtered on the top the Ti layer for ~40 nm. After sputtering, both metal layers will be

etched by a wet etching process as depicted in Figure 8-4. In order to protect the SiN membrane, a layer of photoresist can be used as a protective layer during wet etching of the Au and Ti layers. After completion of the fabrication process, the microlevel electrode will be tested by assembling it as the WE using the existing E-cell design.
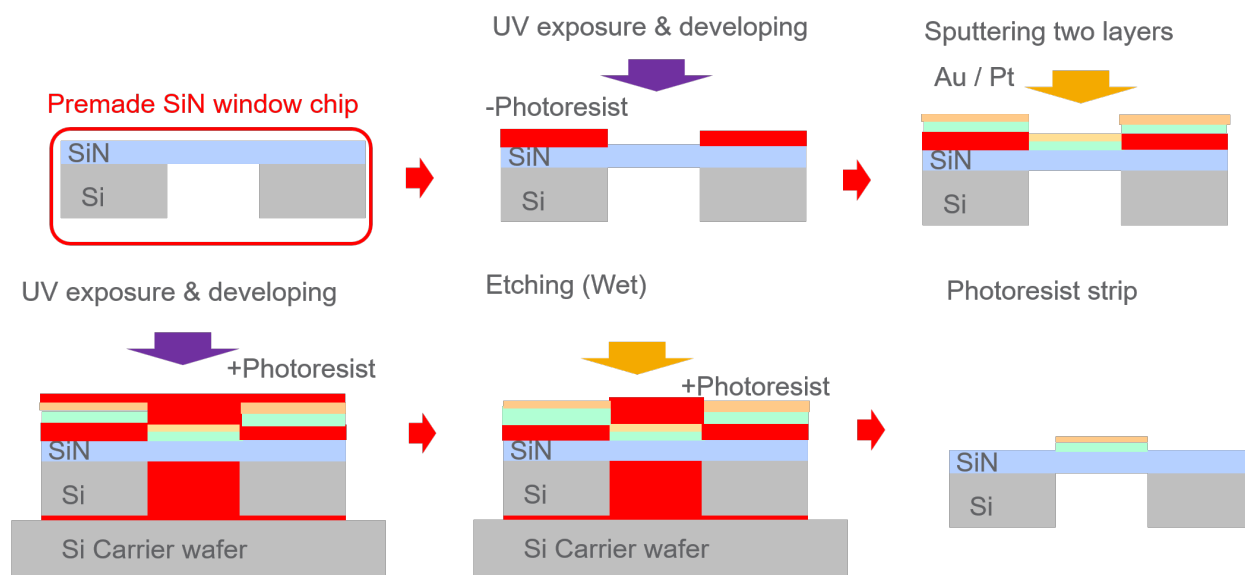


**Figure 8-4.  Schematic showing electrode fabrication
using wet etching on a SiN membrane window**

## 8.2.2     In-situ Liquid ToF-SIMS

A TOF-SIMS V spectrometer (IONTOF GmbH, Münster, Germany) was used in this work. The pressure in the main vacuum chamber was maintained below $4 \times 10^{-7}$ Torr (Yang et al. 2011b). The SiN window was cleaned by a 1 keV $O_2^+$ beam to remove surface contamination with a scanning area of $500 \times 500$ μm$^2$ prior to analysis. An electron flood gun was used to compensate surface charging during analysis. A pulsed 25 keV $Bi_3^+$ primary ion beam was used with a current of ~0.36 pA. The focus spot was about 0.45 μm in diameter and the scan area was 2 μm in diameter. A pulse width of 150 ns was used to punch through the SiN membrane (Yu et al. 2016). The pulse width was changed to 50 ns to obtain a relatively higher mass resolution in the latter portion of the depth profile. More experimental details have been reported elsewhere (Zhou et al. 2016; Yu et al. 2017).

Figure 8-5 provides a close view of the SALVI mounted on the ToF-SIMS's sample holder (Figure 8-1(a)) and its microchannel being punched through by the $Bi_3^+$ion beam (Figure 8-1(b)). The microscope imaging was utilized to facilitate locating the analysis area on the SiN window that seals the microchannel. Five holes were drilled through on the SiN window, exposing the liquid sample beneath to the analysis beam. Subsequently, the secondary ions that carry the signature information of the sample were produced. Two samples were measured including 250-ppm uranium in uranium nitrate form dissolved in $HNO_3$ and laminin solution and a control sample containing $HNO_3$ and laminin only. SALVI is the critical component of in-situ liquid SIMS techniques, which enables the liquid samples to be measured directly at microscale. SALVI only requires a very minimal liquid sample volume, approximately 30 μL.
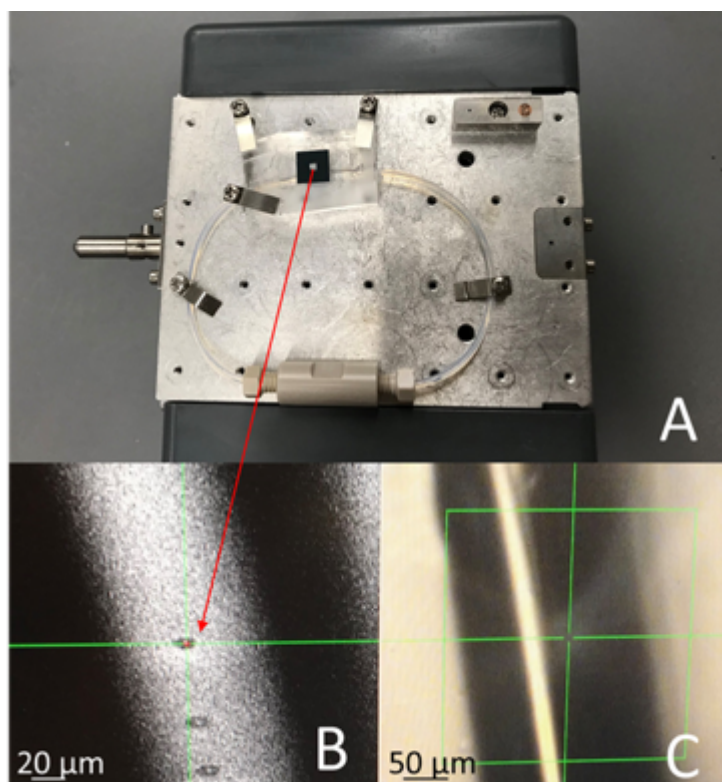
**Figure 8-5.  (a) Vacuum-compatible SALVI device mounted on sample holder before ToF-SIMS analysis, (b) secondary ion image of SALVI's microchannel being punched through by Bi$_3^+$ ion beam, and (c) SALVI's microchannel viewed under microscope for locating analysis area**

### 8.2.3    In-situ Liquid SEM using the Existing SALVI E-cell

Of particular interest to study the oxidation and reduction of UO$_2$, the electrochemical version or the E-cell (Liu et al. 2014; Yu et al. 2016) was used and adapted in this work. The feasibility of using SALVI for in-situ characterization of particles in liquid was demonstrated in our previous work (Yao et al. 2017; Yu et al. 2019a). This paper shows initial results of in-operando study of spent fuel relevant systems using the SALVI E-cell. Two FEI Quanta 3D focused ion beam-scanning electron microcope (FIB-SEM) instruments were used. Both low and high vacuum modes SEM were employed. The radiological material was analyzed in the Quanta 250 field emission gun (FEG) SEM housed in the Radiological Processing Laboratory (RPL) at PNNL. Non-radiological materials were analyzed to optimize imaging conditions. The iron oxide (Fe$_3$O$_4$) in deionized water mixture was analyzed in the Quanta SEM RPL. A standard operation procedure of in-situ liquid SEM was described previously (Yao et al. 2017; Yu et al. 2019a).

The goal of this work is to conduct in-operando SEM of UO$_2$, simulating spent fuel conditions. Figure 8-6(a) depicts the experimental setup including an electrochemical station connected with a SALVI E-cell. Figure 8-6(b) shows a series of cyclic voltammograms obtained with this setup using a standard solution consisting of 2 mM K$_3$Fe(CN)$_6$ and 1 M KNO$_3$ in deionized water. Reagents were acquired from Sigma-Aldrich. This initial result demonstrates the performance of the approach prior to using radiological materials. In-operando results and the application of in-situ SEM imaging in studying nuclear materials are presented.
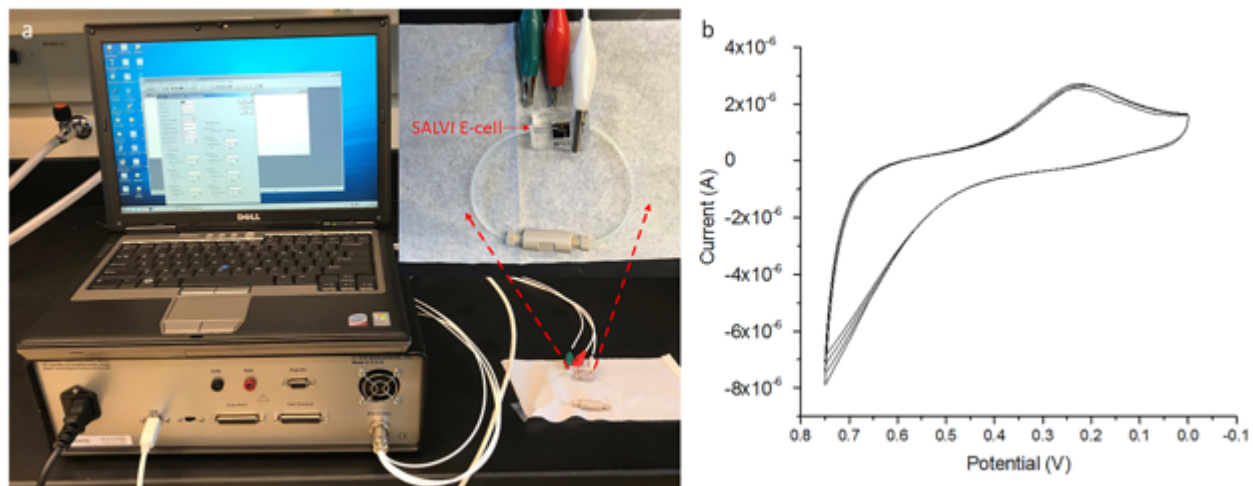
**Figure 8-6.  (a) In-operando SEM setup showing the SALVI E-cell (insert) connected with an electrochemical station, and (b) cyclic voltammograms acquired using this setup**

## 8.2.4    Electrochemistry Analysis of Liquid Sample containing Uranium

Next, we performed electrochemistry experiments using a uranium containing electrolyte in the SALVI E-cell. An EHI 660 E (CH Instruments, Inc., Austin, TX) electrochemical workstation was used. The E-cell was mounted on the sample stage of the Quanta 250 FEG SEM and was tested in the ambient condition. The three electrodes were connected to the electrochemical workstation via corresponding wires as shown in Figure 8-7. More results are shown in Section 8.3, which presents and discusses the experimental results.
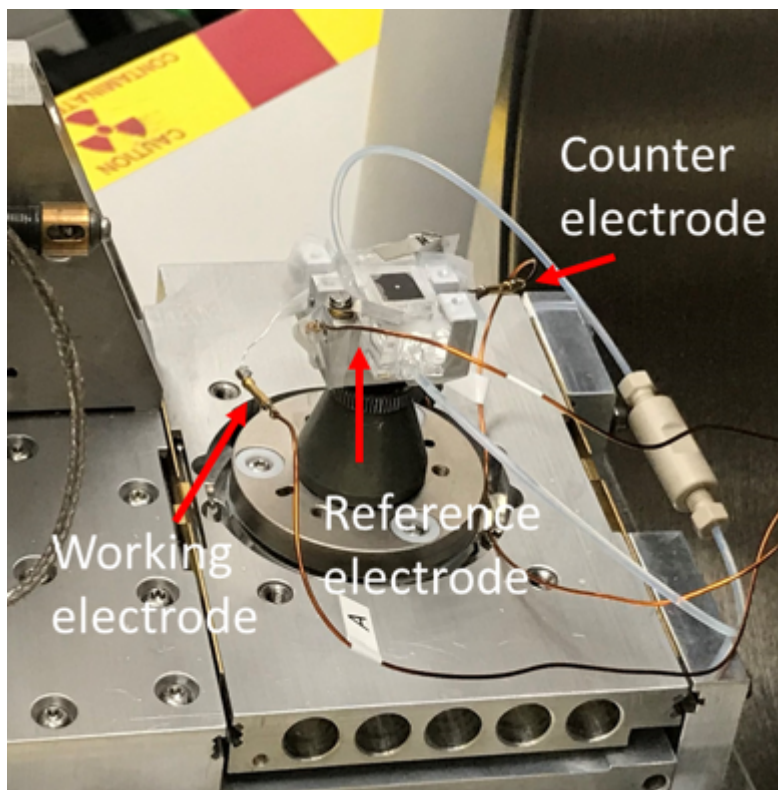
**Figure 8-7.  SALVI E-cell with uranium containing electrolyte in an ambient environment**

### 8.2.5    Multimodal analysis on Los Alamos National Laboratory's Corrosion Sample

A stainless-steel metal coupon was received from LANL and used to examine the unprocessed Wyoming bentonite and the clay-stainless-steel metal interface. Multiple analytical techniques including ToF-SIMS, scanning transmission electron microscopy–x-ray energy dispersive spectroscopy (STEM-EDS), transmission electron microscopy-electron energy loss spectrocopy (TEM-EELS), and scanning electron microscopy–x-ray energy dispersive spectroscopy (SEM-EDS) were used to examine the top surface and cross-sectional interface of the coupon.

In ToF-SIMS analysis, three analysis modes were conducted including high mass resolution mass spectrum, high spatial resolution imaging, and depth profiling. Data were acquired in both positive and negative ion modes. In the mass spectrum mode, 25-KeV $Bi_3^+$ was sputtered on the $100 \times 100$-m area, collecting the high mass resolution spectra for 60 scans with $128 \times 128$-pixel resolution. In the imaging mode, the same areas were analyzed for 200 scans with $256 \times 256$-pixel resolution. In the depth profiling mode, 25-KeV $Bi^+$ was applied as the primary analysis beam, coupled with 2-KeV $O_2$ as the sputter beam to analyze the sample surface layer by layer.

A cross-sectional mount of the metal sample was prepared by polishing to a 0.25-µm finish. The sample was then introduced into a FEI Helios 660 NanoLab™ FEG dual beam FIB-SEM equipped with an EDAX (EDAX Inc., Mahwah, NJ) compositional analysis system. The current and accelerating voltage of the ion beam used for prep was between 9 pA to 9 nA and 2–30 kV, respectively, depending on the progress of the thinning operation. The thinned specimens were attached to Cu-Omniprobe grids.

Lift-out specimens for STEM were characterized on a JEOL (Japan) ARM300F (GrandARM) probe-corrected microscope equipped with high angle annular dark field (HAADF) and bright field (BF) detectors, dual Bruker EDS, and Gatan (Gatan Inc., Pleasanton, California) Quantum Image Filter for electron energy-loss spectroscopy (EELS) and imaging. Diffraction patterns were collected on a Gatan 4D STEM system, and EELS data, and electron micrographs were analyzed with Gatan DigitalMicrograph™ 3.0.

## 8.2.6    Sample Preparation

Two types of sample preparation were described below. One was for liquid SIMS and liquid SEM and the other was for the stainless-steel coupon from LANL.

### 8.2.6.1    *Liquid Samples Analyzed using In-Situ Liquid SIMS*

A liquid solution containing uranium was prepared from U1010- uranyl nitrate (Crystal, ACS grade) and hexahydrate (Spectrum Chemical Mfg. Corp.). 250-ppm uranyl nitrate was dissolved in ~0.09-M $HNO_3$ and 1-mg/ml laminin (Sigma L2020-1MG) was added to make the testing mixture.

### 8.2.6.2    *Liquid Samples Analyzed using the Electrochemistry Workstation*

Two liquid samples loaded in SALVI E-cells were analyzed using the electrochemistry workstation, including 1-mM uranyl nitrate in 0.1-M $HNO_3$ and 0.1-M $HNO_3$ only as the control sample.

### 8.2.6.3    *LANL Metal Coupon Preparation*

The metal coupon received from LANL was unprocessed and non-radioactive. It was cut into smaller pieces for multimodal analysis using various analytical tools. One piece was fixed in epoxy with the cross-sectional interface exposed for analysis after polishing. This interface piece was analyzed using ToF-SIMS.

Figure 8-8(a) shows photos of the LANL metal coupon as received. Figure 8-8(b) gives pictures of the cross-sectional interface fixed in epoxy resin and one of the small pieces from various analyses. Figure 8-8(c) shows how the metal piece was loaded onto the ToF-SIMS stage prior to analysis.
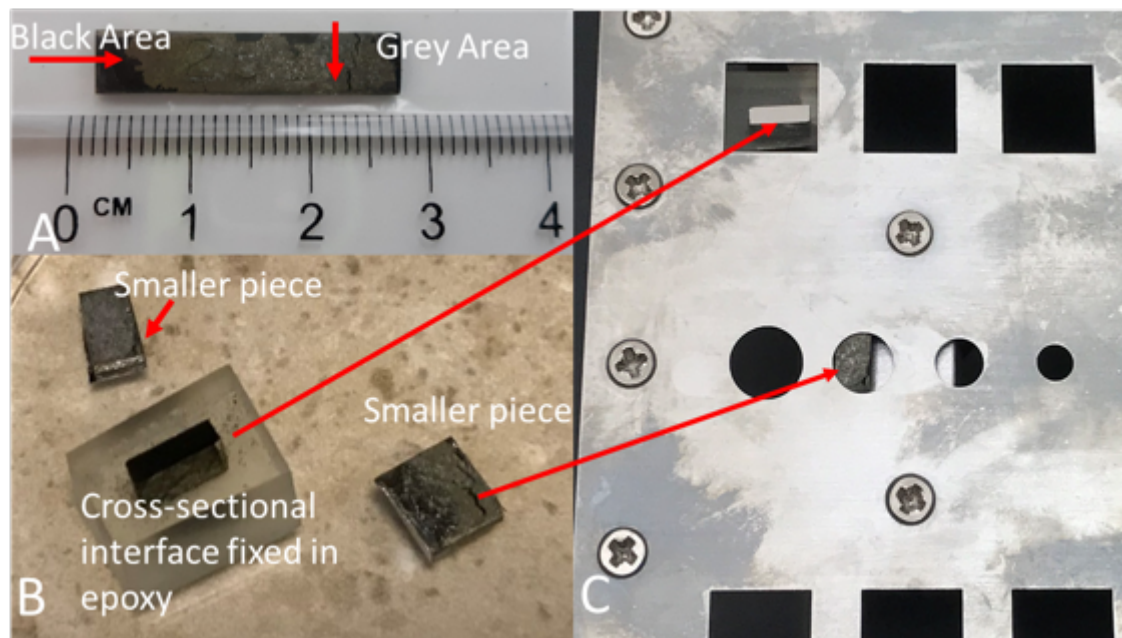
**Figure 8-8. (a) Complete metal coupon as received, (b) trimmed smaller pieces and a piece polished and fixed in the epoxy, and (c) sample coupons mounted in the ToF-SIMS sample holder**

## 8.3　Results and Discussions

In this section, we report results from three types of experiments. The first results are from in-situ liquid SIMS analysis of $UO_2$ containing liquid. The second results are from the in-situ liquid SEM experiment of uranium containing electrolyte. Lastly, the third results are from the multimodal imaging and analysis of the LANL metal coupon.

### 8.3.1　In-situ Liquid SIMS of $UO_2$

We conducted in-situ liquid SIMS analysis of a liquid mixture containing $UO_2$, $HNO_3$, and laminin. Although not directly related to the $UO_2$ spent fuel chemistry, laminin is added to demonstrate the ToF-SIMS capability to identify both organic components and uranium containing compounds. Besides this mixture, we analyzed $UO_2$ dissolved in nitric acid and nitric acid solution as the control.

The mass spectra acquired from these three liquid samples were normalized to the intensity of $NO_2^+$ before comparison as seen in Figure 8-9. The third sample, 3.5% $HNO_3$, was presented previously in our last report. The mass spectrum and 2D image from this sample were used for comparison purposes. The high intensities of laminin fragment peaks such as $C_4H_5N_2^+$, $C_5H_{10}N^+$, and $C_5H_{12}N^+$ were detected from both samples containing laminin (250 ppm U w/laminin and $HNO_3$ w/ laminin) but not from the $HNO_3$ sample as expected. Furthermore, $^{238}UO_2^+$ was only detected from the uranyl sample, even with the interference of organic species. The normalized 2D image comparisons are presented in Figure 8-10, confirming the detection of uranium species and organic molecules in the mixture consisting of 250 ppm U and laminin.

Our in-situ liquid SIMS results illustrate that we can use it to detect the changes of the $UO_2$ electrode before and after applying potentials to the electrode and examine the corrosion process of $UO_2$. It is envisioned that in-situ and in operando approaches will provide new insights into spent fuel chemistry of importance, simulating depository conditions and enhance our ability to manage and control nuclear materials at microscale.
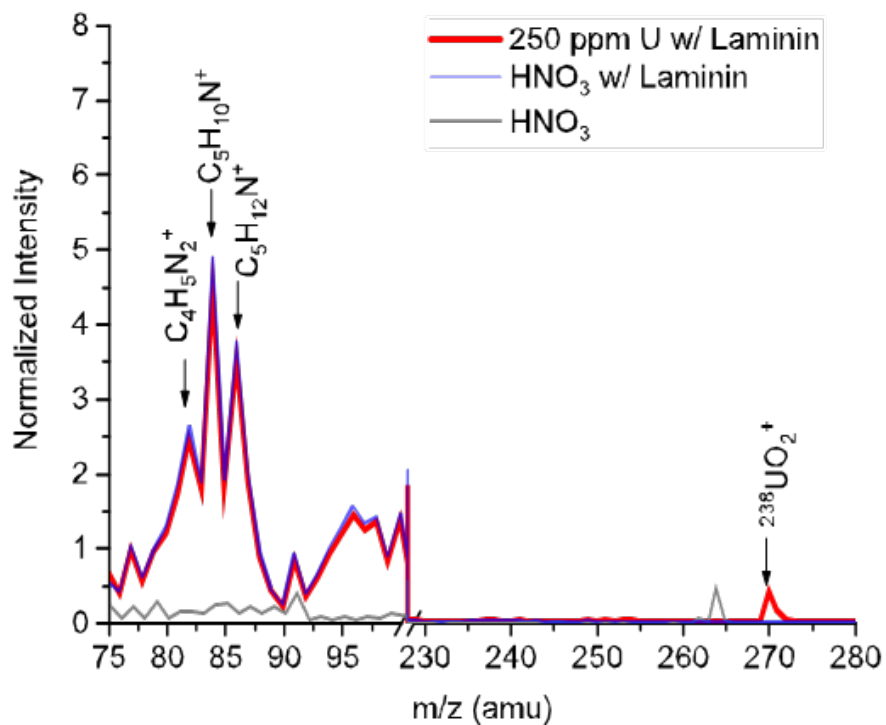
**Figure 8-9. Mass spectra comparison of liquid samples analyzed using liquid SIMS**
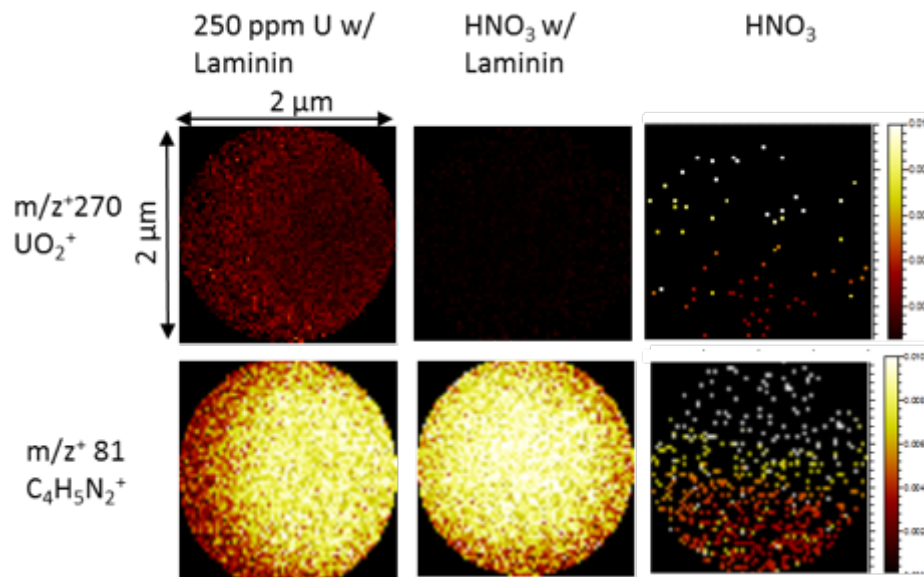


**Figure 8-10. Comparison of normalized 2D images of $UO_2^+$ and $C_4H_5N_2^+$ among three liquid samples**

### 8.3.2    Electrochemical Analysis of Uranyl Nitrate for In-situ SEM

The electrochemistry of U (VI) was conducted using a three-electrode SALVI E-cell, with gold film (~1 mm$^2$) as WE, Pt wires as CE and RE, respectively. The cyclic voltammagram of U (VI) nitrate dissolved in 0.1 M HNO$_3$ showed reduction and possible oxidation processes that were not existing in the control blank sample. The potential process at 0.22 V is assigned to $UO^+ \rightarrow U^{4+}$ reduction. The potential process at -0.21 V indicates possible reduction of $U^{4+} \rightarrow U^{3+}$, while the process at -0.1V possible oxidation of a low valence of U changing to a higher valence. (Figure 8-11). Since WE is gold, the potential of the reduction and oxidation of U may differ slightly from other published reports or databases using other WE materials (Liu et al. 2014; Yu et al. 2016). In addition, the reduction and oxidation processes that appear in both blank and uranyl nitrate solutions may be caused by the Au film, because the effective Au film area is much larger than the UO$_2$ WE. This result suggests that we use a wider range of potentials in future experiments. In addition, a smaller Au film conductive substrate is needed to reduce the interference of H and Au. Future testing will include the scanning rate dependency of the uranyl nitrate using this three-electrode cell with improved UO$_2$ WE design.



**Figure 8-11.  (a) Cyclic voltammagram of 0.1 M HNO₃ and (b) 1mM uranyl nitrate in 0.1 M HNO₃**

### 8.3.3    Multimodal Imaging of the LANL Metal Coupon

We received a sample of corroded metal from F. Caporuscio of LANL. This specimen was cut into sections for further testing and analysis. Extensive characterization by SEM and XRD has been reported by LANL on this specimen (Caporuscio et al. 2014). More details of specimen preparation were provided previously.

Figure 8-12 presents the positive mass spectrum detected from the interface of the metal coupon using the high mass resolution mode of ToF-SIMS. The possible identification of the detected peaks is listed in Table 8-1. Combined with 2D images (Figure 8-13) of the elemental and molecular information of the interface, our results show the main chemical components of clay, the clay-metal interface, and stainless steel. Elemental components such as $K^+$, $Ca^+$, and $Na^+$ from the water that treated the coupon were observed (Figure 8-10). The observation of $Si^+$ and $SiO^+$ (Figure 8-12) on the clay layer confirms silica (SiO$_2$) formation, which was observed using SEM in the earlier LANL report (Caporuscio et. al. 2014). It is interesting that $Fe^+$ and $Fe(OH)^+$ are present in both the stainless steel and clay layer, and the intensity of $Cr^+$ at the interface is stronger than that in the bulk stainless steel (Figure 8-13). This observation provides visualized evidence that Fe-saponite forms at the bentonite – steel interface via oxidative

leaching of Fe and Ni, producing a chromite $(Cr_{1.04}Fe_{0.96})(Fe_{0.69},Ni_{0.31})O_4$ passivation layer on the outer surface of the 316 stainless steel plates (Caporuscio et al. 2014). The ToF-SIMS spectral results demonstrate that SIMS has sufficient surface sensitivity to provide useful elemental information as SEM. More importantly, SIMS can provide high resolution 2D chemical maps showing the interfacial elemental and molecular distribution, offering mechanistic insights into the bentonite–steel interfacial processes.
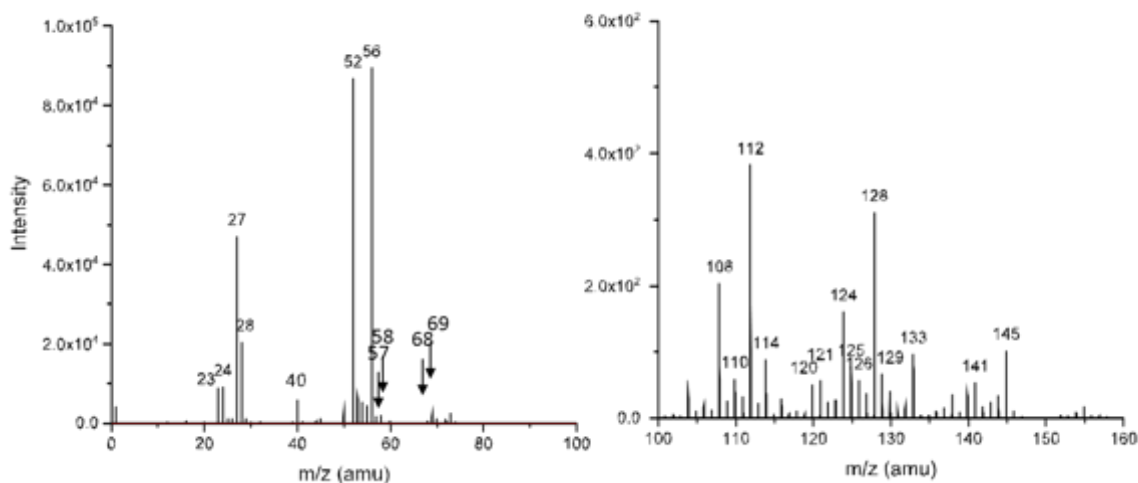


**Figure 8-12.  Positive ions detected from coupon interface fixed in epoxy**

**Table 8-1.  Peak identification of species detected from the corrosion interface**

| No. | Center Mass (u) | Possible Assignment | No. | Center Mass (u) | Possible Assignment |
|---|---|---|---|---|---|
| 1 | 22.99 | $Na^+$ | 8 | 57.94 | $Ni^+$ |
| 2 | 23.98 | $Mg^+$ | 9 | 67.94 | $CrO^+$ |
| 3 | 26.98 | $Al^+$ | 10 | 68.94 | $CrOH^+$ |
| 4 | 27.98 | $Si^+$ | 11 | 69.95 | $CrH_2O^+$ |
| 5 | 39.96 | $Ca^+$ | 12 | 111.88 | $Fe_2+$ |
| 6 | 51.94 | $Cr^+$ | 13 | 128.87 | $Fe_2OH^+$ |
| 7 | 55.94 | $Fe^+$ | 14 | 144.86 | $Fe_2O_2H^+$ |
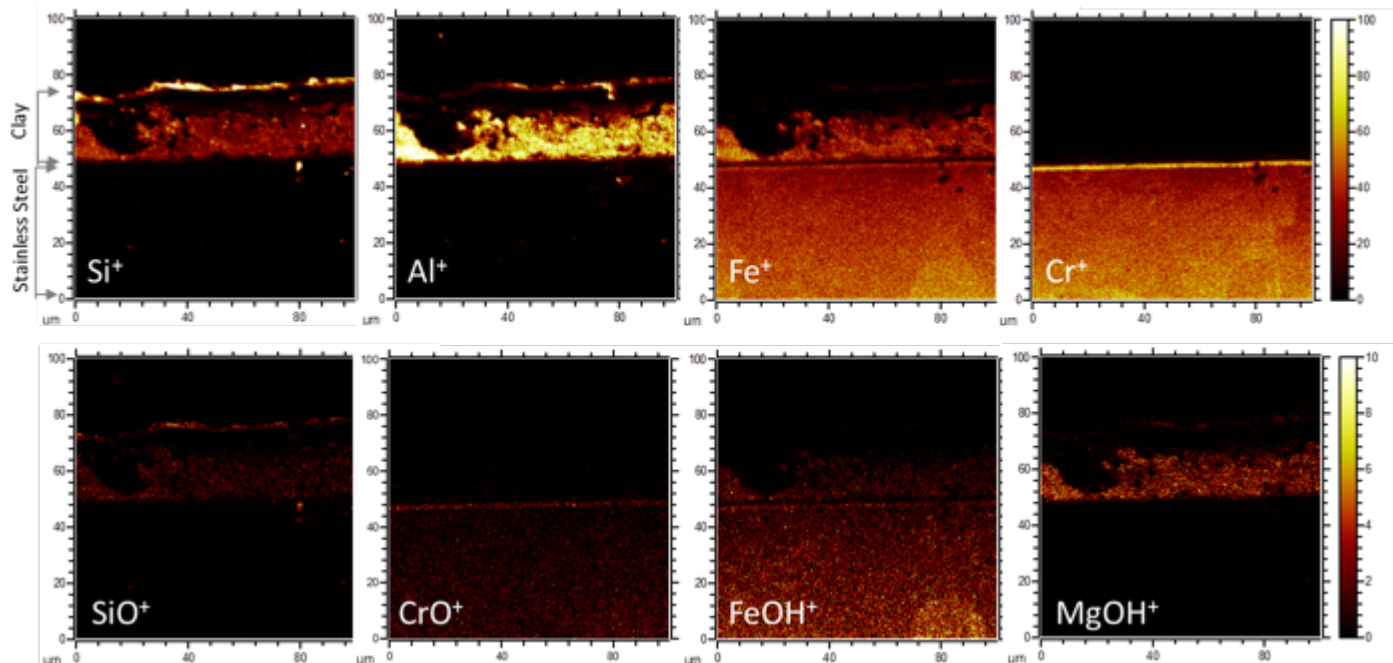
**Figure 8-13.  2D images resulting from SIMS imaging technique capture the distribution of the dominant elements and molecules on the clay, clay-interface, and stainless-steel surface**

In addition, we used the SIMS depth profiling capability to reveal the distribution of chemical species in 3D. SIMS depth profiling was applied to the top surface of one of the small pieces. The depth analysis is approximately ~ 800 nm. The chemical species detected are mainly from the clay layer (Figure 8-14).

Figure 8-15 gives two examples of the 3D SIMS analysis from the top surface region of the corroded metal, comparing the black and gray areas. Figure 8-15(a) shows superimposed 3D images of $Al^+$ and $Fe^+$ from the black area. Ion signals from metal are dominant in the black area. Figure 8-15(b) shows 3D images $Al^+$ and $Fe^+$ from the gray area. Charging causes lower ion intensities compared to the black area. We suspect that iron oxidization was formed on the surface in the gray area.

The 3D SIMS analysis demonstrates the capability of dynamic ToF-SIMS in providing the elemental and molecular information as a function of depth. The 3D visualization can be utilized to reveal the species present around the clay-metal interface, providing insights into the corrosion process at the bentonite–steel interface.
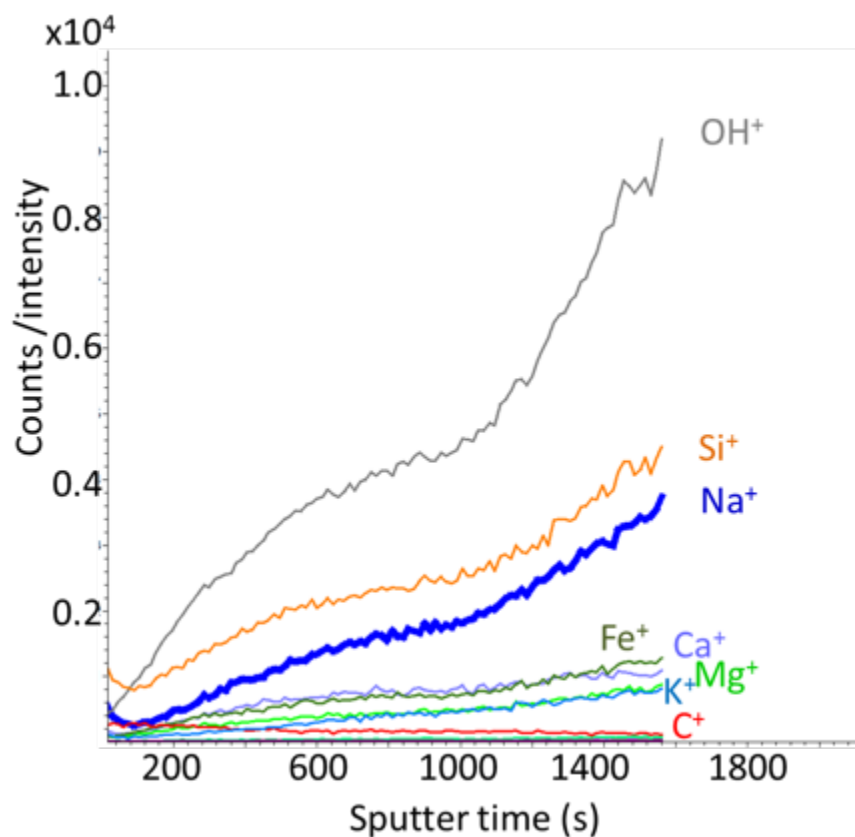
**Figure 8-14.  Depth profiling analysis of clay surface of the metal coupon**
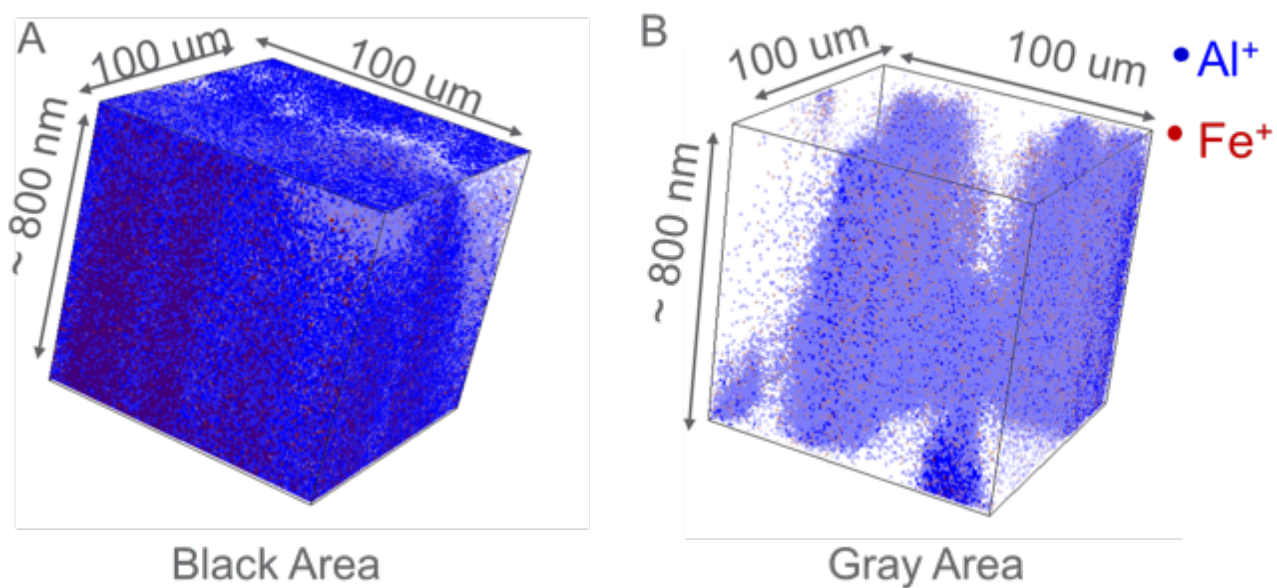


**Figure 8-15.  3D visualization of Al⁺ and Fe⁺ distributions from
(a) black area and (b) gray area in the stainless-steel coupon**

Extensive characterization by SEM and XRD has been reported by LANL on this specimen. STEM-EDS and -EELS work was used to understand the mechanism of metal corrosion. The EDS elemental maps show the distribution of elements and the separation of the clay layer from the corroded metal. This is also clearly visible in the STEM image. The clay consists of Na, Al, O, and Si as major components. Other minor elements are also identified but not shown in the figure.
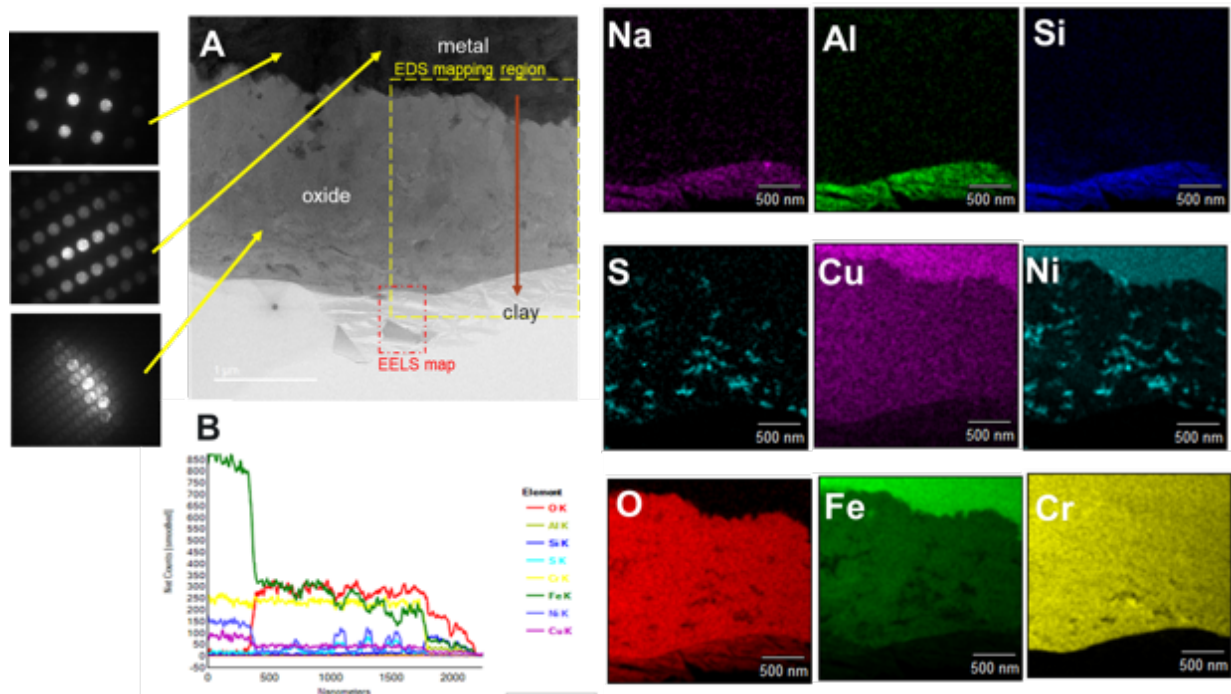


NOTE:   The oxide layer contains particles of Ni-sulfide. Both Fe and Cu are present in the oxide layer, but at lower levels than in the metal. In contrast, Cr was uniform throughout the corrosion rind. The clay was a sodium alumino-silicate.

**Figure 8-16.  Image and diffraction patterns of the corrosion rind
with an EDS line profile and elemental maps**

Iron is enriched in the metal and present at lower levels in the oxide, as expected. Ni and S have formed sulfides throughout the oxide zone. Diffraction data was also collected from the different regions in the specimen.
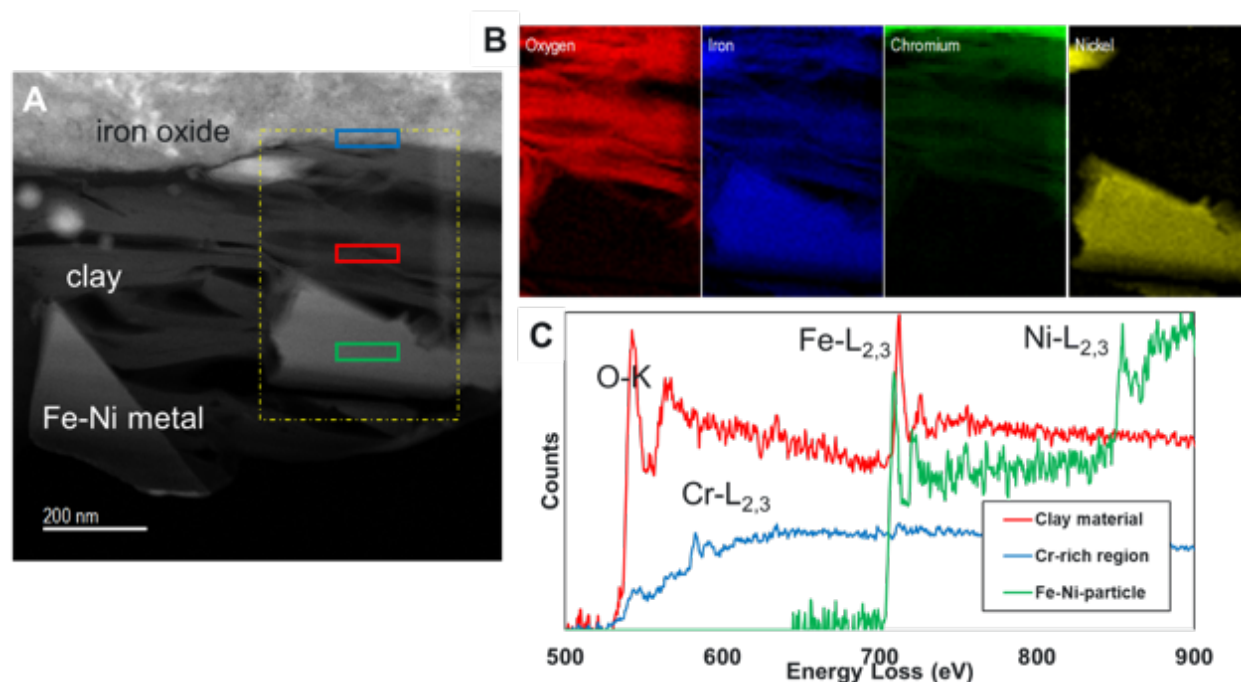
NOTE:    A shift in the Fe-L$_{2,3}$ edge indicates oxidation of Fe in the clay relative to the other phase.

**Figure 8-17.  (a) Image of the corrosion rind, (b) EELS elemental maps
of the major elements, and (c) EELS spectra of three major regions
noted in (a), including a Fe-Ni particle in the clay, most likely a sulfide**

## 8.4    Conclusions for In-situ Electrochemical Testing

We are developing the tools that will enable us to conduct in-situ liquid SEM analyses of UO$_2$ to validate the electrochemical model for long-term disposal of nuclear fuel. Furthermore, in-situ ToF-SIMS analysis could complement the in-situ SEM imaging and provide information on the U species forming in solution during the corrosion processes.

The following list summarizes key findings pertinent to the three types of experiments conducted:

- **In-situ Liquid SIMS of UO$_2$**—Our in-situ liquid SIMS results illustrate that we can use it to detect the changes of the UO$_2$ electrode before and after applying potentials to the electrode and examine the corrosion process of UO$_2$. It is envisioned that in-situ and in operando approaches will provide new insights into spent fuel chemistry of importance, simulating repository conditions and enhance our ability to manage and control nuclear materials at microscale.

- **Electrochemical Analysis of Uranyl Nitrate for In-situ SEM**—The cyclic voltammagram of U (VI) nitrate dissolved in 0.1 M HNO$_3$ showed reduction and possible oxidation processes that were not existing in the control blank sample. In addition, experimental results suggest that we use a wider range of potentials in future experiments. Moreover, a smaller Au film conductive substrate is needed to reduce the interference of H and Au. Future testing will include the scanning rate dependency of the uranyl nitrate using this three-electrode cell with improved UO$_2$ WE design.
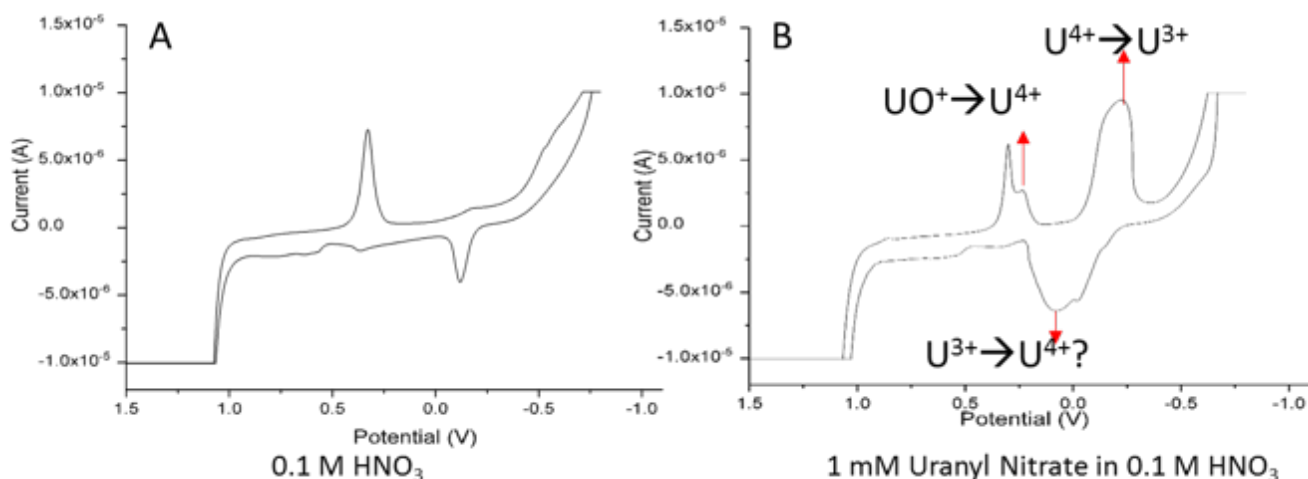
- **Multimodal Imaging of the LANL Metal Coupon**—The 3D SIMS analysis demonstrates the capability of dynamic ToF-SIMS in providing the elemental and molecular information as a

function of depth. The 3D visualization can be utilized to reveal the species present around the clay-metal interface, providing insights into the corrosion process at the bentonite–steel interface.

# 9.   CONCLUSIONS

This report documents progress made during FY19 on the EBS R&D Work Package in the SFWST Campaign. The R&D activities were designed to improve the understanding of EBS component evolution and interactions, as well as interactions between the host media and the EBS. A primary goal of this work is to advance the development of process models that include certain distinct processes that can be incorporated into a PA or can provide critical information for implementing better contraints on barrier performance. The plan is to either directly implement the models within the GDSA platform or use the models for confidence building and/or to provide insight into the underlying processes. The R&D team consisted of individuals from Sandia, LBNL, LANL, PNNL, BRGM, the University of California Berkeley, and Mississippi State University.

The FY19 EBS activities involved modeling and analysis work as well as experimental work. The following subsections summarize the progress made in the different research areas.

## 9.1   Thermal Analysis for the Disposal of Dual Purpose Canisters in Sedimentary Host Rjock using the Semi-analytical Method (Section 2)

Semi-analytical, thermal calculations were conducted regarding the direct disposal of DPCs in a generic closed-mode, sedimentary repository setting. Conducted to support GDSA PFLOTRAN simulations, the calculations investigate parameters that could influence management of the high thermal loads expected with DPCs due to the large number of PWR assemblies per waste package. The analysis examined the effects of drift spacing, waste package spacing, backfill thermal conductivity, number of PWR assemblies per waste package, and surface storage period. The predicted results show that a combination of a larger repository foot print, a longer surface storage time and an engineered buffer would be required to control peak temperatures. Alternative disposal concepts were also shown as part of sensitivity analysis. The results are in line with previous analyses.

## 9.2   Tetravalent Uranium Solubility and Speciation (Section 3)

Experiments were conducted to investigate the solubility of $UO_2$ and speciation of U in $SO_4$-bearing, 1-m NaCl solutions at 250°C, 300°C, and 350°C and saturated water vapor pressure. The predominant sulfate complex of U(IV) was identified as the neutral aqueous species, $U(OH)_2SO_4^{\circ}$. Earlier work on chloride complex of U(IV), such as $UCl_4^{\circ}$ (Timofeev et al. 2018), showed that its stability has a strong negative correlation with pH and thus it plays an important role only in acidic solutions. In contrast, the species identified in this study contribute appreciably to the mass balance of dissolved uranium even in more realistic solutions of near-neutral acidity. In the sulfate-bearing solutions ranging from 0.01 to 0.35 mol/kg of total dissolved sulfate, the $U(OH)_2SO_4^{\circ}$ species controls the solubility of uranium at reducing conditions. However, even within more modest sulfate concentration ranges, uranium concentrations can develop ranging from hundreds of ppb to tens of ppm and even more when in equilibrium with uraninite, a mineral phase commonly encountered in both natural and engineered systems. Logarithms of the formation constant ($U_4^+ + SO_4^{2-} + 2OH^- = U(OH)_2SO_4$) for this species are 30.18, 32.16, and 36.31, respectively, at 250°C, 300°C, and 350°C.

## 9.3   THMC Modeling of Impact of High Temperature on EBS Bentonite (Section 4)

In the past few years, we have dedicated our effort to developing a coupled THMC model to evaluate the chemical alteration and associated mechanical changes in a generic repository and to consider the interaction between EBS bentonite and the natural system clay formation. Two main scenarios were developed for comparison: a "high T" case, in which the temperature near the waste package can reach

about 200°C, and a "low T" case, in which the temperature peaks at about 100°C. THMC modeling of coupling of chemical and mechanical processes is the key part of the evaluation of the impact of chemical changes on the mechanical behavior of bentonite. In FY19, we started to use a new simulator TReactMech to work on Linux platform, which is more suitable for large-scale computations and better able to incorporate other mathematical or physical tools for coupled modeling. The milestones reached are as follows:

- We added the dual structure model, BExM, to link mechanical process with chemistry in TOUGHREACT-FLAC to allow us to simultaneously incorporate the effects of exchangeable cations, ionic strength of pore water and abundance of swelling clay on the swelling stress of bentonite.

- We ran new high T and low T simulations. The ultimate goal is to investigate the thermal limit of clay repository. Reliable evaluation of the impact of a long-term geochemical effect on mechanical behavior will help determine whether a clay repository can sustain higher temperature.

- We introduced the new simulator TReactMech on a Linux platform. An initial 3D THM benchmark test was studied. The application of a numerical code TReactMech was validated by means of a comparison with analytical solutions.

The current coupled THMC model on a Windows platform greatly improves our understanding of the coupled processes contributing to chemical and mechanical alteration in EBS bentonites and natural system argillite formations and answers questions regarding the thermal limit of EBS bentonite in clay repository. However, for solving large problems and better modeling efficiency, the simulator for conducting coupled THMC modeling needs to be improved. In the remaining time of FY20, we are planning:

- To investigate chemical induced deformation in a solid skeleton related to changes of solution compositions, and to derive an improved constitutional model for swelling pressure in compacted clays. In that way, we can develop a stricter MC coupled model in the framework of poromechancis. A better quantitative understanding of how chemical change controls the material structure is required. Studies will be focused on developing and verifying such relationships and searching data for parameter calibration

- To derive a reduced order model (ROM) that can be integrated into the PA model in GDSA. The importance of bentonite alteration and its impact on mechanical behavior needs to be integrated to PA model to assess their relevance to the safety of a repository. Specifically, we will first implement of bentonite swelling models such as linear swelling, state surface, BBM, and BExM into a parallel THMC simulator TReactMech and a ROM will be developed based on a large number of THMC simulations.

## 9.4 Integration of Coupled THC Model with GDSA using Reduced-order Model (Section 5)

The THC model was used to develop a ROM to compute an apparent $K_d$ as a function of time and space (or averaged across EBS), which can be plugged into the PA model. As the first step, we simulated the THC process within a buffer-argillite system using TOUGHREACT, and computed $K_d$ at each grid block over time. The results show that although the $K_d$ values vary over one order of magnitude in space and time in parallel lines, the temporal evolution is spatially consistent. This would make it possible to develop the statistical representation of the $K_d$ evolution across the space in a relatively straightforward manner. In addition, the dependency of $K_d$ on pH is fairly linear, which could also be used to create

ROM, although the dependency has to be evaluated at different geochemical conditions and parameters based on the application of the UQ. A spatial averaging strategy was considered to determine the $K_d$ value representing the entire buffer as a single grid block in the PA model. Simple averaging of $K_d$ over the buffer overestimated the overall adsorbed mass, compared to the apparent $K_d$ over the buffer based on the buffer-averaged adsorbed and aqueous concentrations. Comparison of numerical and experimental results is needed to substantiate the developed approach.

## 9.5    Studying Chemical Controls on Montmorillonite Structure and Swelling Pressure (Section 6)

### 9.5.1    Computational and Thermodynamic Modeling of Clay Swelling

Modeling the evolution of compacted clay microstructure in response to chemical perturbations in aqueous chemistry requires a detailed understanding of the molecular-level forces that regulate water adsorption and ion exchange thermodynamics in the clay interlayer nanopores. We are combining molecular mechanics simulations (MD and GCMC) with thermodynamic modeling to predict the coexistence of multiple swelling states (e.g. 2-water layer hydrate coexisting with 3-water layer hydrate) for montmorillonite clay. Our key accomplishments include:

- We have developed a realistic molecular model of cis-vacant montmorillonite. We equilibrated this structure in homoionic NaCl and KCl to determine the molecular structure of the interlayer water and counterions (e.g., $Na^+$ and $K^+$) for the 1- and 2-water layer hydrates. Stronger H-bonding of interlayer nanopore water molecules with the structural hydroxyl sites in the clay sheet causes water to be more highly structured in the cis-vacant structure compared to trans-vacant clay.

- We performed a series of molecular simulations to determine a physiochemical basis for observed rotational ordering of Na- and K-montmorillonite. Static equilibrium calculations indicate that crystallographically oriented layers are energetically preferred for the 1-water layer states, but forced rotations indicate that multiple rotational orientations are energetically accessible due to thermal fluctuations.

- Crystalline hydrate phase coexistence data derived from SAXS measurements were used to develop a thermodynamic model for ion exchange driven swelling and collapse of montmorillonite. Swelling pressures for compacted clay (1600 kg/m$^3$) are shown to vary with the composition of the electrolyte, with highest swelling pressures occurring in equilibrium with relatively low water activity Na-rich aqueous fluids.

Our ongoing work employs our new molecular model to provide validation of and inputs for the thermodynamic model in mixed Na/K electrolyte. Currently, the model assumes a regular solution model for mixing of the 2- and 3-water layer hydrate swelling states. We are using MD results to directly calculate excess mixing energies and to explain the non-ideal mixing behavior. Future work will extend this model to include aqueous $CaCl_2$, which is a major counterion component in bentonite employed in EBS. This work will involve additional SAXS studies to measure distributions of swelling states as a function of counterion composition as well as a complementary suite of MD simulations.

### 9.5.2    Chemical Controls on Montmorillonite Swelling Pressure and Structure

As described in Section 4.4 of Zheng et al. (2019), we collaborated with Drs. Francis Claret and Stephane Gaboreau, BRGM Orléans, to develop a miniaturized oedometer cell for synchrotron x-ray studies of dynamic changes in compacted swelling clay structure. This system will enable SAXS to measure distributions of interlayer distances as well as microscale x-ray computed tomography ($\mu$XCT) to measure interparticle pore dimensions. This system will permit us to follow changes in bentonite interlayer spacing

and submicron structure as a function of solution composition and to test our predictions of swelling pressure.

The oedometer has been calibrated at BRGM and was scheduled to be shipped to LBNL early in FY20 for experiments that measure the changes in bentonite swelling pressure during ion-exchange. Laboratory studies of swelling and swelling hysteresis for a range of electrolyte compositions (including Na, K and Ca) and concentrations were planned to provide new experimental tests of our thermodynamic models for swelling. In addition, SAXS beamtime is scheduled at beamline 5-ID of the Advanced Photon Source (APS), which will provide information on the evolution of interlayer and interpore dimensions during ion exchange and smectite expansion and collapse.

## 9.6    Transmission X-ray Microscope (TXM) for In-situ Nanotomography of Bentonite and Shale (Section 7)

To deepen our understanding of relationship of clay swelling and chemical conditions, we plan to design and commission a new TXMs at beamline 11.3.1 and provide proof-of-principle data on (1) the structural evolution of hydrated compacted bentonite under changing chemical conditions or (2) the deformation and fracture sealing of candidate repository rocks, such as shale or halite, under stress over multiple time scales. We have completed the sample selection, experimental design. The TXM specifications are chosen to enable the imaging of the pore structure between smectite particles and the deformation of smectite particles and mineral inclusions in shale. The x-ray energy is chosen to be sufficiently high to pass through environmental sample cells in order to enable time-lapse studies of rock-fluid systems under controlled conditions. As part of this project, a new sample cell is designed and fabricated that can be used to apply uniaxial stress and allow for the flow of aqueous fluids.

Excellent progress was made in FY19 on the construction of an x-ray microscope dedicated to in-situ nanotomography studies of the MC evolution of geological materials, particularly clay media and clay-rich rocks. A novel uniaxial stress-strain cell has been designed and all components purchase or fabricated. An optical imaging system has been set up to enable preliminary studies of flow and compaction.

X-ray operations were expected to commence in early FY20 with TXM commissioning to proceed over the subsequent 4 weeks. The experimental emphasis was expected to rapidly transition from characterizing the imaging performance of the instrument using calibration standards to performing initial studies of clay and shale samples under ambient conditions. The first in-situ studies were expected at 6 weeks following x-ray operation.

## 9.7    In-situ Electrochemical Testing of Uranium Dioxide under Anoxic Conditions (Section 8)

Analyzing radioactive materials in liquids and slurries can be challenging using bulk approaches. As an alternative, the research team has developed the SALVI, a vacuum-compatible, microfluidic device, to enable surface analysis of liquids and liquid-solid interactions using SEM and ToF-SIMS. The goal is to provide real-time and in-operando monitoring of $UO_2$ electrode stability and morphological change and to study the $UO_2$ corrosion process at the microscale.

Much of the FY19 effort involved establishing the capabilities to this new experimental approach. Additional staff that could provide expertise on electrochemistry and the operation of the in-situ cells were brought onto the project. Equipment suitable for in-situ electrochemical corrosion testing of $UO_2$ was purchased and/or built as needed. Initial testing of this new experimental approach demonstrates that multimodal analysis of $UO_2$ materials is possible using SALVI and in-situ chemical imaging. Both in-situ liquid SEM and SIMS can be used as new approaches to analyze radioactive materials in liquid and slurry

forms of high-level nuclear wastes. In addition, stainless steel materials, like those that would be used in the repository setting, were analyzed using multiple surface tools including SEM, TEM, XPS, and ToF-SIMS. The results show that material interfaces change as a result of redox chemistry in the repository environment. Further investigation is warranted to understand the physical and chemical processes to support the process model development.

The following list summarizes key findings pertinent to the three types of experiments conducted:

- **In-situ Liquid SIMS of $UO_2$**—Our in-situ liquid SIMS results illustrate that we can use it to detect the changes of the $UO_2$ electrode before and after applying potentials to the electrode and examine the corrosion process of $UO_2$. It is envisioned that in-situ and in operando approaches will provide new insights into spent fuel chemistry of importance, simulating repository conditions, and enhance the ability to manage and control nuclear materials at microscale.

- **Electrochemical Analysis of Uranyl Nitrate for In-situ SEM**—The cyclic voltammagram of U (VI) nitrate dissolved in 0.1 M $HNO_3$ showed reduction and possible oxidation processes that were not existing in the control blank sample. In addition, experimental results suggest that we use a wider range of potentials in future experiments. Moreover, a smaller Au film conductive substrate is needed to reduce the interference of H and Au. Future testing will include the scanning rate dependency of the uranyl nitrate using this three-electrode cell with improved $UO_2$ WE design.

- **Multimodal Imaging of the LANL Metal Coupon**—The 3D SIMS analysis demonstrates the capability of dynamic ToF-SIMS in providing the elemental and molecular information as a function of depth. The 3D visualization can be utilized to reveal the species present around the clay-metal interface, providing insights into the corrosion process at the bentonite–steel interface.

This page is intentionally left blank.

# 10. REFERENCES

Ahn, J., D. Kawasaki, and P.L. Chambré. 2002. "Relationship among performance of geologic repositories, canister-array configuration, and radionuclide mass in waste." *Nucl. Technol.* 140:94–112.

Ahonen, L., H. Ervanne, T. Jaakkola, and R. Blomqvist. 1994. "Redox chemistry in uranium-rich groundwater of Palmottu uranium deposit, Finland." *Radiochim. Acta* 66/67:115–121.

Aja, S.U., S.A. Wood, and A.E. Williams-Jones. 1995. "The aqueous geochemistry of Zr and the solubility of some Zr-bearing minerals." *Appl. Geochemistry* 10:603–620.

Allard, B. 1982. "Solubilities of Actinides in Neutral or Basic Solutions." *Actinides in Perspective.* 553–580. Elsevier. Available at: https://linkinghub.elsevier.com/retrieve/pii/B9780080291932500298.

Andrews, J.C., E. Almeida, M.C. van der Meulen, J.S. Alwood, C. Lee, Y. Liu, J. Chen, F. Meirer, M. Feser, and J. Gelb. 2010. "Nanoscale X-ray microscopic imaging of mammalian mineralized tissue." *Microscopy and Microanalysis* 16:327 –336.

Bastrakov, E., S. Jaireth, and T.P. Mernagh. 2010. "Solubility of uranium in hydrothermal fluids at 25-300°C: Implications for the formation of uranium deposits." *Geoscience Australia Record* 2010.

Bea, S.A., H. Wainwright, N. Spycher, B. Faybishenko, S.S. Hubbard, and M.E. Denham. 2013. "Identifying key controls on the behavior of an acidic-U (VI) plume in the Savannah River Site using reactive transport modeling." *Journal of Contaminant Hydrology* 151:34–54.

Berendet, I., J.-M. Cases, M. Francoise, J.-P. Uriot, L. Michot, A. Masion, and F. Thomas. 1995. "Mechanism of adsorption and desorption of water vapor by homoionic montmorillonites: 2. the Li+, Na+, K+, Rb+ And Cs+-exchanged forms." *Clays and Clay Minerals* 43(3): 324–336.

Booker, J.R. and C. Savvidou. 1985. "Consolidation around a point heat source." *International Journal for Numerical and Analytical Methods in Geomechanics* 9:173–184.

Bossart, P. 2011. *Characteristics of the Opalinus Clay at Mont Terri*. Mont Terri Project, Wabern Switzerland.

Boţan, A., B. Rotenberg, V. Marry, P. Turq, and B. Noetinger. 2011. "Hydrodynamics in Clay Nanopores." *The Journal of Physical Chemistry C* 115.

Bourg, I.C. and G. Sposito. 2011. "Molecular dynamics simulations of the electrical double layer on smectite surfaces contacting concentrated mixed electrolyte (NaCl–CaCl₂) solutions." *Journal of Colloid and Interface Science* 360 (2): 701–715.

Bradbury, M.H., B. Baeyens. 2011. "Predictive sorption modelling of Ni(II), Co(II), Eu(III), Th(IV) and U(VI) on MX-80 bentonite and Opalinus Clay: A "bottom-up" approach." *Applied Clayence* 52:27–33.

Brookins, D.G. 1990. "Radionuclide behabior at the Oklo nuclear reactor, Gabon." *Waste Manag.* 10:285–296.

Buck, E.C. and R.S. Wittman. 2014. *Radiolysis Model Formulation for Integration with the Mixed Potential Model.* Richland, WA: Pacific Northwest National Laboratory.

Buck, E.C., R.S. Wittman, C.Z. Soderquist, and B.K. McNamara. 2018. "Monitoring bromide effect on radiolytic yields using in situ observations of uranyl oxide precipitation in the electron microscope." *RSC Advances* 8 (33): 18227–18233.

Burns, P.C., R.C. Ewing, and A. Navrotsky. 2012. "Nuclear fuel in a reactor accident." *Science* 335 (6073): 1184–1188. doi: 10.1126/science.1211285.

Cacuci, D.G. 2003. *Sensitivity and Uncertainty Analysis, Vol. 1: Theory*. Boca Raton, FL: Chapman and Hall/CRC Press.

Caporuscio, F.A., S.E.M. Palaich, M.C. Cheshire, and C.F. Jové-Colón. 2017. "Corrosion of copper and authigenic sulfide mineral growth in hydrothermal bentonite experiments." *J. Nucl. Mater.* 485:137–146.

Caporuscio, F.A., M.C. Cheshire, M.S. Rearick, and C. Jové-Colón. 2014. *Argillite EBS Experimental Program 2014: Fuel cycle research and development*. :Los Alamos, NM: Los Alamos National Laboratory.

Caporuscio, F.A., S.E.M. Palaich, M.C. Cheshire, and C.F. Jové Colón. 2017. "Corrosion of copper and authigenic sulfide mineral growth in hydrothermal bentonite experiments." *Journal of Nuclear Materials* 485:137–146.

Carbol, P., J. Cobos-Sabate, J.-P. Glatz, C. Ronchi, V. Rondinella, D.H. Wegen, T. Wiss, A. Loida, V. Metz, B. Kienzler, K. Spahiu, B. Grambow, J. Quiñones, and A. Martínez Esparza Valiente. 2005. *The effect of dissolved hydrogen on the dissolution of $^{233}U$ doped $UO_2(s)$, high burn-up spent fuel and MOX fuel*. TR-05-09. Stockholm, Sweden: Svensk Kärnbränslehantering AB.

Casas, I., J. De Pablo, J. Giménez, M.E. Torrero, J. Bruno, E. Cera, R.J. Finch, and R.C. Ewing. 1998. "The role of pe, pH, and carbonate on the solubility of $UO_2$ and uraninite under nominally reducing conditions." *Geochim. Cosmochim. Acta* 62:2223–2231.

Castellanos, E., M.V. Villa, E. Romero, A. Lloret, and A. Gens. 2008. "Chemical impact on the hydro-mechanical behaviour of high-density FEBEX bentonite." *Physics and Chemistry of the Earth* 33:S516–S526.

Cheshire, M.C., F.A. Caporuscio, C.F. Jové Colón, and K.E. Norskog. 2018. "Fe-saponite growth on low-carbon and stainless steel in hydrothermal-bentonite experiments." *J. Nucl. Mater* 511:353–366.

Cheshire, M.C., F.A. Caporuscio, M.S. Rearick, C. Jové-Colón, and M.K. McCarney. 2014. "Bentonite evolution at elevated pressures and temperatures: An experimental study for generic nuclear repository designs." *Am. Mineral.* 99:1662–1675.

Conroy, M., J.A. Soltis, R.S. Wittman, F.N. Smith, S. Chatterjee, X. Zhang, E.S. Ilton, and E.C. Buck. 2017. "Importance of interlayer H bonding structure to the stability of layered minerals." *Scientific Reports* **7**(1): 13274. doi: 10.1038/s41598-017-13452-7.

Cuney, M. 2009. "The extreme diversity of uranium deposits." *Miner. Depos.* 44:3–9.

Ding, Y., Y. Zhou, J. Yao, C. Szymanski, J. Fredrickson, L. Shi, B. Cao, Z. Zhu and X.-Y. Yu. 2016. "In Situ Molecular Imaging of the Biofilm and Its Matrix." *Analytical Chemistry* 88 (22): 11244–11252.

DOE (U.S. Department of Energy). 2008. *Yucca Mountain Repository License Application for Construction Authorization*. DOE/RW-0573 Update 1. Washington, D.C.: U.S. Department of Energy.

Dong, W., T. Tokunaga, J. Davis, J. Wan, 2012. "Uranium (VI) adsorption and surface complexation modeling under acidic conditions: background sediments from the F-Area Savannah River Site." *Environmental Science and Technology* 46:1565–1571.

Drits, V.A. and B.B. Zviagina. 2009. "Trans-vacant and cis-vacant 2:1 layer silicates: Structural features, identification, and occurrence." *Clays and Clay Minerals* 57 (4): 405–415.

Easton, E. 2011. "Developing a Regulatory Framework for Extended Storage and Transportation." Presentation for the *National Transportation Stakeholder Forum*. May 10–12, 2011. Denver, CO. energy.gov/sites/prod/files/em/Easton_NTSF_2011.pdf.

Ellis, G.S., A.L. Sessions, A. Deev, Z. Aizenshtat, J.F. Adkins, Y. Tang, A. Meshoulam, W.P. Gilhooly, W. Said Ahmad, J. Liu, and A. Amrani. 2016. "Study of thermochemical sulfate reduction mechanism using compound specific sulfur isotope analysis." *Geochim. Cosmochim. Acta* 188:73–92. http://dx.doi.org/10.1016/j.gca.2016.05.026.

Engelhard, M.H., X. Guo, A. Lanzirotti, E.S. Ilton, M. Newville, A. Navrotsky, R.K. Kukkadapu, S.R. Sutton, and H. Xu. 2016. "Structure and thermodynamics of uranium-containing iron garnets." *Geochim. Cosmochim. Acta* 189:269–281.

Ewing, R.C. 2015. "Long-term storage of spent nuclear fuel." *Nat. Mater.* 14:252–257. http://www.nature.com/doifinder/10.1038/nmat4226.

Finsterle, S. 2010. *iTOUGH2 User's Guide, Report LBNL-40040.* Berkeley, CA: Lawrence Berkeley National Laboratory.

Finsterle, S. and Y. Zhang. 2011. "Solving iTOUGH2 simulation and optimization problems using the PEST protocol." *Environmental Modelling and Software* 26:959–968. doi:10.1016/j.envsoft.2011.02.008, 2011.

Gammons, C.H., S.A. Wood, J.P. Jonas, and J.P. Madison. 2003. "Geochemistry of the rare-earth elements and uranium in the acidic Berkeley Pit lake, Butte, Montana." *Chem. Geol.* 198:269–288.

Gens, A. 2010. "Soil environment interactions in geotechnical engineering." *Géotechnique* 60:3–74.

Goldstein, T.P. and Z. Aizenshtat. 1994. "Thermochemical sulfate reduction a review." *J. Therm. Anal.* 42:241–290.

Grambow, B. and S. Bretesché. 2014. "Geological disposal of nuclear waste: II. From laboratory data to the safety analysis – Addressing societal concerns." *Appl. Geochemistry* 49:247–258. http://linkinghub.elsevier.com/retrieve/pii/S088329271400119X.

Grenthe, I., H. Wanner, and I. Forest. 1992. *Chemical Thermodynamics of Uranium*. Amsterdam, Netherlands: Elsevier.

Guillaumont, R., T. Fanghanel, V. Neck, J. Fuger, D.A. Palmer, I. Grenthe, and M.H. Rand. 2003. "Update on the chemical thermodynamics of uranium, neptunium, plutonium, americium and technetium." *Chem. Thermodyn.* 5:919. https://books.google.de/books/about/Update_on_the_Chemical_Thermodynamics_of.html?id=J9zvAAAAMAAJ&redir_esc=y.

Guimarães, L.D.N., A. Gens, M. Sánchez, and S. Olivella. 2013. "A chemo-mechanical constitutive model accounting for cation exchange in expansive clays." *Géotechnique* 63:221–234.

Guo, X., A. Navrotsky, R.K. Kukkadapu, M.H. Engelhard, A. Lanzirotti, M. Newville, E.S. Ilton, S.R. Sutton, and H. Xu. 2016. "Energetics of a Uranothorite (Th1 – xUxSiO4) Solid Solution." *Geochim. Cosmochim. Acta* 189:269–281.

Hadgu, T., D. Clayton, and E. Hardin. 2015. *Cavern/Vault Disposal Concepts and Thermal Calculations for Direct Disposal of 37-PWR Size DPCs*. FCRD-UFD-2015-000715. Albuquerque, NM: Sandia National Laboratories.

Hardin, E. and M. Voegele. 2013. *Alternative Concepts for Direct Disposal of Dual-Purpose Canisters.* U.S. Department of Energy, Used Fuel Disposition R&D Campaign. FCRD-UFD- 2013-000102 Rev. 0. Albuquerque, NM: Sandia National Laboratories.

Hardin, E., J. Blink, H. Greenberg, M. Sutton, M. Fratoni, J. Carter, M. Dupont, and R. Howard. 2011. *Generic repository design Concepts and Thermal Analysis*. FCRD-USED-2011-000143, Rev. 0. Albuquerque, NM: Sandia National Laboratories.

Hardin, E., L. Price, E. Kalinina, T. Hadgu, A. Ilgen, C. Bryan, J. Scaglione, K. Banerjee, J. Clarity, R. Jubin, V. Sobes, R. Howard, J. Carter, T. Severynse, and F. Perry. 2015. *Summary of Investigations on Technical Feasibility of Direct Disposal of Dual-Purpose Canisters*. FCRD-UFD-2015-000129. Albuquerque, NM: Sandia National Laboratories.

Hardin, E., T. Hadgu, D. Clayton, R. Howard, H. Greenberg, J. Blink, M. Sharma, M. Sutton, J. Carter, M. Dupont, and P. Rodwell. 2012. *Disposal Concepts/Thermal Load Management (FY11/12 Summary Report)*. FCRD-UFD-2012-00219; Milestone M3FT-12SN0804032. Albuquerque, NM: Sandia National Laboratories.

Hardin, E.L., D.J. Clayton, R.L. Howard, J.M. Scaglione, E. Pierce, K. Banerjee, M.D. Voegele, H.R. Greenberg, J. Wen, T.A. Buscheck, J.T. Carter, T. Severynse and W.M. Nutt. 2013. *Preliminary Report on Dual-Purpose Canister Disposal Alternatives (FY13)*. FCRD-UFD-2013-000171, Rev. 1. Albuquerque, NM: Sandia National Laboratories.

Haynes, D.W., K.C. Cross, R.T. Bills, and M.H. Reed. 1995. "Olympic Dam ore genesis; a fluid-mixing model." *Econ. Geol.* 90:281–307. doi: https://doi.org/10.2113/gsecongeo.90.2.281.

Helgeson, H.C., D.H. Kirkham, and G.C. Flowers. 1981. "Theoretical prediction of the thermodynamic behavior of aqueous electrolytes at high pressures and temperatures: IV. Calculation of activity coefficients, osmotic coefficients, and apparent molal and standard and relative partial molal properties to 600°." *Am. J. Sci.* 281:1249–1516.

Hennig, C., K. Schmeide, V. Brendler, H. Moll, S. Tsushima, and A.C. Scheinost. 2007. "EXAFS investigation of U(VI), U(IV), and Th(IV) sulfato complexes in aqueous solution." *Inorg. Chem.* 46:5882–92. http://www.ncbi.nlm.nih.gov/pubmed/17580931.

Holmboe, M. and I.C. Bourg. 2013. "Molecular dynamics simulations of water and sodium diffusion in smectite interlayer nanopores as a function of pore size and temperature." *The Journal of Physical Chemistry C* 118 (2): 1001–1013.

Honorio, T., L. Brochard., and M. Vandamme. 2017. "Hydration Phase Diagram of Clay Particles from Molecular Simulations." *Langmuir* 33:12766–12776.

Hsiao, Y. and M. Hedström. 2017. "Swelling pressure in systems with na-montmorillonite and neutral surfaces: A molecular dynamics study." *The Journal of Physical Chemistry C* 121 (47): 26414–26423.

Itasca. 2009. *FLAC3D, Fast Lagrangian Analysis of Continua in 3 Dimensions, Version 4.0*. Minneapolis, MN: Itasca Consulting Group.

Jerden Jr, J.L., K. Frey, and W. Ebert. 2015. "A multiphase interfacial model for the dissolution of spent nuclear fuel." *Journal of Nuclear Materials* 462:135–146.

Johnson, J.W., E.H. Oelkers, and H.C. Helgeson. 1992. "SUPCRT92: A software package for calculating the standard molal thermodynamic properties of minerals, gases, aqueous species, and reactions from 1 to 5000 bar and 0 to 1000 °C." *Comput. Geosci.* 18:899–947. http://linkinghub.elsevier.com/retrieve/pii/009830049290029Q.

Kestin, J., J. Sengers, and B. Kamgar-Parsi. 1984. "Thermophysical Properties of Fluid $H_2O$." *J. Phys. Chem. Ref.* 13:175–183. http://potomac.nist.gov/srd/PDFfiles/jpcrd250.pdf.

Kim, J., E. Sonnenthal, and J. Rutqvist. 2015. "A sequential implicit algorithm of chemo-thermo-poromechanics for fractured geothermal reservoirs." *Computers & Geosciences* 76:59–71.

Kim, J., E.L. Sonnenthal, and J. Rutqvist. 2012. "Formulation and sequential numerical algorithms of coupled fluid/heat flow and geomechanics for multiple porosity materials." *International Journal for Numerical Methods in Engineering* 92 (5): 425–456.

Kister, P., P. Vieillard, M. Cuney, D. Quirt, and E. Laverret. 2005. "Thermodynamic constraints on the mineralogical and fluid composition evolution in a clastic sedimentary basin: the Athabasca Basin (Saskatchewan, Canada)." *Eur. J. Mineral.* 17:325–341. http://www.ingentaselect.com/rpsv/cgi-bin/cgi?ini=xref&body=linker&reqdoi=10.1127/0935-1221/2005/0017-0325.

Kneafsey, T.J., S. Nakagawa, E.L. Sonnenthal, M. Voltolini, P.F. Dobson, J.T. Smith, and S.E. Borglin. 2017. "Comparison of Experimental and Modeling Results of Fracture Sustainability in EGS Systems." *42nd Workshop on Geothermal Reservoir Engineering: Stanford, California, USA, 13–15 February 2017*. 768. Stanford, CA: Stanford Geothermal Program; Red Hook, NY: Curran Associates, Inc.

Komninou, A. and D.A. Sverjensky. 1995. "Hydrothermal alteration and the chemistry of ore-forming fluids in an unconformity-type uranium deposit. Geochim." *Cosmochim. Acta* 59:2709–2723.

Lammers, L.N., I.C. Bourg, M. Okumura, K. Kolluri, G. Sposito, and M. Machida. 2017. "Molecular dynamics simulations of cesium adsorption on illite nanoparticles." *Journal of colloid and interface science* 490:608–620.

Lauber, M., B. Baeyens, and M.H. Bradbury. 2000. *Physico-Chemical Characterisation and Sorption Measurements of Cs, Sr, Ni, Eu, Th, Sn and Se on Opalinus Clay from Mont Terri*. PSI Bericht Nr.00-10; Nagra Technical Report NTB 00-11. Villigen, Switzerland: Paul Scherrer Inst; Wettingen, Switzerland: Nagra.

Li, H., C. Cai, L. Jia, C. Xu, and K. Zhang. 2017. "The Effect of Water Chemistry on Thermochemical Sulfate Reduction: A Case Study from the Ordovician in the Tazhong Area, Northwest China." *Geofluids* 2017 (34): 1–11. DOI: 10.1155/2017/6351382.

Liu, B., X.-Y. Yu, Z. Zhu, X. Hua, L. Yang, and Z. Wang. 2014. "In situ chemical probing of the electrode-electrolyte interface by ToF-SIMS." *Lab on a Chip* 14 (5): 855–859.

Liu, H.H., J. Houseworth, J. Rutqvist, L. Zheng, D. Asahina, L. Li, V. Vilarrasa, F. Chen, S. Nakagawa, S. Finsterle, C. Doughty, T. Kneafsey, and J. Birkholzer. 2013. *Report on THMC modeling of the near field evolution of a generic clay repository: Model validation and demonstration*. FCRD-UFD-2013-0000244. Berkeley, CA: Lawrence Berkeley National Laboratory.

Liu, X.-D. and X.-C. Lu. 2006. "A Thermodynamic Understanding of Clay-Swelling Inhibition by Potassium Ions." *Angew. Chem. Int. Ed.* 45:6300–6303.

Lloret, A., M.V. Villar, M. Sánchez, A. Gens, X. Pintado, E.E. Alonso. 2003. "Mechanical behaviour of heavily compacted bentonite under high suction changes." *Géotechnique* 53 (1): 27–40.

Mariner, P.E., E.R. Stein, J.M. Frederick, S.D. Sevougian, and G.E. Hammond. 2017. *Advances in Geologic Disposal System Modeling and Shale Reference Cases*. SFWD-SFWST-2017-000044; SAND-2017-10304R. Albuquerque, NM: Sandia National Laboratories. doi:10.2172/1395750.

Mark, P. and L. Nilsson. 2001. "Structure and Dynamics of the TIP3P, SPC, and SPC/E Water Models at 298 K." *The Journal of Physical Chemistry A* 105:9954–9960.

Marshall, W.L. and E.U. Franck. 1981. "Ion Product of Water Substance, 0-1000°C, 1-10,000 Bars. New International Formulation and Its Background." *J. Phys. Chem. Ref. Data* 10:295–304.

Meirer, F., J. Cabana, Y. Liu, A. Mehta, J.C. Andrews, and P. Pianetta. 2011. "Three-dimensional imaging of chemical phase transformations at the nanoscale with full-field transmission X-ray microscopy." *J. Synchrot. Radiat.* 18:773–781.

Migdisov, A.A., H. Boukhalfa, A. Timofeev, W. Runde, R. Roback, and A.E. Williams-Jones. 2018. "A spectroscopic study of uranyl speciation in chloride-bearing solutions at temperatures up to 250 °C." *Geochim. Cosmochim. Acta* 222:130–145. http://linkinghub.elsevier.com/retrieve/pii/S0016703717306798.

Migdisov, A.A., A.E. Williams-Jones, V. van Hinsberg, and S. Salvi. 2011. "An experimental study of the solubility of baddeleyite (ZrO2) in fluoride-bearing solutions at elevated temperature." *Geochim. Cosmochim. Acta* 75:7426–7434.

Millero, F.J., R. Feistel, D.G. Wright, and T.J. McDougall. 2008. "The composition of Standard Seawater and the definition of the Reference-Composition Salinity Scale." *Deep. Res. Part I. Oceanogr. Res. Pap.* 55 (1): 50–72. 10.1016/j.dsr.2007.10.001.

Minisini, B. and F. Tsobnang. 2005. "Ab initio comparative study of montmorillonite structural models." *Applied Surface Science* 242:21–28.

Morris, M.D. 1991. "Factorial Sampling Plans for Preliminary Computational Experiments." *Technometrics* 33 (2): 161–174.

Murakami, H. and J. Ahn. 2011. "Development of compartment models with Markov-chain processes for radionuclide transport in repository region." *Annals of Nuclear Energy* 38 (2-3).

Myshakin, E.M., M. Makaremi, V.N. Romanov, K.D. Jordan, and G.D. Guthrie. 2014. "Molecular Dynamics Simulations of Turbostatic Dry and Hydrated Montmorillonite with Intercalated Carbon Dioxide." *Journal of Physical Chemistry A* 118:7454–7468.

Nelson, J., S. Misra, Y. Yang, A. Jackson, Y.J. Liu, H.L. Wang, H.J. Dai, J.C. Andrews, Y. Cui, and M.F. Toney. 2012. "In Operando X-ray Diffraction and Transmission X-ray Microscopy of Lithium Sulfur Batteries." *Journal of the American Chemical Society* 134:6337–6343.

Nishiyama, H., M. Suga, T. Ogura, Y. Maruyama, M. Koizumi, K. Mio, S. Kitamura, and C. Sato. 2010. "Atmospheric scanning electron microscope observes cells and tissues in open medium through silicon nitride film." *Journal of Structural Biology* 169 (3): 438–449.

Norrish, K. 1954. "The swelling of montmorillonite." *Discussions of the Faraday Society* 18:120–134.

Oelkers, E. and H.C. Helgeson. 1990. "Triple-ion anions and polynuclear complexing in supercritical electrolyte solutions." *Geochim. Cosmochim. Acta* 54:727–738. http://linkinghub.elsevier.com/retrieve/pii/001670379090368U.

Oelkers, E. and H.C. Helgeson. 1991. "Calculation of activity coefficients and degrees of formation of neutral ion pairs in supercritical electrolyte solutions." *Geochim. Cosmochim. Acta* 55:1235–1251. http://linkinghub.elsevier.com/retrieve/pii/001670379190303M.

Opel, K., S. Weiß, S. Hübener, H. Zänker, and G. Bernhard. 2007. "Study of the solubility of amorphous and crystalline uranium dioxide by combined spectroscopic methods." *Radiochim. Acta* 95:143–149.

Parks, G.A. and D.C. Pohl. 1988. "Hydrothermal solubility of uraninite." *Geochim. Cosmochim. Acta* 52:863–875.

Pau, G.S.H., Y. Zhang, and S. Finsterle. 2013. "Reduced order models for many-query subsurfaces flow application." *Computational Geosciences* 14 (4): 705–721.

Pau, G.S.H., Y. Zhang, S. Finsterle, H. Wainwright, and J. Birkholzer. 2014. "Reduced order modeling in iTOUGH2." *Computers & Geosciences* 65:118–126.

Perez, F.M., J.M. Gil, and F.J.M. Gil. 1980. "Preparation, Infrared and Visible Spectra of Sulfate Complexes of Uranium(IV)." *Zeitschrift für anorganische und allgemeine Chemie* 462 (1): 231–240. doi: 10.1002/zaac.19804620127.

Pruess, K., C. Oldenburg, and G. Moridis. 2012. *TOUGH2 User's Guide, Version 2.1*. Report LBNL-43134. Berkeley, CA: Lawrence Berkeley National Laboratory.

Pruess, K., C. Oldenburg, G. Moridis. 1999. *TOUGH2 User's Guide, Version 2.0*. Berkeley, CA: Lawrence Berkeley National Laboratory.

Ransom, B. and H.C. Helgeson. 1994. "A chemical and thermodynamic model of aluminous dioctahedral 2: 1 layer clay minerals in diagenetic processes; regular solution representation of interlayer dehydration in smectite." *American Journal of Science* 294 (4): 449–484.

Rechard, R.P., M.L. Wilson, and S.D. Sevougian. 2014. "Progression of performance assessment modeling for the Yucca Mountain disposal system for spent nuclear fuel and high-level radioactive waste." *Reliability Engineering and System Safety* 122:96–123.

Rich, R.A., H.D. Holland, and U. Peterson. 1977. *Hydrothermal Uranium Deposits.* Amsterdam: Elsevier.

Richard A., C. Rozsypal, J. Mercadier, D.A. Banks, M. Cuney, M.-C. Boiron, and M. Cathelineau. 2011. "Giant uranium deposits formed from exceptionally uranium-rich acidic brines." *Nat. Geosci.* 5:142–146. http://www.nature.com/doifinder/10.1038/ngeo1338.

Rotenberg, B., J. Morel, V. Marry, P. Turq, and N. Morel-Desrosiers. 2009. "On the driving force of cation exchange in clays: Insights from combined microcalorimetry experiments and molecular simulation." *Geochimica Et Cosmochimica Acta* 73 (14): 4034–4044.

Rutqvist, J., L. Zheng, F. Chen, H.H. Liu, and J. Birkholzer. 2014. "Modeling of coupled thermo-hydro-mechanical processes with links to geochemistry associated with bentonite-backfilled repository tunnels in clay formations." *Rock Mechanics and Rock Engineering* 47 (1): 167–186.

Ryzhenko, B.N., O.V. Bryzgalin, I.Y. Artamkina, M.Y. Spasennykh, and A.I. Shapkin. 1985. "An electrostatic model for the electrolytic dissociation of inorganic substances dissolved in water." *Geochem. Int.* 22:138–144.

Ryzhenko, B.N., Y.V. Shvarov, and N.I. Kovalenko. 1997. "The Sn-Cl-FCSHO-Na system: Thermodynamic properties of components within the conditions of the earth's crust." *Geochemistry Int.* 35:1016–1020.

Saltelli, A., M. Ratto, T. Andres, F. Campolongo, J. Cariboni, D. Gatelli, M. Saisana, and S. Tarantola. 2008. *Global Sensitivity Analysis: The Primer*. West Sussex, England: John Wiley & Sons.

Sánchez, M., A. Gens, L.J.D.N. Guimarães, and S. Olivella. 2005. "A double structure generalized plasticity model for expansive materials." *International Journal for Numerical and Analytical Methods in Geomechanics* 29:751–787.

Sani, R.K., B.M. Peyton, J.E. Amonette, and G.G. Geesey. "2004. Reduction of uranium(VI) under sulfate-reducing conditions in the presence of Fe(III)-(hydr)oxides." *Geochim. Cosmochim. Acta* 68:2639–2648.

Seward, T.M., A.E. Williams-Jones, and A.A. Migdisov. 2013. *The Chemistry of Metal Transport and Deposition by Ore-Forming Hydrothermal Fluids*. 2nd ed. Elsevier Ltd. http://dx.doi.org/10.1016/B978-0-08-095975-7.01102-5.

Shock, E.L., D.C. Sassani, and H. Betz. 1997a. "Uranium in geologic fluids: Estimates of standard partial molal properties, oxidation potentials, and hydrolysis constants at high temperatures and pressures." *Geochim. Cosmochim. Acta* 61:4245–4266.

Shock, E.L., D.C. Sassani, and H. Betz. 1997b. "Uranium in geologic fluids: Estimates of standard partial molal properties, oxidation potentials, and hydrolysis constants at high temperatures and pressures." *Geochim. Cosmochim. Acta* 61:4245–4266. http://linkinghub.elsevier.com/retrieve/pii/S0016703797002408.

Shock, E.L., D.C. Sassani, M. Willis, and D.A. Sverjensky. 1997c. "Inorganic species in geologic fluids: Correlations among standard molal thermodynamic properties of aqueous ions and hydroxide complexes." *Geochim. Cosmochim. Acta* 61:907–950.

Shvarov, Y.V. 2010. *OptimA: A program for the calculation of the free energies of dissolved aqueous species from the results of chemical experiments*.

Shvarov, Y.V. 2015. "A suite of programs, OptimA, OptimB, OptimC, and OptimS compatible with the Unitherm database, for deriving the thermodynamic properties of aqueous species from solubility, potentiometry and spectroscopy measurements." *Appl. Geochemistry* 55:17–27.

Shvarov, Y.V. and E.N. Bastrakov. 1999. *HCh, A Software Package for Geochemical Equilibrium Modeling: User's Guide*. Record 1999/25.

Smith, D.W. and J.R. Booker. 1993. "Green's functions for a fully coupled thermoporoelastic material." *International Journal for Numerical and Analytical Methods in Geomechanics* 17:139–163.

Smith, J.T., E.L. Sonnenthal, and T. Cladouhos. 2015. "Thermal-Hydrological-Mechanical Modelling of Shear Stimulation at Newberry Volcano, Oregon." Presented at 49th US Rock Mechanics/Geomechanics Symposium held in San Francisco, CA, USA.

Sobol, I.M. 2001. "Global sensitivity indices for nonlinear mathematical models and their Monte Carlo estimates." *Math. Comput. Simul.* 55 (1-3): 271–280.

Sonnenthal, E.L., J.T. Smith, T. Cladouhos, J. Kim, L. Yang. 2015. "Thermal-Hydrological-Mechanical-Chemical Modeling of the 2014 EGS Stimulation Experiment at Newberry Volcano, Oregon." *40th Workshop on Geothermal Reservoir Engineering: Stanford, California, USA, 26–28 January 2015.* Stanford, CA: Stanford Geothermal Program; Red Hook, NY: Curran Associates, Inc.

Sonnenthal, E., W. Pettitt, T. Smith, A. Riahi, D. Siler, M. Kennedy, E. Majer, P. Dobson, B. Ayling, B. Damjanac, and D. Blankenship. 2018. "Continuum Thermal-Hydrological-Mechanical Modeling of the Fallon FORGE Site." *GRC Transactions* 42.

Sonnenthal, E. and N. Spycher. 2014. *TOUGHREACT (TREACT) v3.32*. Computer software. February 28, 2014.

Sposito, G. 1972. "Thermodynamics of swelling clay-water systems." *Soil Science* 114 (4): 243–249.

Sui, X., Y. Zhou, F. Zhang, J. Chen, Z. Zhu and X.-Y. Yu. 2017. "Deciphering the aqueous chemistry of glyoxal oxidation with hydrogen peroxide using molecular imaging." *Physical Chemistry Chemical Physics* 19 (31): 20357–20366.

Sun, L., J.T. Hirvi, T. Schatz, S. Kasa, and T.A. Pakkanen. 2015. "Estimation of montmorillonite swelling pressure: A molecular dynamics approach." *The Journal of Physical Chemistry C* 119 (34): 19863–19868.

Sunder, S., J.J. Cramer, and N.H. Miller. 1996. "Geochemistry of the Cigar Lake uranium deposit: XPS studies." *Radiochim. Acta* 74:303–308.

Sverjensky, D., E.L. Shock, and H.C. Helgeson. 1997. "Prediction of the thermodynamic properties of aqueous metal complexes to 1000 C and 5 kb." *Geochim. Cosmochim. Acta* 61:1359–1412. http://linkinghub.elsevier.com/retrieve/pii/S0016703797000094.

Swiler, L.P., J.C. Helton, E. Basurto, D.M. Brooks, P.E. Mariner, L.M. Moore, S. Mohanty, S.D. Sevougian, and E.R. Stein. 2019. *Status Report on Uncertainty Quantification and Sensitivity Analysis Tools in the Geologic Disposal Safety Assessment (GDSA) Framework.* M2SF-19SN010304031; SAND2019-13835R. Albuquerque, NM: Sandia National Laboraties.

Tagirov, B.R., A. Zotov, and N. Akinfiev. 1997. "Experimental study of dissociation of HCl from 350 to 500° C and from 500 to 2500 bars: Thermodynamic properties of HCl°(aq)." *Geochim. Cosmochim. Acta* 61:4267–4280. http://linkinghub.elsevier.com/retrieve/pii/S0016703797002743.

Tambach, T.J., P.G. Bolhuis, and B. Smit. 2004. "A molecular mechanism of hysteresis in clay swelling." *Angew. Chem. Int. Ed.* 43:2650–2652.

Teich-McGoldrick, S.L., J.A. Greathouse, C.F. Jove-Colon, and R.T. Cygan. 2015. "Swelling properties of montmorillonite and beidellite clay minerals from molecular simulation: Comparison of temperature, interlayer cation, and charge location effects." *The Journal of Physical Chemistry C* 119 (36): 20880–20891.

Thiberge, S., O. Zik, and E. Moses. 2004. "An apparatus for imaging liquids, cells, and other wet samples in the scanning electron microscopy." *Review of Scientific Instruments* 75 (7): 2280–2289.

Thom, J. and G.M. Anderson. 2008. "The role of thermochemical sulfate reduction in the origin of Mississippi Valley-type deposits. I. Experimental results." *Geofluids* 8:16–26.

Timofeev, A., A.A. Migdisov, and A.E. Williams-Jones. 2015. "An experimental study of the solubility and speciation of niobium in fluoride-bearing aqueous solutions at elevated temperature." *Geochim. Cosmochim. Acta* 158:103–111.

Timofeev, A., A.A. Migdisov, and A.E. Williams-Jones. 2017. "An experimental study of the solubility and speciation of tantalum in fluoride-bearing aqueous solutions at elevated temperature." *Geochim. Cosmochim. Acta* 197:294–304.

Timofeev, A., A.A. Migdisov, A.E. Williams-Jones, R. Roback, A.T. Nelson, and H. Xu. 2018. "Uranium transport in acidic brines under reducing conditions." *Nat. Commun.* 9:1–7. http://www.nature.com/articles/s41467-018-03564-7.

Tournassat, C., I.C. Bourg, M. Holmboe, G. Sposito, and C.I. Steefel. 2016. "Molecular dynamics simulations of anion exclusion in clay interlayer nanopores." *Clays and Clay Minerals* 64 (4): 374–388.

Tournassat, C., R.M. Tinnacher, S. Grangeon, and J.A. Davis. 2018. "Modeling uranium (VI) adsorption onto montmorillonite under varying carbonate concentrations: A surface complexation model accounting for the spillover effect on surface potential." *Geochimica et Cosmochimica Acta* 220:291–308.

Tremaine, P., J. Chen, G.I. Wallace, and W.A. Boivin. 1981. "Solubility of uranium (IV) oxide in alkaline aqueous solutions to 300 C." *J. Solution Chem.* 10:221–230. http://link.springer.com/article/10.1007/BF00653099.

Vao-soongnern, V., C. Pipatpanukul, and S. Horpibulsuk. 2015. "A combined X-ray absorption spectroscopy and molecular dynamic simulation to study the local structure potassium ion in hydrated montmorillonite." *Journal of Materials Science* 50:7126–7136.

Vidal, O. and B. Dubacq. 2009. "Thermodynamic modelling of clay dehydration, stability and compositional evolution with temperature, pressure and H2O activity." *Geochimica Et Cosmochimica Acta* 73 (21): 6544–6564.

Vieillard, P., P. Blanc, C.I. Fialips, H. Gailhanou, and S. Gaboreau. 2011. "Hydration thermodynamics of the SWy-1 montmorillonite saturated with alkali and alkaline-earth cations: A predictive model." *Geochimica Et Cosmochimica Acta* 75 (19): 5664–5685.

Voltolini, M., A. Haboub, S. Dou, T.-H. Kwon, A.A. MacDowell, D.Y. Parkinson, and J. Ajo-Franklin. 2017. "The emerging role of 4D synchrotron X-ray micro-tomography for climate and fossil energy studies: five experiments showing the present capabilities at beamline 8.3.2 at the Advanced Light Source." *J. Synchrot. Radiat.* 24:1237–1249.

Wainwright, H.M., S. Finsterle, Y. Jung, Q. Zhou, and J.T. Birkholzer. 2014. "Making sense of global sensitivity analyses." *Computers & Geosciences* 65:84–94.

Whittaker, M.L., L.N. Lammers, S. Carrero Romero, B. Gilbert, and J.F. Banfield. 2019. "Ion exchange selectivity in clay is controlled by nanoscale chemical-mechanical coupling." Submitted to Proceedings of the National Academy of Science.

Xu, T., E. Sonnenthal, N. Spycher, and K. Pruess. 2006. "TOUGHREACT-A simulation program for non-isothermal multiphase reactive geochemical transport in variably saturated geologic media: Applications to geothermal injectivity and CO2 geological sequestration." *Computers & Geosciences* 32:145–165.

Xu, T., N. Spycher, E. Sonnenthal, G. Zhang, L. Zheng, and K. Pruess. 2011. "TOUGHREACT Version 2.0: A simulator for subsurface reactive transport under non-isothermal multiphase flow conditions." *Computers & Geosciences* 37 (6): 763–774.

Yang, L., X.-Y. Yu, Z. Zhu, M.J. Iedema, and J.P. Cowin. 2011a. "Probing liquid surfaces under vacuum using SEM and ToF-SIMS." *Lab on a Chip* 11 (15): 2481–2484.

Yang, L., X.-Y. Yu, Z.H. Zhu, T. Thevuthasan, and J.P. Cowin. 2011b. "Making a hybrid microfluidic platform compatible for in situ imaging by vacuum-based techniques." *J. Vac. Sci. Technol. A* 29 (6): 061101.

Yang, L., Z. Zhu, X.-Y. Yu, E. Rodek, L. Saraf, T. Thevuthasan, and J.P. Cowin. 2014. "In situ SEM and ToF-SIMS analysis of IgG conjugated gold nanoparticles at aqueous surfaces." Surface and Interface Analysis 46 (4): 224–228. https://doi.org/10.1002/sia.5252.

Yao, J., B.W. Arey, L. Yang, F. Zhang, R. Komorek, J. Chun and X.-Y. Yu. 2017. "In Situ Characterization of Boehmite Particles in Water Using Liquid SEM." *Journal of Visualized Experiments* (127): e56058. doi:10.3791/56058.

Yin, G.C., M.T. Tang, Y.F. Song, F.R. Chen, K.S. Liang, F.W. Duewer, W.B. Yun, C.H. Ko, and H.P.D. Shieh. 2006. "Energy-tunable transmission x-ray microscope for differential contrast imaging with near 60 nm resolution tomography." *Applied Physics Letters* 88 (24): 241115. doi: 10.1063/1.2211300.

Yu, J., Y. Zhou, X. Hua, Z. Zhu and X.-Y. Yu. 2016. "In Situ Characterization of Hydrated Proteins in Water by SALVI and ToF-SIMS." *Journal of Visualized Experiments* (108): 53708–53708.

Yu, X., J. Yu, Y. Zhou, Y. Zhang, J. Wang, J.E. Evans, X.-Y. Yu, X.-L. Wang, and Z. Zhu. 2017. "An investigation of the beam damage effect on in situ liquid secondary ion mass spectrometry analysis." *Rapid Communications in Mass Spectrometry* 31 (23): 2035–2042.

Yu, X.-Y., B. Arey, S. Chatterjee, and J. Chun. 2019a. "Improving in situ liquid SEM imaging of particles." Surface and Interface Analysis 51 (13):1325–1331. https://doi.org/10.1002/sia.6700.

Yu, X.-Y., B. Liu, and L. Yang. 2013. "Imaging liquids using microfluidic cells." *Microfluidics and Nanofluidics* 15 (6): 725–744.

Yu, X.-Y., J. Yao, D.B. Lao, D.J. Heldebrant, Z. Zhu, D. Malhotra, M.-T. Nguyen, V.-A. Glezakou and R. Rousseau. 2018. "Mesoscopic Structure Facilitates Rapid CO2 Transport and Reactivity in CO2 Capture Solvents." *The Journal of Physical Chemistry Letters* 9 (19): 5765–5771.

Yu, X.-Y., J. Yao, Z. Zhu and E. Buck. 2019b. "Analysis of radioactive materials in liquid using in situ SEM and ToF-SIMS." Presented at International High-Level Radioactive Waste Management (IHLRWM) Conference, Knoville, TN, American Nuclear Society.

Yu, X.-Y., L. Yang, J. Cowin, M. Iedema, and Z. Zhu. 2011. "Systems and methods for analyzing liquids under vacuum." uspto.gov. U. S. P. a. T. Office. USA, Battelle Memorial Institute**:** 16.

Zheng, L., J. Rutqvist, C. Steefel, K. Kim, F. Chen, V. Vilarrasa, S. Nakagawa, J. Zheng, J. Houseworth, and J. Birkholzer. 2014. *Investigation of Coupled Processes and Impact of High Temperature Limits in Argillite Rock*. FCRD-UFD-2014-000493, LBNL-6719E. Berkeley, CA: Lawrence Berkeley National Laboratory.

Zheng, L. H. Xu, B. Gilbert, N. Subramanian, L. Lammers, F. Claret, C. Gaboreau, X. Cao, M. Voltolini, A. MacDowell, H. Lisabeth, J. Ajo-Franklin. 2019. *Engineered Barrier System Research Activities at LBNL: FY19 Progress Report*. M3SF-19LB010308022; LBNL- 2001205. Berkeley, CA: Lawrence Berkeley National Laboratory.

Zheng, L., K. Kim, H. Xu, and J. Rutqvist. 2016. *DR Argillite Disposal R&D at LBNL*. FCRD-UFD-2016-000437; LBNL-1006013. Berkeley, CA: Lawrence Berkeley National Laboratory.

Zheng, L., L. Li, J. Rutqvist, H. Liu, and J.T. Birkholzer. 2012. *Modeling Radionuclide Transport in Clays*. FCRD-URD-2012-000128. Berkeley, CA: Lawrence Berkeley National Laboratory.

Zheng, L., J. Rutqvist, H. Xu, K. Kim, M. Voltolini, and X. Cao. 2017a. *Investigation of Coupled Processes and Impact of High Temperature Limits in Argillite Rock*. SFWD-SFWST-2017-000040; LBNL-2001014. Berkeley, CA: Lawrence Berkeley National Laboratory.

Zheng, L., J. Rutqvist, K. Kim, and J. Houseworth. 2015. *Investigation of Coupled Processes and Impact of High Temperature Limits in Argillite Rock*. FCRD-UFD-2015-000362; LBNL-187644. Berkeley, CA: Lawrence Berkeley National Laboratory.

Zheng, L., J. Rutqvist, H. Xu, and J.T. Birkholzer. 2017b. "Coupled THMC models for bentonite in an argillite repository for nuclear waste: Illitization and its effect on swelling stress under high temperature." *Engineering Geology* 230:118–129.

Zhou, Y., J. Yao, Y. Ding, J. Yu, X. Hua, J.E. Evans, X. Yu, D.B. Lao, D.J. Heldebrant, S.K. Nune, B. Cao, M.E. Bowden, X.Y. Yu, X.L. Wang, and Z. Zhu. 2016. "Improving the Molecular Ion Signal Intensity for In Situ Liquid SIMS Analysis." *J Am Soc Mass Spectrom* 27 (12): 2006–2013.